Open access • Journal Article • DOI:10.1175/1520-0469(1976)033<1955:TGOAW>2.0.CO;2

The Generation of African Waves — Source link

Mary Alice Rennick

Institutions: University of Illinois at Urbana–Champaign

Published on: 01 Oct 1976 - Journal of the Atmospheric Sciences (American Meteorological Society)

Topics: Mechanical wave, Breaking wave, Turbulence kinetic energy, Wavelength and Jet (fluid)

THE GENERATION OF AFRICAN WAVES

BY

MARY ALICE RENNICK

B.A., Knox College, 1970
M.S., University of Illinois, 1972

THESIS

Submitted in partial fulfillment of the requirements
for the degree of Doctor of Philosophy in Physics
in the Graduate College of the
University of Illinois at Urbana-Champaign, 1975

Urbana, Illinois

THE GENERATION OF AFRICAN WAVES

Mary Alice Rennick, Ph.D.
Department of Physics
University of Illinois at Urbana-Champaign, 1975

It has been speculated that westward propagating disturbances, known as African waves, originate as perturbations on the low level easterly jet which is present over northern Africa during the season of intense wave activity. A linearized, pseudo-spectral, primitive equation model is used to simulate the response of the observed jet to perturbations on the scale of African waves.

Results show that the jet is unstable due to both its horizontal and vertical shears. The sub adiabatic lapse rate, however, acts to stabilize the waves. The most unstable wave supported by the jet has a wavelength of 3000 km and a period of 2.0 - 2.5 days. It attains its maximum intensity at the 700 mb level, near 14°N. This compares favorably with the characteristics of the observed waves.

The kinetic energy of the waves grows at the expense of the kinetic energy of the mean jet. Energy is transferred at approximately equal rates by the horizontal and vertical Reynolds stresses. Energy conversions involving available potential energy are nearly an order of magnitude smaller, reflecting the fact that the kinetic energy of the wave accounts for about ninety per cent of the total wave energy.

The characteristics of the most unstable wave are virtually unchanged when a crude parameterization of latent heat release is included in the model.

The modification of the jet due to the growth of the waves is studied by allowing nonlinear interactions to take place between the wave and the zonally averaged flow. The results indicate that, for the simplified system studied, the interaction is too small to affect the stability of the jet on the time scale of a single wave.

ACKNOWLEDGMENT

The author wishes to thank Dr. M-K. Mak for his support throughout the course of this research. Dr. R. Burpee provided helpful insight into the observational aspects of the problem and generously made available his data on African disturbances. Thanks are extended to Dr. R. Wilhelmson for his helpful discussions of the computational aspects of the problem. Acknowledgment is made to the National Center for Atmospheric Research, which is sponsored by the National Science Foundation, for computer time used in this research. This work was also supported by NSF contracts GA 32443 and DES 7401188.

TABLE OF CONTENTS

I. INTRODUCTION

The term African wave is used to describe the wave-like disturbances which propagate westward across northern Africa and the Atlantic Ocean. Observational studies of the waves over the continent and near the coast of Africa have been made by Carlson (1969a,b; 1971) and by Burpee (1972, 1974, 1975). The waves have an average wavelength of about 2500 km, and a period of 3.2 days. Their most easily identified features are the oscillations of the meridional wind at 700 mb, and the accompanying fluctuations of the surface pressure. The waves are observed throughout the summer, from late June to September, but reach their maximum intensity during late August and September. During this period they propagate as a nearly continuous wavetrain. The progress of the waves as they move across the ocean has been studied using satellite photographs by Arnold (1966, 1967) and by Frank (1969, 1970). Frank (1970) has shown that as many as half of all Atlantic tropical cyclones develop from African waves.

Although the waves have been studied extensively in the vicinity of the west coast of the African bulge, (5°W - 15°W, 5°N - 15°N) relatively little is known about the early development of the waves. In particular, the mechanism by which the waves are generated is not well known. Some insight into the nature of the generating mechanism may be obtained by examining the region in which the waves are first observed. Burpee (1972) determined that the waves originate at the 700 mb level, near 30-35°E, and that the waves are most intense near 12°N. This region is just to the south of the axis of a low level easterly jet which is present during the summer months.

Because the waves form at latitudes where the jet produces a strong shear of the zonal wind, and during the season of maximum intensity of the jet, Burpee (1972) suggested that the waves may originate as unstable perturbations on the low level jet. Nitta and Yanai (1969) have discussed the possibility that the mean flow field in some tropical regions may be unstable due to its horizontal shear, and that this instability may serve as a generating mechanism for tropical waves. Burpee proposed that the vertical shear, as well as the horizontal shear associated with the low level jet is sufficiently great to support instability.

The data gives some support to this view. Although a detailed description of the momentum and heat transports by the waves cannot be constructed from the available data, it appears that the waves do transport easterly momentum away from the jet at 700 mb, at least in parts of the African wave region. Likewise, there is a transport of heat down the gradient of mean temperature at 850 mb and at 700 mb. Such transports of wave momentum and heat away from the regions in which these quantities are large results in the growth of the disturbance. Thus, the horizontal wind shear and temperature gradient (and its accompanying vertical wind shear) may both be important in the generation of African waves.

Analytic methods can provide limited information concerning shear instabilities. A necessary condition for instability of a quasigeostrophic jet was derived by Charney and Stern (1962). It can be shown that the low level African jet satisfies this condition, but little further insight into the nature of the instability can be gained analytically. It becomes necessary to resort to numerical techniques in order to probe the stability characteristics of a realistic mean flow.

It is the purpose of this study to examine the structure of the waves which are supported by the horizontal and vertical shears of the low level jet, and to compare these waves to the observations of African waves. To do this, a linearized, pseudo-spectral, primitive equation model was constructed, and applied to the African atmosphere. The model allows the effects of a number of physical features to be studied. Some of the most significant of these are the length scale of the disturbance, the intensity of the jet, and the temperature structure of the atmosphere. The instabilities generated by the horizontal shear acting alone are considered first, followed by the modifications brought about by the existence of the vertical shear. The energetics of the wave are analyzed to identify the major source of wave energy. Finally, the effect of moisture on the instability process is considered by including a crude parameterization of latent heat release in the model.

The extent to which the waves alter the stability of the mean flow is investigated using an extension of the model which allows for some nonlinear interactions. This extended model is also used to examine whether the instability can be maintained through surface heating effects.

II. OBSERVATIONS

1. The Mean Flow

The large scale wind field over Africa during the summer months is characterized by low level southwesterly winds near the equator, and easterly flow aloft. Figure 2.1 shows east-west and north-south cross sections of the August mean wind as determined by Burpee (1972). He constructed the cross sections by averaging the August data for the eight years from 1957 to 1964. The east-west cross section is taken along 13°N. This figure shows that below 300 mb the zonal wind field does not vary significantly from 15°E to the west coast of Africa, near 15°W. There are no large variations in the low level flow as far east as 33°E, indicating that it is not unreasonable to represent the time averaged flow by its zonal average. The north-south cross section is taken at 5°E. It displays two easterly wind maxima, one in the lower troposphere at 600-700 mb, and the other in the upper troposphere, at 200 mb. The upper jet reaches its maximum intensity at 10°N. It is part of the "Tropical Easterly Jet" described by Reiter (1963). It forms to the south of the quasi-stationary anticyclones which are located over the Asiatic Plateau and the Sahara Desert during the summer months. Easterly momentum is transported southward on the eastern slopes of the anticyclones, providing the jet with a source of momentum.

The strength and position of the low level jet are highly variable in both time and space. The magnitude of the jet is often as great as 20 m sec^{-1} (Carlson, 1969a). Because of the spatial variability of the jet,

the amplitude indicated in Figure 2.1, which represents an average over eight years, is probably an underestimate of the jet intensity.

Below 850 mb, the large scale circulation at low latitudes is strongly influenced by a southwesterly current. This is a monsoon-type circulation, and carries moist air from the Gulf of Guinea, northward. Because of the moist air is cooler than the dry Saharan air to the north, there is a positive south to north temperature gradient at low levels. This gradient is maintained up to the 600-700 mb level. Above that level, the temperature decreases from equator to pole. The temperature gradient reverses at approximately the same level as that at which the vertical shear of the zonal wind changes sign, in agreement with thermal wind arguments. The deviations of the temperature at 5°E from its latitudinal average value is shown in Figure 2.2.

2. Wave Disturbances

Synoptic scale disturbances in northern Africa have been the subject of a number of investigations in recent years. The most extensive studies have been made by Carlson (1969a,b; 1971) and by Burpee (1972, 1974, 1975). Other studies have been made by Dean and LaSeur (1974), Aspliden (1974), and Okulaja (1970). An earlier work by Eldridge (1957) discusses the characteristics of lines of squally weather which move across West Africa.

There are three major types of data available for the study of African waves. These are surface reports, rawinsonde reports from upper air stations, and satellite data. The locations of surface and upper air stations are shown in Figure 2.3. Not all stations were used in every study, but the figure indicates the available data coverage. The network

Figure 2.1. Monthly mean zonal wind (m sec^{-1}) for August (after Burpee, 1972).

a) Cross section along 13°N. The dotted line indicates the position of the easterly wind maximum in the lower troposphere.

b) Cross section along 5°E.

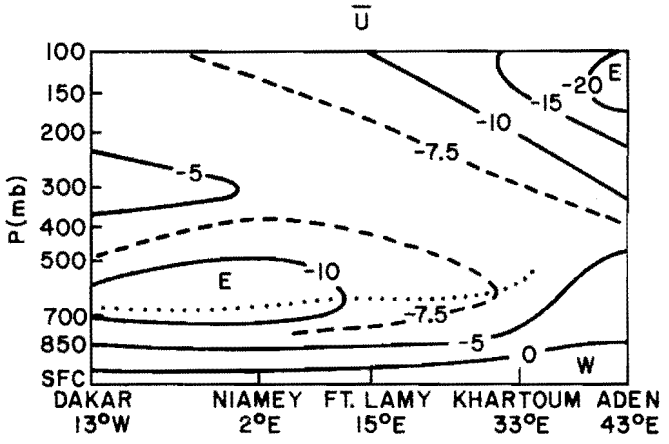
$\overline{U}$
100
150
200
300
400
500
700
850
SFC
P(mb)
-5
-7.5
-10
-15
-20
E
W
0
DAKAR
13°W
NIAMEY
2°E
FT. LAMY
15°E
KHARTOUM
33°E
ADEN
43°E

(a)

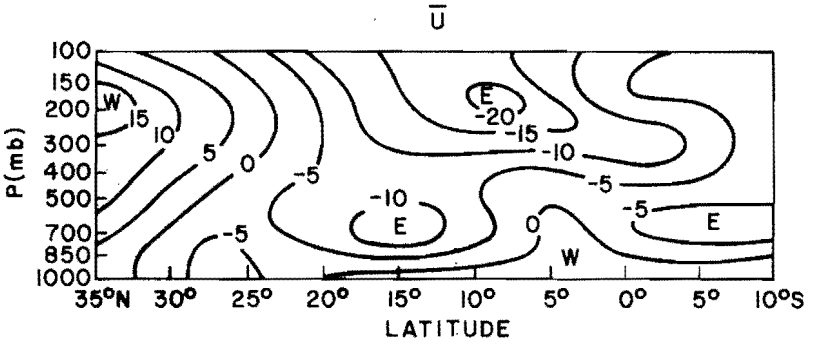
$\overline{U}$
100
150
200
300
400
500
700
850
1000
P(mb)
W
15
10
5
0
-5
-10
-15
-20
E
W
35°N
30°
25°
20°
15°
10°
5°
0°
5°
10°S
LATITUDE

(b)

Figure 2.2. Deviations of the monthly mean temperature (°C) for August at 5°E. Contour interval = 2.0C.

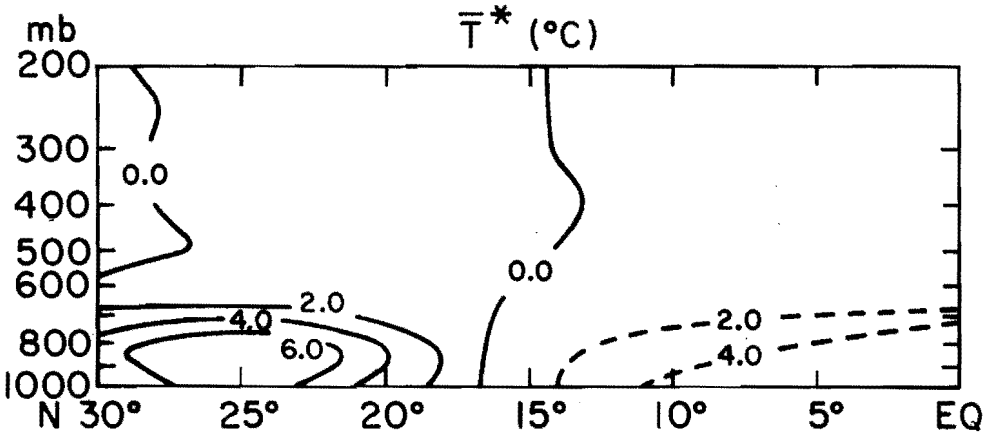
mb
$\overline{T}^*$ (°C)
200
300
400
500
600
800
1000
0.0
0.0
2.0
4.0
6.0
2.0
4.0
N 30°
25°
20°
15°
10°
5°
EQ

Figure 2.3. Map of Africa, showing the locations of reporting stations. The small solid circles are surface stations; large solid circles are the 8 upper air stations used for spectral analysis by Burpee (1972); large open circles are other upper air stations reporting more frequently than every other day; X's are other upper air stations.

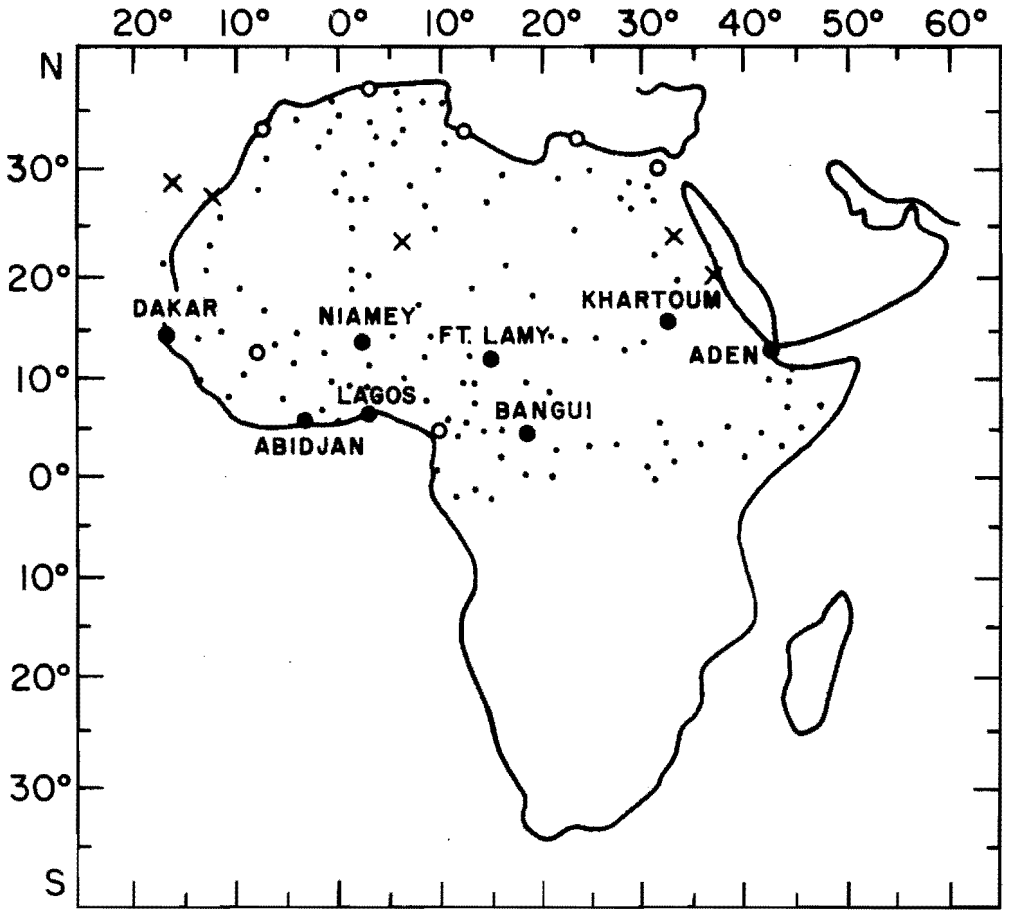
20°
10°
0°
10°
20°
30°
40°
50°
60°
N
30°
20°
10°
0°
10°
20°
30°
S
DAKAR
NIAMEY
FT. LAMY
KHARTOUM
ADEN
LAGOS
BANGUI
ABIDJAN

is most dense near the southern coast of the African bulge, along the Gulf of Guinea. There are very few reporting stations (particularly upper air stations) in the desert regions to the north of 15°N. Furthermore, the existing stations do not always report at the same times each day. Such irregularities in the data network complicate the analysis of the data considerably.

Two basic types of data analysis have been employed--synoptic analysis and spectral analysis. Carlson (1969a) studied the synoptic histories of four African waves as they progressed from about 15°E to the Cape Verde Islands during a two week period in August and September, 1967. Three of these waves later developed into Atlantic hurricanes. During the period from July to mid-September, 1968, Carlson identified 33 waves passing through the network (Carlson, 1969b). Three of these waves are discussed in great detail (Carlson, 1971). From 1 May, 1954 to 31 May, 1955, the WMO Technical Mission for Desert Locust Control compiled a set of wind data at 850 mb, 700 mb, and 500 mb by augmenting the rawinsonde network by over 100 daily pilot balloon ascents. This data set was used by Aspliden (1974) to construct monthly streamline charts. Similar synoptic techniques were used by Dean and LaSeur (1974) and by Okulaja (1970). In order to alleviate the difficulties involved with conventional synoptic analysis on a sparse data network. Burpee (1972) used spectral techniques to analyze data for the months of May through November, from 1960 to 1964. Time series of zonal and meridional wind, temperature, specific humidity, and geopotential height were constructed at nine different levels at the eight upper air stations indicated on Figure 2.3. Burpee (1974) extended the spectral treatment to include all surface stations

between 5°N and 33°N, and all upper air stations north of the equator which report at least once a day. He also used a compositing technique to determine the characteristics of the waves at the surface. Perhaps the most complete description of the waves is given by Burpee (1975) in a report based on data gathered during the Atlantic Tropical Experiment (GATE) conducted as part of the Global Atmospheric Research Project. Data from land and ship observations were analyzed by synoptic and composite techniques, and supplemented by satellite data for that study.

The waves are most easily recognized as disturbances in the horizontal wind fields that move from east to west across the African continent. From July through September the waves propagate continuously. About 25 to 30 waves leave the western coast of Africa during these months. The wavelength and period of the waves vary within the ranges 1500-4000 km, and 2.2-5.5 days. Of the 24 waves observed during the GATE in 1974, the average wavelength was 2500 km and the average period was 3.2 days. The waves first appear, and are most intense, at 700 mb, where the meridional wind perturbation reaches a maximum of from 2 m sec^{-1} to 3 m sec^{-1}. The winds at 850 mb are closely coupled to those at 700 mb, particularly during the latter part of the wave season. In the western part of the African bulge, the waves are clearly discernable in the surface data as well.

A vertical cross section of the meridional wind perturbation, v', associated with a typical wave as it leaves the African coast is shown in Figure 2.4. The cross section was constructed by compositing data from the 24 waves in 1974. At this longitude, the maximum amplitude of v' is 3.5 m sec^{-1} and is located at 700 mb. (Farther east, near 0°,

Figure 2.4. Vertical cross section of v'(m sec^{-1}) for an idealized wave (after Burpee, 1975).

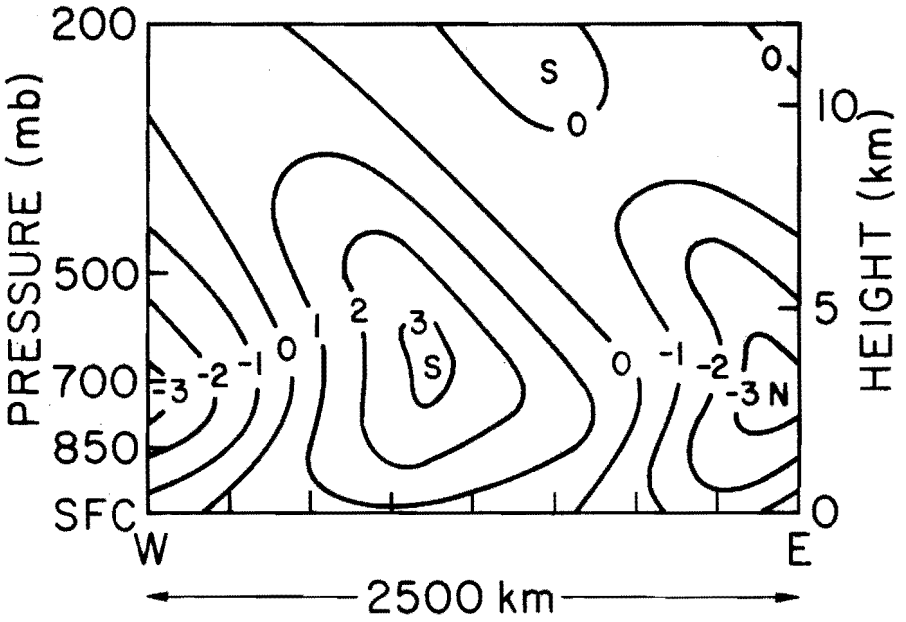
200
500
700
850
SFC
PRESSURE (mb)
W
E
2500 km
10
5
0
HEIGHT (km)
S
0
0
-3
-2
-1
0
1
2
3
S
0
-1
-2
-3 N

the maximum amplitude is less than 2 m sec^{-1}.) The wave extends downward to the surface where the maximum amplitude is 1 m sec^{-1}, and upward to 500 mb. There is no clear evidence of wave activity at 200 mb. The wave features tilt eastward with height from the surface to about 650 mb. Above this level they tilt westward with increasing height.

Figure 2.5 shows the streamlines and isotachs of the composited wave at 700 mb. The maximum wind speeds are found near 15°N. The wave features extend beyond the northern boundary of the data network, as seen by the large values of v' at 20°N. The waves probably affect the wind field south of the equator as well, as evidenced by the existence of wind speeds in excess of 1 m sec^{-1} there. Both the trough and the ridge axes slope from southwest to northeast from the equator to about 15°N. At approximately the same latitude at which the wind speed reaches its maximum value, the slopes of the axes change. In the case of the trough axis, the slope continues to be from southwest to northeast, but is more gradual to the north of 15°N. The slope of the ridge axis changes sign, and slopes from southeast to northwest. Analyses of surface data indicate that the waves have maximum surface amplitudes near 20°N, or 500-600 km to the north of the 700 mb maximum.

Although the horizontal wind perturbation is the most prominent wave feature, other quantities reflect the passage of the waves as well. The surface pressure fluctuates with the passage of the wave, with the greatest fluctuation equal to 2-3 mb near 20°N, the latitude of maximum surface wind perturbation. Spectral results (Burpee, 1972) indicate that there is a geopotential height perturbation with magnitude of about 50 m^2 sec^{-2}

Figure 2.5. Streamlines (solid lines) and isotachs (dotted lines) of the idealized wave at 700 mb. Trough and ridge axes are indicated by dashed lines (after Burpee, 1975).

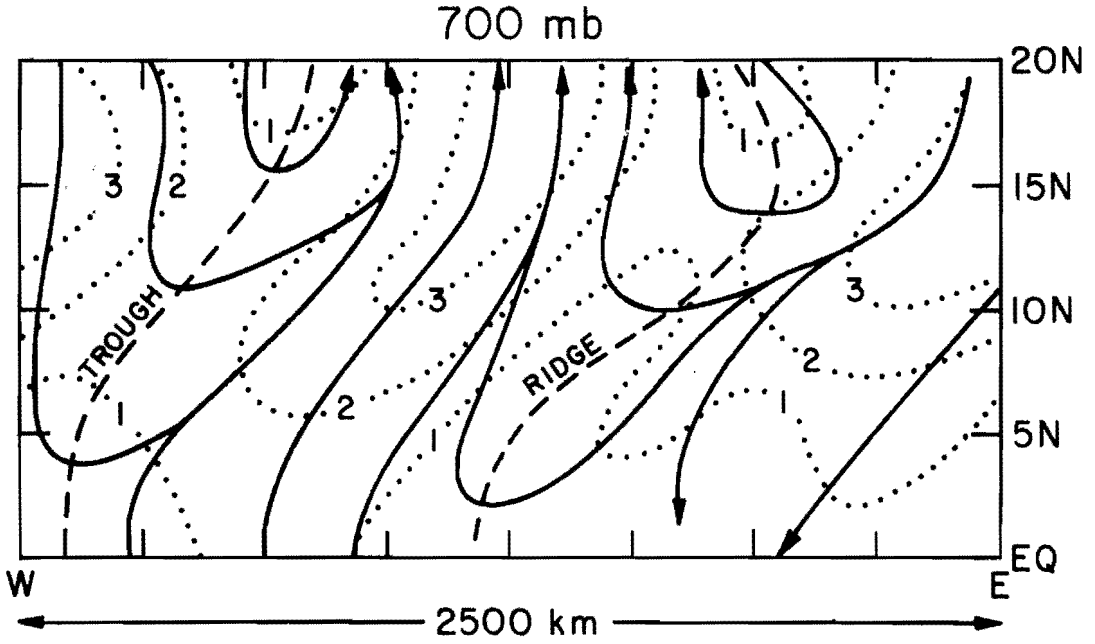
700 mb
20N
15N
10N
5N
EQ
W
E
TROUGH
RIDGE
1
2
3
2500 km

which is about 90° out of phase with the meridional wind perturbation, and in approximate geostrophic balance with it.

The temperature field associated with the waves is more difficult to determine. Burpee (1972) attempted to identify temperature oscillations at the frequency of the waves, but was unsuccessful. He also showed, however, that the amplitude of the 850 mb temperature oscillation required to maintain geostrophic balance with the wind field is about .2C, too small to be resolved by his analysis. Synoptic analysis of individual waves near the west coast of Africa indicates that temperature deviations of 1-2C are present at upper levels (400 mb), where the waves have warm cores. At lower levels the temperature deviations are smaller and the waves have cold cores. The relatively large temperature perturbation at 400 mb is due to convective activity induced when the wave encounters the moist, less stable air near the coast.

Like the temperature perturbation, the vertical velocity field of the waves reflects the degree of convective activity associated with the waves. No clear description of the vertical velocity field has been given, except in the western part of the wave domain, where satellite pictures indicate substantial convective activity. Burpee (1975) computed the vertical motion implied by the horizontal wind fields at 850, 700, and 500 mb as the waves leave the African continent. His calculations show maximum vertical velocities at 600 mb, north of 15°N. The strongest updraft is just west of the position of the 700 mb trough, and the strongest downdraft is somewhat to the east of the trough. The magnitude of the vertical velocity perturbation is about 1.5 cm sec^{-1}. This pattern is closely correlated to the upper level cloud coverage as indicated by satellite

photographs, so it may be assumed that the waves modulate the convective activity in the region. However, data from inland regions of western Africa do not show a simple correlation, and the interaction between the waves and convective activity away from the coast is not clear.

Although the mature stage of the waves as they approach the African coast and begin their propagation over the Atlantic Ocean has been fairly well documented, less is known about the mechanism by which the waves are generated, and their early development. The GATE data network extended to only 5°E, and Carlson's to 15°E. Of the 33 waves studied during the 1968 wave season, nearly half originated to the east of 15°E. Only four originated to the west of 5°E (Carlson, 1969b). Carlson suggested that the waves may be generated due to enhanced convection over elevated terrain. This would indicate that the mountainous regions of Sudan and Ethiopia may be source regions for the waves. Burpee (1972) examined the spectral data for two stations near the proposed source region: Aden, which is located to the east of the mountains, and Khartoum, which is just downstream from the mountains. Neither station showed a significant spectral peak at the frequency of African waves, indicating that the waves do not originate in that area. Aspliden (1974) also attempted to locate the source of the waves and concluded that topographic features are not principally responsible for wave generation. He found that most of the waves originate to the east of 30°E, but found no single area acting as a source region for the waves.

A connection between wave generation and the low level squall lines, or "Disturbance Lines" described by Eldridge (1957) has been suggested by Okulaja (1970). These squall lines occur frequently over Ghana and Nigeria,

well to the west of the preferred region for wave initiation as determined by Burpee (1972) and by Aspliden (1974). While the convective processes involved in squall line formation and propagation may be influenced by the passage of African waves, most of the waves form to the east of the squall line region.

III. THEORETICAL CONSIDERATIONS

The theory of hydrodynamic instability in the atmosphere has been studied extensively during the past 100 years. Some of the earliest work was done by Rayliegh (1879), who assumed that the atmosphere could be treated as a homogeneous, incompressible fluid, and derived a necessary condition for instability of a jet-like structure. More recently, the effects of buoyancy, compressibility, the earth's rotation, and viscous dissipation have been studied. Comprehensive descriptions of the major contributions to the theory of the stability of fluid flow as it applies to the earth's atmosphere are given by Lin (1955), Drazin and Howard (1966), and Kuo (1973). No attempt to summarize all the results will be made here. Only those points which relate directly to the problem of African waves will be discussed.

In order to identify the mechanisms by which an atmospheric current may become unstable, the equations of motion for a rotating fluid are studied. It is not necessary to consider the full nonlinear equations in order to investigate the stability of a jet with respect to infinitesimal perturbations. Instead, the linearized equations are used. The only modes of instability which are of interest are those which may be related to African waves. Since a single wave is confined to an area no greater than about 3000 km on a side, the equations need not be written on a sphere. The appropriate geometry is the beta-plane. This is a plane tangent to the surface of the earth at a given latitude, θ_o. The horizontal coordinates $\hat{x}$ and $\hat{y}$ are defined to be parallel to the plane, rather than to the

curved earth. Distances in the $\hat{x}$ direction are positive from west to east, and are given by $\delta x = a \cos \theta_o \, \delta\lambda$, where a is the radius of the earth, and λ is the longitude. $\hat{y}$ is positive from south to north, and distances are given by $y = y_o + a \tan (\theta - \theta_o)$, where y_o is the value of y at θ_o. Usually, $y_o = a\theta_o$. The curvature of the earth is included only in the representation of the Coriolis force. The Coriolis force is given by $\vec{F}_c = -2\vec{\Omega} \times \vec{V}$, where $\vec{\Omega}$ is the rotation of the earth. Because the horizontal components of $\vec{V}$ are much larger than the vertical component, the horizontal components of $\vec{F}_c$ may be approximated by $- f\hat{k} \times \vec{V}$, where f is the vertical component of the rotation vector, $2\Omega\sin\theta$ and $\hat{k}$ is the unit vector in the vertical direction. On a beta-plane, the variation of f is assumed to be linear with y. Then $f = f_o + \beta_y$, where $f_o \equiv 2\Omega\sin\theta_o$ and $\beta \equiv \frac{2\Omega\cos\theta_o}{a}$. Then $\frac{df}{dy} = \beta$ is a constant. It is convenient to use pressure, rather than height, as the independent vertical coordinate. For large scale motions, the atmosphere may be considered a hydrostatic fluid, so that the mass between two pressure surfaces is a constant. Then an element of mass may be expressed in x, y, p coordinates without reference to the density, and the continuity equation assumes a particularly simple form.

The equations governing inviscid, adiabatic, hydrostatic fluid motions on a beta-plane are:

$$\frac{\partial u}{\partial t} + u \frac{\partial u}{\partial x} + v \frac{\partial u}{\partial y} + \omega \frac{\partial u}{\partial p} - fv + \frac{\partial \phi}{\partial x} = 0 \qquad (1)$$

$$\frac{\partial v}{\partial t} + u \frac{\partial v}{\partial x} + v \frac{\partial v}{\partial y} + \omega \frac{\partial v}{\partial p} + fu + \frac{\partial \phi}{\partial y} = 0 \qquad (2)$$

$$\frac{\partial T}{\partial t} + u\frac{\partial T}{\partial x} + v\frac{\partial T}{\partial y} + \omega\left(\frac{\partial T}{\partial p} - \frac{\kappa T}{p}\right) = 0 \qquad (3)$$

$$\frac{\partial \phi}{\partial p} + \frac{RT}{p} = 0 \qquad (4)$$

$$\frac{\partial u}{\partial x} + \frac{\partial v}{\partial y} + \frac{\partial \omega}{\partial p} = 0 \qquad (5)$$

These are the primitive equations. The symbols have their usual meanings:

u zonal component of the wind: $\frac{d}{dt}$

v meridional component of the wind: $\frac{dy}{dt}$

ω pressure velocity: $\frac{dp}{dt}$

T temperature

ϕ geopotential: gz

f Coriolis parameter

R gas constant for dry air

Equations (1) and (2) express conservation of momentum. (3) is the appropriate form of the thermodynamic equation in the absence of diabatic heat sources. (4) requires that all motions by hydrostatic, and (5) expresses conservation of mass.

In order to address the question of the stability of infinitesimal disturbances of a basic flow, the equations are linearized. To do this, each quantity is split into two parts: $\xi(x,y,p,t) = [\overline{\xi}](y,p) + \xi'(x,y,p,t)$. $[\overline{\xi}]$ denotes the value of ξ, averaged with respect to longitude and time. ξ' represents the local deviation of the quantity ξ from its zonal and temporal average. Equations governing the mean state are obtained by

applying the averaging operator to the primitive equations, and dropping terms which are second order in perturbation quantities.

$$[\bar{v}]\frac{\partial[\bar{u}]}{\partial y} + [\bar{\omega}]\frac{\partial[\bar{u}]}{\partial p} - f[\bar{v}] = 0 \tag{6}$$

$$[\bar{v}]\frac{\partial[\bar{v}]}{\partial y} + [\bar{\omega}]\frac{\partial[\bar{v}]}{\partial p} + f[\bar{u}] + \frac{\partial[\bar{\phi}]}{\partial y} = 0 \tag{7}$$

$$[\bar{v}]\frac{\partial[\bar{T}]}{\partial y} + [\bar{\omega}]\left(\frac{\partial[\bar{T}]}{\partial p} - \frac{\kappa[\bar{T}]}{p}\right) = 0 \tag{8}$$

$$\frac{\partial[\bar{\phi}]}{\partial p} + \frac{R[\bar{T}]}{p} = 0 \tag{9}$$

$$\frac{\partial[\bar{v}]}{y} + \frac{\partial[\bar{\omega}]}{p} = 0 \tag{10}$$

If the undisturbed state of the atmosphere can be represented by a steady zonal flow $[\bar{u}]$, with $[\bar{v}] = [\bar{\omega}] = 0$, these equations reduce to the simpler system

$$f[\bar{u}] + \frac{\partial[\bar{\phi}]}{\partial y} = 0 \tag{11}$$

$$\frac{\partial[\bar{\phi}]}{\partial p} + \frac{R[\bar{T}]}{p} = 0 \tag{12}$$

These equations may be combined to form

$$\frac{\partial[\bar{u}]}{\partial p} - \frac{R}{fp}\frac{\partial[T]}{\partial y} = 0 \tag{13}$$

(12) is just the hydrostatic equation. (11) states that the pressure gradient force, $\frac{\partial[\phi]}{\partial y}$ must be exactly balanced by the Coriolis force, f[u]. This is the geostrophic relationship. (13) is the geostrophic thermal wind equation, an undisturbed purely zonal flow must be in geostrophic balance. Even under more general conditions, the wind and height fields are usually in approximate geostrophic balance.

Since $[\bar{T}]$ enters the thermal wind equation only as $\frac{\partial[\bar{T}]}{\partial y}$, and because the temperature varies much more rapidly with pressure than it does with latitude, it is convenient to define an additional operator $\sim$, which represents an average with respect to time, latitude, and longitude. Then $[\bar{T}] = \tilde{T} + [\bar{T}]^*$. $\tilde{T}$ is a function of pressure only.

A set of equations for the perturbation motions is obtained by subtracting equations (6) - (10) from (1) - (5) with the assumption $[\bar{v}] = [\bar{\omega}] = 0$. Neglecting terms which are second order in perturbation quantities, the resulting equations are:

$$\frac{\partial u'}{\partial t} + [\bar{u}]\frac{\partial u'}{\partial x} + \frac{\partial[\bar{u}]}{\partial y}v' + \frac{\partial[\bar{u}]}{\partial p}\omega' - fv' + \frac{\partial \phi'}{\partial x} = 0 \qquad (14)$$

$$\frac{\partial v'}{\partial t} + [\bar{u}]\frac{\partial v'}{\partial x} + fu' + \frac{\partial \phi'}{\partial y} = 0 \qquad (15)$$

$$\frac{\partial T'}{\partial t} + [\bar{u}]\frac{\partial T'}{\partial x} + \frac{\partial[\bar{T}]^*}{\partial y}v' + \left(\frac{\partial[\bar{T}]}{\partial p} - \frac{\kappa[\bar{T}]}{p}\right)\omega' \qquad (16)$$

$$\frac{\partial \phi}{\partial p} + \frac{RT'}{p} = 0 \qquad (17)$$

$$\frac{\partial u'}{\partial x} + \frac{\partial v'}{\partial y} + \frac{\partial \omega'}{\partial p} = 0 \qquad (18)$$

An additional simplification to the equations arises from the fact that the static stability, $\sigma = \left(\frac{\partial \tilde{T}}{\partial p} - \frac{\kappa \tilde{T}}{p}\right)$ is usually significantly larger than $\left(\frac{\partial [\bar{T}]^*}{\partial p} - \frac{\kappa [\bar{T}]^*}{p}\right)$. When this is the case, the thermodynamic equation (16) may be rewritten

$$\frac{\partial T'}{\partial t} + [\bar{u}] \frac{\partial T'}{\partial x} + \frac{\partial [\bar{T}]^*}{\partial y} v' + \sigma\omega' = 0 \qquad (19)$$

Equations (14), (15), (17), (18), and (19) govern small perturbations in an atmosphere which is characterized by a steady zonal flow [u] and a mean temperature field which satisfies the condition $\left|\frac{\partial \tilde{T}}{\partial p} - \frac{\kappa \tilde{T}}{p}\right| >> \left|\frac{\partial [\bar{T}]^*}{\partial p} - \frac{\kappa [\bar{T}]^*}{p}\right|$. In order to investigate the nature of the solutions to these equations, appropriate boundary conditions must be chosen. In writing the equations on a beta-plane, it is assumed that the solution is of interest for only a limited range of latitudes. The boundary conditions are chosen such that there is no mass flux across the lateral boundaries. Then $v' = 0$ at the equator and at 30°N. The perturbations on the mean state are assumed to be wave-like in nature, so that periodic boundary conditions are applied in the x direction. In order to preserve the total mass of air in the channel under consideration, there must be no vertical flow into or out of the atmosphere, so $\omega' = 0$ at the surface of the earth and at the top of the atmosphere.

A first step toward understanding the growth of disturbances in the system described by the primitive equations is to consider the energetics of a disturbance. The kinetic energy of a disturbance, the eddy kinetic energy, is defined in terms of the horizontal velocity perturbation. The kinetic energy per unit surface area is given by

$$EKE = \frac{\frac{1}{2}\int dM(u'^2 + v'^2)}{\int ds}$$

where dM is an element of mass and ds is an element of surface area. The sum of the gravitational potential energy and the internal thermal energy of the atmosphere is given by the total dry static energy,

$$S = \frac{\int dM\, c_p\, T}{\int ds}$$

Instead of dealing directly with S, it is convenient to define the available potential energy. This is the excess of dry static energy over that which would be present following an adiabatic redistribution of mass such that the potential temperature surfaces were parallel to the pressure surfaces. This is the maximum amount of energy which could be converted to kinetic energy by means of adiabatic motions. Lorenz (1955) has shown that the eddy available potential energy may be approximated by

$$EAPE = \frac{-\frac{1}{2}\int dM \frac{R}{p\sigma} T'^2}{\int ds} .$$

This expression for EAPE is valid unless the mean temperature stratification of the atmosphere is nearly neutral, in which case $\sigma \simeq 0$. Its meaning becomes less clear when the contribution to the overall stratification due to deviations from the mean temperature, $\left(\frac{\partial [\bar{T}]^*}{\partial p} - \frac{\kappa [\bar{T}]^*}{p}\right)$, becomes comparable to σ.

It is a simple matter to derive the equations governing the net changes in EKE and EAPE throughout the total mass of the atmosphere.

$$\frac{dEKE}{dt} = \frac{\int dM(u' \frac{\partial u'}{\partial t} + v' \frac{\partial v'}{\partial t})}{\int ds} \tag{20}$$

$$\frac{dEAPE}{dt} = \frac{-\int dM \frac{R}{p\sigma} T' \frac{\partial T'}{\partial t}}{\int ds} \tag{21}$$

Upon substitution from the momentum equations (14) and (15), and applying the boundary conditions, (20) becomes

$$\frac{dEKE}{dt} = \frac{\int dM \left\{ - \frac{\partial[\bar{u}]}{\partial y} u'v' - \frac{\partial[\bar{u}]}{\partial p} u'\omega' + \phi' \left(\frac{\partial u'}{\partial x} + \frac{\partial v'}{\partial y} \right) \right\}}{\int ds}$$

Successive applications of the continuity equation (18) and the hydrostatic relation (17) yield the final result:

$$\frac{dEKE}{dt} = \frac{\int dM \left\{ - \frac{\partial[\bar{u}]}{\partial y} u'v' - \frac{\partial[\bar{u}]}{\partial p} u'\omega' - \frac{R}{p} T'\omega' \right\}}{\int ds} \tag{22}$$

The equation for $\frac{dEAPE}{dt}$ may be derived in a similar manner, substituting the thermodynamic equation (19) into (21).

$$\frac{dEAPE}{dt} = \frac{\int dM \frac{R}{p\sigma} \left\{ \frac{\partial[\bar{T}]}{\partial y} T'v' + \sigma T'\omega' \right\}}{\int ds}$$

$$\frac{dEAPE}{dt} = \frac{\int dM \left\{ \frac{R}{p\sigma} \frac{\partial[\bar{T}]}{\partial y} T'v' + \frac{R}{p} T'\omega' \right\}}{\int ds} \tag{23}$$

The sum of (22) and (23) is the net change in the total energy of the disturbance:

$$\frac{dETE}{dt} = \frac{\int dM \left\{ - \frac{\partial[\bar{u}]}{\partial y} u'v' - \frac{\partial[\bar{u}]}{\partial p} u'\omega' + \frac{R}{p\sigma} \frac{\partial[\bar{T}]}{\partial y} T'v' \right\}}{\int ds} \qquad (24)$$

From (24) it may be seen that there are three mechanisms by which the total energy of the disturbance may be changed. Two of these, those described by $- \frac{\partial[\bar{u}]}{\partial y} u'v'$ and $- \frac{\partial[\bar{u}]}{\partial p} u'\omega'$, represent conversion of the kinetic energy of the zonally averaged flow, ZKE, to EKE. The third mechanism, described by $\frac{R}{p\sigma} \frac{\partial[T]}{\partial y} T'v'$, represents conversion of the available potential energy of the zonally averaged frow, ZAPE, to EAPE. As may be seen from (22) and (23), EAPE can be converted to EKE by an overturning process described by $- \frac{R}{p} T'\omega'$.

The energy conversion $- \frac{\partial[\bar{u}]}{\partial y} u'v'$ allows a disturbance to grow at the expense of the mean flow by down-gradient transport of zonal momentum. The transport is accomplished by the horizontal Reynolds stress. This mechanism is generally considered to be important in the tropics. Charney (1963) used scale analysis to show that, in the absence of condensation, tropical motions are nearly horizontal. The horizontal wind field is essentially non-divergent. Vertical coupling is a second order effect. If vertical coupling is eliminated from the primitive equations by requiring $\frac{\partial}{\partial p} = 0$, then it follows that $\omega' = 0$ and $T' = 0$. The equations become:

$$\frac{\partial u'}{\partial t} + [\bar{u}] \frac{\partial u'}{\partial x} + \frac{\partial[\bar{u}]}{\partial y} v' - fv' + \frac{\partial \phi'}{\partial x} = 0 \qquad (25)$$

$$\frac{\partial v'}{\partial t} + [\bar{u}] \frac{\partial v'}{\partial x} + fu' + \frac{\partial \phi'}{\partial y} = 0 \qquad (26)$$

$$\frac{\partial u'}{\partial x} + \frac{\partial u'}{\partial y} = 0 \qquad (27)$$

The only way in which the energy of a disturbance governed by (25) - (27) can change is through the action of the horizontal Reynolds stress. Thus, since there is very little water vapor available for condensation in the region in which African waves are generated, Charney's scaling arguments suggest that down-gradient momentum transport is an important mechanism for the growth of the waves.

That this mechanism may be important in the generation of African waves has been proposed in various forms by Frank (1970), Carlson (1971), Burpee (1972), and Aspliden (1974). Both the upper and lower tropospheric jets (see Figure 2.1) are seasonal. They are present only during the summer months. Indeed, they are most intense during the months of strong wave activity. Since the lower tropospheric jet is centered near the 600-700 mb level, the same level at which the waves originate, it is quite possible that the waves originate as unstable perturbations on this jet. Burpee (1974) computed the transport of horizontal momentum by the waves. He found transport of easterly momentum away from the 700 mb jet at the rate of 1.0 m^2 sec^{-2} at 12°N. At 5°N, easterly momentum is transported toward the jet at the rate 0.5 m^2 sec^{-2}. This result is contrary to an earlier result (Burpee, 1972) which indicated a transport of easterly momentum away from the jet at both 12°N and 5°N. The transport of momentum away from the jet indicates that horizontal shear instabilities may contribute to the growth of the waves.

The conditions under which horizontal momentum transport can lead to the unbounded growth of a disturbance in a non-rotating fluid were found by Rayleigh (1880). The treatment was extended to the case of a rotating fluid by Kuo (1949). The system is reduced to a single ordinary

differential equation by introducing a streamfunction ψ', defined by: $u' = -\frac{\partial \psi'}{\partial y}$; $v' = \frac{\partial \psi'}{\partial x}$. (27) is then satisfied identically, and the vertical component of the perturbation vorticity, $\zeta' = -\frac{\partial u'}{\partial y} + \frac{\partial v'}{\partial x}$ is given by $\nabla^2 \psi'$, where ∇^2 is the two-dimensional operator $\left(\frac{\partial^2}{\partial x^2} + \frac{\partial}{\partial y^2}\right)$. The local rate of change of vorticity is found by forming $\frac{\partial}{\partial x}(26) - \frac{\partial}{\partial y}(25)$.

$$\left(\frac{\partial}{\partial t} + [\bar{u}]\frac{\partial}{\partial x}\right)\nabla^2\psi' + \left(\beta - \frac{d^2[\bar{u}]}{dy^2}\right)\frac{\partial \psi'}{\partial x} = 0 \qquad (28)$$

(28) is the barotropic vorticity equation, expressing the conservation of absolute vorticity, $\zeta' + f$, in a horizontal system. The x and t dependence of the solution ψ' may be separated by writing $\psi' = \mathrm{Re}\ \hat{\psi}(y) \exp[ik(x-ct)]$ where $\hat{\psi}$ is a complex amplitude containing the latitudinal dependence of the solution, k is a real wavenumber, and c is a complex phase velocity. Upon substitution into (28), this leads to the ordinary differential equation:

$$\frac{d^2\hat{\psi}}{dy^2} - \left(k^2 - \frac{\beta - d^2[u]/dy^2}{[\bar{u}] - c}\right)\hat{\psi} = 0 \qquad (29)$$

The solution ψ' will grow exponentially with time if the imaginary part of c is greater than zero. A necessary condition for $c_i \neq 0$ may be obtained by eliminating c_r between the real and imaginary parts of (29). Then

$$\frac{d}{dy}\left(\hat{\psi}_i \frac{d\hat{\psi}_r}{dy} - \hat{\psi}_r \frac{d\hat{\psi}_i}{dy}\right) - 2\,\mathrm{Im}\left(\frac{1}{[\bar{u}]-c}\right)\left(\beta - \frac{d^2[\bar{u}]}{dy^2}\right)|\hat{\psi}|^2 = 0 \qquad (30)$$

The boundary conditions on v' require that $\hat{\psi}_r = \hat{\psi}_i = 0$ on the lateral boundaries, so (30) may be integrated with respect to y to give:

$$c_i \int_{y_1}^{y_2} dy \left(\beta - \frac{d^2[\bar{u}]}{dy^2} \right) \frac{|\hat{\psi}|^2}{|[\bar{u}] - c|^2} = 0 \qquad (31)$$

In order that $c_i \neq 0$, the average value of $\beta - \frac{d[\bar{u}]}{dy^2}$, weighted by $\frac{|\hat{\psi}|}{|[\bar{u}] - c|^2}$, must vanish. A necessary (although not sufficient) condition for this is that the quantity $\left(\beta - \frac{d^2[\bar{u}]}{dy^2} \right)$ must change sign somewhere in the domain. Since $\left(\beta - \frac{d^2[\bar{u}]}{dy^2} \right)$ is the meridional derivative of the absolute vorticity of the mean flow, a necessary condition for instability of the flow is that $\frac{d}{dy}$ $(f + [\bar{\zeta}])$ changes sign.

That the barotropic instability could account for some observed disturbances in the tropics has been suggested by the work of Nitta and Yanai (1969). They considered the observed latitudial distribution of $(f + [\zeta])$ over the Marshall Islands in the Pacific Ocean. They found that the meridional gradient of the absolute vorticity changes sign near the latitudes at which easterly waves are observed. Furthermore, the growth rate and wavelength of the observed waves are compatible with those calculated from barotropic theory.

The absolute vorticity of the monthly mean flow at 5°E was computed using the monthly mean cross sections constructed by Burpee.[1] $(f + [\zeta])$ at 700 mb is plotted as a function of latitude in Figure 3.1 for the months of January, April, August, and November. Only in August does $\frac{d}{dy}$ $(f + [\zeta])$ change sign. Thus, the season of African wave activity coincides with the season during which the necessary condition for barotropic instability is satisfied. This implies that barotropic instability may be an important mechanism by which kinetic energy is transferred from the mean flow to growing wave disturbances.

[1] Private communication.

Figure 3.1. $f + [\zeta]$ at 5°E ($\times 10^{-5}$ sec^{-1})

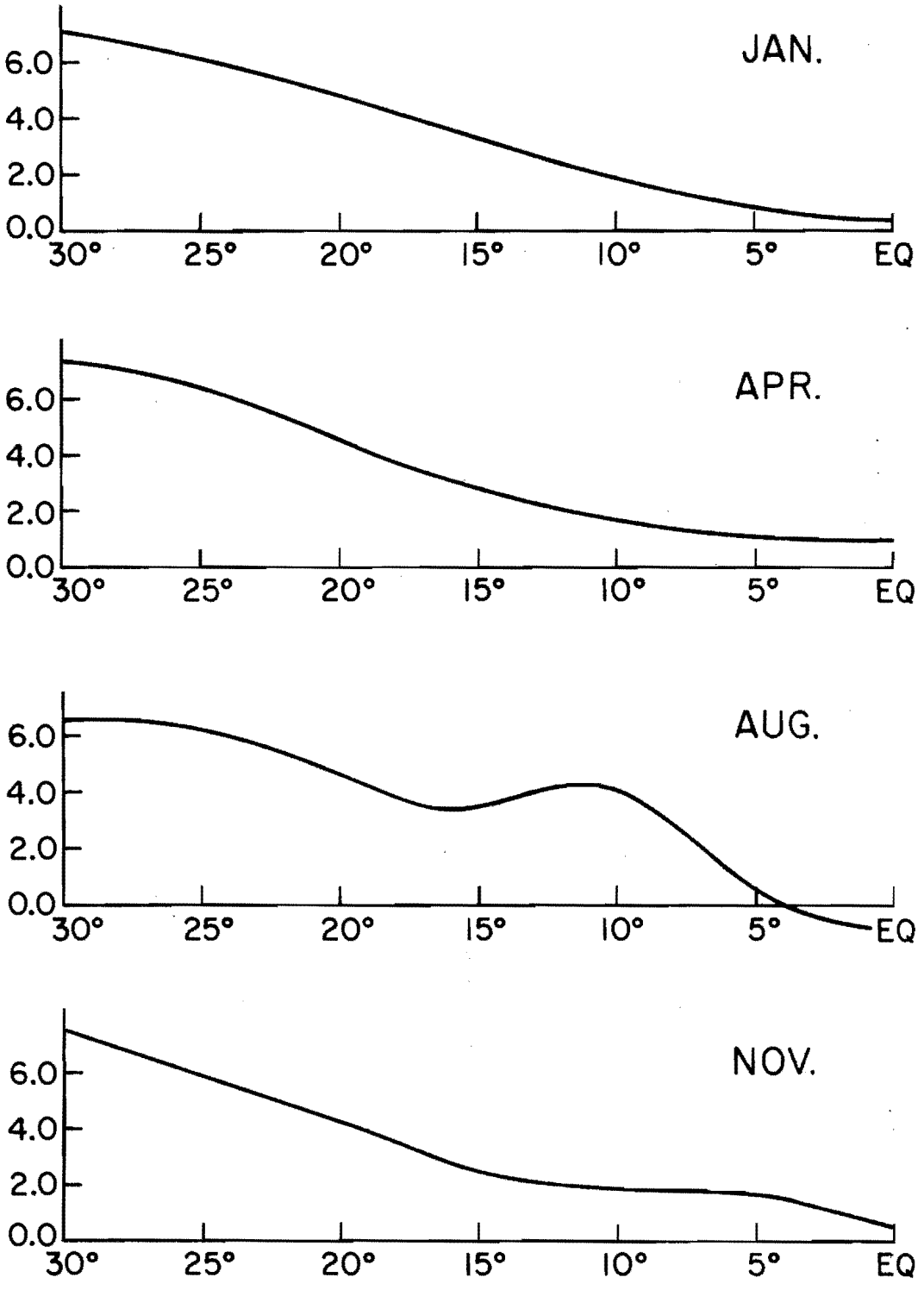
JAN.
APR.
AUG.
NOV.
6.0
4.0
2.0
0.0
30°
25°
20°
15°
10°
5°
EQ

A mechanism similar to barotropic instability can convert ZKE to EKE by transporting zonal momentum down the vertical gradient of mean zonal momentum. This process is represented by the term $-\frac{\partial[\bar{u}]}{\partial p} u'\omega'$ in the energy equation. In an atmosphere in which [u] is a function of p only ($\frac{\partial[\bar{u}]}{\partial y} = 0$), a stability analysis similar to that for the barotropic system may be carried out. In order to do this, three important assumptions must be made. The first is that the horizontal scale of the disturbance is small enough so that the effect of the Coriolis force may be neglected. The disturbance is also assumed to be independent of y. The stratification of the mean state is assumed to be neutral, so that the potential temperature of the undisturbed atmosphere is independent of pressure, and $\sigma = 0$. Then a parcel of air which is displaced vertically is neutrally bouyant. The gravitational force vanishes.

If these assumptions are all met, then the necessary condition for instability is that $\frac{\partial^2[\bar{u}]}{\partial p^2}$ must change sign. This condition is met by the mean flow over Africa. At most points between 10°N and 20°N, there is an inflection point in $[\bar{u}]$ near the 700 mb level. However, this does not necessarily imply that the atmosphere must be unstable due to this mechanism, because other factors tend to stabilize the flow. The horizontal scale of the disturbance is not really small enough to allow the Coriolis force to be neglected. The assumption that the disturbance is independent of y cannot be justified by scaling considerations or by an appeal to observations. Squire (1933) has shown that in a flow containing shear in only one dimension, the maximally unstable disturbance is always two dimensional. Therefore, relaxation of the assumption of lateral decoupling should decrease the instability. Furthermore, the assumption that $\sigma = 0$

is not justified. Except in thin layers near the surface, the atmosphere is almost never neutrally stratified. Instead, the potential temperature increases with height, so that $\sigma < 0$ and gravitational forces act to inhibit vertical motions. Thus, both the temperature stratification and the three dimensional nature of the disturbances tend to stabilize any disturbances which might be expected to grow at the expense of the mean flow through the vertical transport of zonal momentum. So although $\frac{\partial^2[\bar{u}]}{\partial p^2}$ changes sign in the region of African wave activity, this does not imply that instabilities must be generated through $-\frac{\partial[\bar{u}]}{\partial p} u'\omega'$.

While the direct effect of vertical wind shear on the stability of the mean flow is not entirely clear, the accompanying meridional temperature gradient gives rise to a simple baroclinic instability which may be treated using quasi-geostrophic theory. (A summary of quasi-geostrophic theory is presented in Appendix I.) In general, baroclinic instability is not considered to be an important energy generating mechanism in the tropics, because it requires a large meridional temperature gradient, which is not found in the tropics. Furthermore, the growth rate of the instability can be shown to grow as the Coriolis parameter. Since $f = 0$ at the equator, the instability must be inhibited in the tropics. However, the presence of the Sahara Desert results in low level temperature gradients which are anomalously large for the tropics, so that the possibility of baroclinic instability cannot be immediately rejected.

Baroclinic instability is a means by which the available potential energy of the zonal mean flow, ZAPE, may be converted to EKE. The conversion does not take place directly; the energy must first be converted from ZAPE to EAPE, and then from EAPE to EKE. The conversion

from ZAPE to EAPE can proceed whenever the trajectories of the perturbation motion are such that they make a smaller angle with the horizontal than do the surfaces of constant potential temperature. This type of flow results in a situation in which dense air overlies less dense air. This configuration is unstable; the resulting overturning converts EAPE to EKE. Quasi-geostrophic theory can be used to estimate the smallest possible slope for the perturbation trajectories, or equivalently, the smallest possible value of $\frac{\partial[\bar{u}]}{\partial p}$ such that the instability may proceed.

The linearized form of the quasi-geostrophic vorticity equation is

$$\frac{\partial \zeta_g'}{\partial t} + [\overline{u_g}] \frac{\partial \zeta_g'}{\partial x} + \left(\beta + \frac{\partial[\overline{\zeta_g}]}{\partial y}\right) v_g' + f_o \left(\frac{\partial u'}{\partial x} + \frac{\partial v'}{\partial y}\right) = 0 \qquad (32)$$

Equation (32), along with equations (17) and (19), govern the quasi-geostrophic system. Charney (1947) was the first to study the stability characteristics of this system. He assumed that $[\overline{u_g}]$ increased linearly with height and was independent of y. The only energy source by which disturbances may grow in this system is the transport of heat down the meridional temperature gradient, a process described by $\frac{R}{p\sigma} \frac{\partial[\bar{T}]}{\partial y} T'v'$. Charney's results, and those of subsequent authors (e.g. Eady, 1949; Kuo, 1952) show that if the vertical shear of $[\overline{u_g}]$ is sufficiently great, disturbances with wavelengths of several thousand kilometers are unstable. If ΔU is the change in $[\overline{u_g}]$ through a layer of depth Δp, then, for some wavelength, perturbations grow exponentially if

$$\Delta U > \Delta U_c \equiv \frac{\beta}{f_o^2} \frac{R}{p} \sigma(\Delta p)^2 \qquad (33)$$

For usual mid latitude conditions, the inequality (33) is almost always satisfied. Therefore, the theory of quasi-geostrophic instability is very useful in understanding the growth of mid latitude disturbances. However, since $U_c \alpha \frac{1}{f_o^2}$, the shear required for instability increases rapidly toward the equator. In the African wave region, the largest values for the vertical shear of $[\bar{u}]$ occur between 1000 mb and 650 mb. Using a typical value for σ, and f_o at 15°N, the change in $[\bar{u}]$ between 1000 mb and 650 mb required by (34) for instability is 27 m sec^{-1}. Since observed values of the shear at the peak of the African wave season rarely exceed 20 m sec^{-1}, it is not likely that quasi-geostrophic baroclinic instability plays an important role in the generation of African waves.

This does not necessarily imply that horizontal heat transport is not an important mechanism in wave generation. The system described above represents a maximum simplification of the problem. The assumptions which lead to (32) are well justified in mid latitudes, but they are more dubious in the tropics. It is likely, then, that non-geostrophic effects are important. Also, the assumption of linear shear of $[\bar{u}]$ is not good for the African wave region. Phillips (1964) has shown that if non-geostrophic effects are included in the analysis, consistency requires that the meridional dependence of the disturbance be included as well. All of this indicates that the processes allowed by the real atmosphere in the region of African wave activity are far more complex than those described by the quasi-geostrophic model. Thus, it cannot be concluded that horizontal heat transport is unimportant, but only that it is not obvious that the mechanism is important.

A serious drawback to the preceding discussion of instability mechanisms is that the three energy generating mechanisms have been treated separately. This greatly simplifies the analysis, but it precludes the possibility of interactions between the mechanisms. In fact, the August mean zonal wind over Africa displays a definite jet-like structure. Both horizontal and vertical shears are present. The horizontal shear at 700 mb is sufficient to support barotropic instabilities. The vertical shear is nowhere sufficiently great to support simple quasi-geostrophic baroclinic instability.

The nature of the interaction between horizontal and vertical shears is not well known. A necessary condition for instability in a quasi-geostrophic atmosphere having both horizontal and vertical shear was derived by Charney and Stern (1962), and extended somewhat by Charney (1973). Pedlosky (1964a,b; 1965) used a two level quasi-geostrophic model to study the effect of a small horizontal shear on a baroclinically unstable system. These studies do not use the primitive equations. They consider the interactions between the horizontal momentum transport and the horizontal heat transport. They do not consider the vertical transport of horizontal momentum by the vertical Reynolds stress. Orlanski (1968) used the primitive equations in a numerical model to find the effect of changing the slope of a frontal surface on the type of frontal wave generated. His model is related to the problem of jet instability, but does not bear directly on it. The only work that considers a true jet situation is that of Charney and Stern.

Charney and Stern derived a condition for the stability of a jet structure similar to that derived by Kuo (1949) for a barotropic flow.

The relevant quantity of the mean flow is not the gradient of absolute vorticity, $\frac{\partial}{\partial y}(f + [\bar{\zeta}])$, as in the barotropic case, but that of the pseudo-potential vorticity,

$$\frac{\partial [\bar{q}]}{\partial y} = \frac{\partial}{\partial y}(f + [\bar{\zeta}]) + \frac{\partial}{\partial p}\left(\frac{pf_o^2}{R\sigma}\frac{\partial [\bar{u}]}{\partial p}\right) \tag{34}$$

Charney (1973) showed that if the surface temperature increases northward, as is the case in northern Africa, $\frac{\partial [\bar{q}]}{\partial y}$ must be negative somewhere in the domain in order to have instability.

Values of $\frac{\partial [\bar{q}]}{\partial y}$ at 700 mb are plotted in Figure 3.2. The dotted line is the gradient of absolute vorticity; the dashed line is the baroclinic term, $\frac{\partial}{\partial p}\left(\frac{pf_o^2}{R}\frac{\partial [\bar{u}]}{\partial p}\right)$. $\frac{\partial [\bar{q}]}{\partial y}$ is indeed negative between 10°N and 15°N. This is due mostly to the barotropic term, $\frac{\partial}{\partial y}(f + [\bar{\zeta}])$. The baroclinic term contributes to the negativity of $\frac{\partial [\bar{q}]}{\partial y}$, but is always smaller in magnitude than the barotropic term. This analysis indicates that the flow may be unstable, and that the instability is mainly due to the horizontal shear of the mean wind, although the vertical shear effects are of the proper sign to support the instability.

The preceding discussion of possible modes of shear instability as applied to the region of African wave generation remains incomplete. It shows that the horizontal shear of the mean flow is sufficiently great so that the horizontal Reynolds stress probably acts as a generating mechanism for the energy of a disturbance. The vertical Reynolds stress may act in a similar manner, but the stabilizing effect of the temperature stratification tends to inhibit this instability. The vertical shear of the mean flow is apparently not intense enough to support the conversion of ZAPE to EAPE by means of baroclinic instability.

Figure 3.2. The gradient of pseudo-potential vorticity at 700 mb.

$\cdots\cdots \frac{\partial}{\partial y}(f + [\overline{q}]$

$---- \frac{\partial}{\partial p}\left(\frac{pf_o^2}{R\sigma}\frac{\partial[\overline{u}]}{\partial p}\right)$

$\_\_\_\_ \frac{\partial[\overline{q}]}{\partial y}$

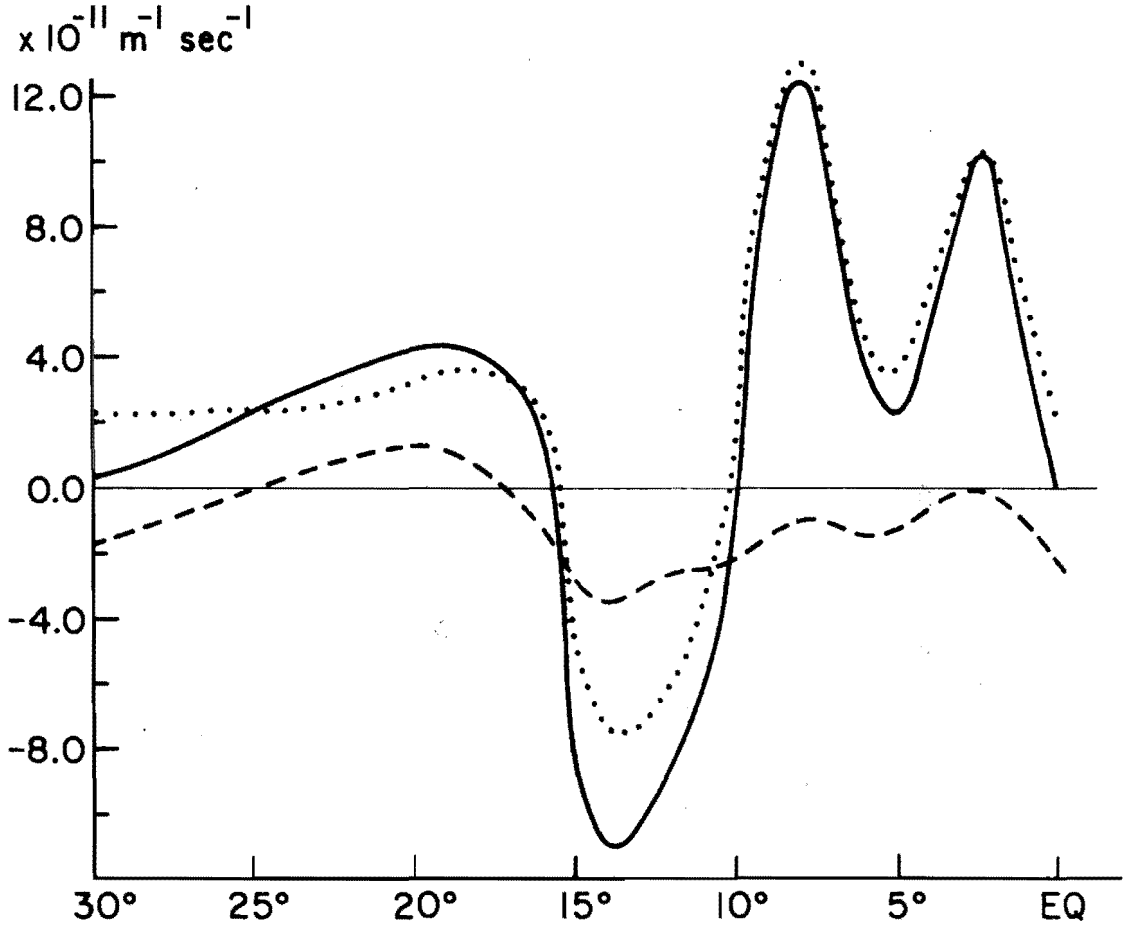

In order to investigate the instabilities of the flow in more detail, and to study the interactions among the three possible energy generating mechanisms, the equations of motion can be solved numerically. A numerical model can be used to determine the stability of the mean flow to small perturbations, and to determine the structure of any growing disturbances which are supported by the flow.

IV. THE MODEL

1. Construction of the Model

The linear stability criteria derived in Chapter 3 indicate that the low level jet over Africa may be unstable due to its horizontal and/or vertical shear. Since an analytic solution to the primitive equations (3.14) - (3.18) is not feasible, it is necessary to employ a numerical model to obtain an approximate solution to the equations for a realistic mean state. The model results should establish not only whether or not the observed mean flow is capable of supporting disturbances on the scale of African waves, but also the particular features of the flow which are responsible for the instability. Furthermore, the model should indicate by what physical mechanisms energy is transferred from the mean flow to the waves, and in what ways the competing mechanisms interact.

Like the theoretical analysis, the model is based on the linearized equations of motion. This is justified since the principal aim of the model is to study the initiation stage of the waves. During the initiation process the wave amplitudes are small, and linear processes should be dominant. For convenience, the equations of motion (3.14) - (3.18) are repeated here.

$$\frac{\partial u'}{\partial t} + [\bar{u}]\frac{\partial u'}{\partial x} + \frac{\partial [\bar{u}]}{\partial y} v' + \frac{\partial [\bar{u}]}{\partial p} \omega' - fv' + \frac{\partial \phi'}{\partial x} = 0 \qquad (1)$$

$$\frac{\partial v'}{\partial t} + [\bar{u}]\frac{\partial v'}{\partial x} + fu' + \frac{\partial \phi'}{\partial y} = 0 \qquad (2)$$

$$\frac{\partial T'}{\partial t} + [\bar{u}]\frac{\partial T'}{\partial x} + \frac{\partial [\bar{T}]}{\partial y} v' + \sigma\omega' + \left(\frac{\partial [\bar{T}]^*}{\partial p} - \frac{\kappa [\bar{T}]^*}{p}\right) \omega' \qquad (3)$$

$$\frac{\partial \phi'}{\partial p} + \frac{RT'}{p} = 0 \qquad (4)$$

$$\frac{\partial u'}{\partial x} + \frac{\partial v'}{\partial y} + \frac{\partial \omega'}{\partial p} = 0 \qquad (5)$$

In order to solve these equations, the x dependence of the solution is separated, and a solution of the form $\xi'(x,y,p,t) = \xi_1(y,p,t)\sin kx + \xi_2(y,p,t)\cos kx$ is assumed. This form allows the wavelength of the perturbation to be specified. The amplitude and phase of the wave are found as functions of y, p, and t by solving an initial value problem in ξ_1 and ξ_2. Derivatives with respect to x are exact. Derivatives with respect to y, p, and t must be approximated by finite differences.

The y and p structure of the wave are defined on a grid in the y-p plane. The grid spacing must be sufficiently small so that the structure of both the mean state and the perturbation may be resolved. In particular, it must be small enough so that truncation error in the finite difference representation of derivatives does not lead to serious errors in the solution. African waves are mainly confined to the region between 5°N and 25°N, a distance of about 2000 km. Significant shears are present on a scale of 1000 km. (Refer to Figure 2.5) In order to resolve this structure, a horizontal grid spacing, Δy, of 125 km is used. As seen from Figure 2.4, the vertical extent of the waves is about 500 mb. A vertical grid spacing, Δp, of 200 mb is used to resolve this structure. A relatively larger value of Δp is used than Δy because the dynamical

coupling of the vertical levels is much weaker than the horizontal coupling.

An efficient grid scheme is defined by considering the various terms of (1) - (5) which require a finite difference representation. (1) requires no finite differencing of perturbation quantities. (2) requires that $\frac{\partial \phi'}{\partial y}$ be defined at the same points as v'. The diagnostic equations (4) and (5) require that $\frac{\partial \phi'}{\partial p}$ be defined where T' is defined, and that both $\frac{\partial v'}{\partial y}$ and $\frac{\partial \omega'}{\partial p}$ be defined where u' is defined. Using centered differences to define $\frac{\partial}{\partial y}$ and $\frac{\partial}{\partial p}$, these requirements suggest the staggered grid system shown in Figure 4.1. u', v', and ϕ' are all defined at the same vertical levels. T' and ω' are defined at levels midway between two u'-v'-ϕ' levels. u', T', ϕ', and ω' are defined at the same latitudes; v' is defined at alternate latitudes. Because the mean state does not change with time, the mean state variables may simply be defined at those points at which they are needed. Terms which require a perturbation variable at a point at which that variable is not defined (such as the Coriolis terms in the momentum equations) are handled by taking a linear average of the nearest points. With this scheme, all finite differences are properly centered and taken over one grid interval in the appropriate direction. In only one term, $\frac{\partial [\bar{T}]}{\partial y} v'$ in (3), is a four point average of a perturbation quantity required. Four other terms require a two point average.

Although the simple centered difference spatial derivative is quite satisfactory, the analogous time scheme is not acceptable. The centered difference, of leapfrog, time scheme introduces two solutions: one corresponding to even numbered time steps, the other to odd. The two solutions quickly become decoupled, and the results become invalid. To avoid this difficulty, an alternate scheme, the Heun scheme, is used.

Figure 4.1. Cross section in the y-p plane showing arrangement of grid points. v' is computed at points denoted by x, u' and ϕ' are computed at points denoted by $\cdot$. ω' and T' are computed at points denoted by +.

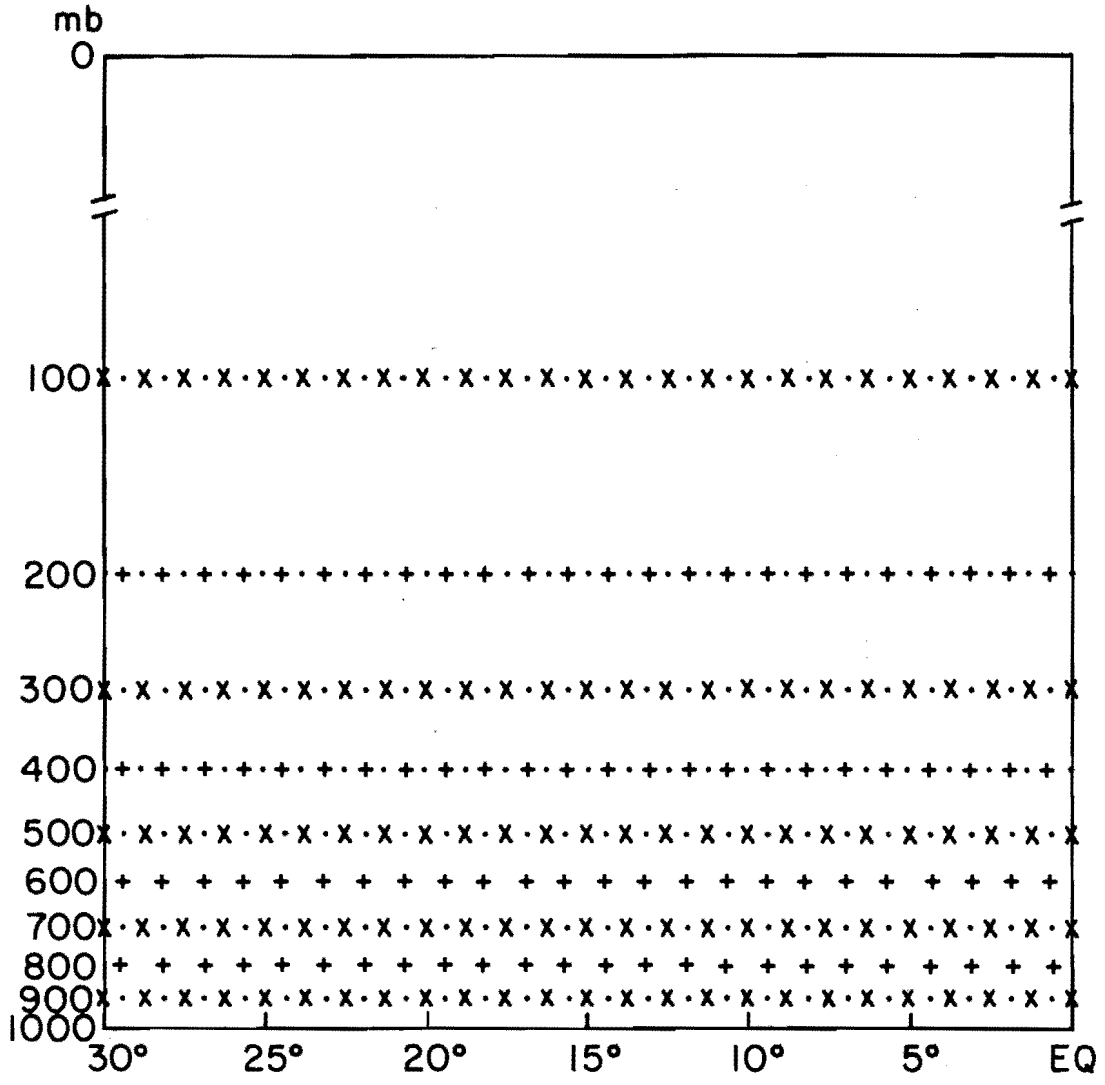
mb
0
100
200
300
400
500
600
700
800
900
1000
30°
25°
20°
15°
10°
5°
EQ

This is a two step method for computing time derivatives. If $\frac{\partial f}{\partial t} = g(t)$, then values of f at successive time steps are computed as follows.

$$f^{(n+1)} = f^n + g^n \Delta t$$

$$f^{n+1} = \frac{1}{2} [f^{(n+1)} + f^n + g^{(n+1)} \Delta t] \qquad (6)$$

The superscript n refers to the time step. (n) refers to an intermediate value which must be computed in order to obtain the value of the function at the next time step. This scheme was used successfully by Lorenz (1963) for long term integration. Like the leapfrog scheme, it has truncation errors which are of second order in Δt. However, the Heun scheme does introduce a small amplification factor of the form $A = (1 + \frac{1}{4} p^4)^{1/2}$, where $p \equiv kc_r \Delta t$. (Lilly, 1965) As long as p is sufficiently small, this should not adversely affect the results.

The appropriate time step depends on the types of motions which are present in the system under consideration. Courant, Friedrichs, and Lewy (1928) showed that computational stability requires that the condition $\frac{c_s \Delta t}{\Delta s} < 1$ be satisfied. Here, c_s is the $\hat{s}$ component of the phase velocity of the most rapidly moving wave, and Δs is the grid spacing in the $\hat{s}$ direction. Since the primitive equations permit the existence of rapidly propagating internal gravity waves; the required time step is on the order of a few minutes. This is sufficiently small so that the amplification factor inherent in the Heun differencing scheme is less than $1 + 10^{-7}$ even after 3000 time steps. Since an African wave takes about five days to propagate from the apparent source region to the west coast of Africa, the integration must be carried out for approximately

this length of time. With the value of Δt required for computational stability, this requires about 2500 time steps.

Since African waves are observed only in a limited part of the atmosphere, it is not necessary to solve the equations on the entire globe. Indeed, rectangular, rather than spherical, geometry is assumed in writing the equations on a beta-plane. The equations are applied to a latitudinal channel of the atmosphere. Because only the amplitudes of the spectral components are computed, the longitudinal extent of the channel is not important. However, care must be exercised in choosing the width and depth of the channel, and in specifying the behavior of the solution at the boundaries.

The lateral boundaries are relatively easy to handle. The wave amplitudes are large only between 5°N and 25°N, although there is some evidence of weak wave activity at the equator. The model assumes that the wave is strictly confined to the latitude band between the equator and 30°N. The meridional wind perturbation, v', is constrained to be zero at these latitudes, so there can be no fluxes across the boundaries. It is not necessary to impose lateral boundary conditions on any other variables, because of the way in which the grid is set up.

The upper and lower boundaries pose a more serious problem. At the upper boundary, there must be no inflow of energy. This condition may be achieved by forcing the vertical velocity, ω', to vanish there. At the surface of the earth, vertical motions should likewise vanish. However, the earth's surface does not, in general, correspond to a constant pressure surface. For simplicity, however, ω' is assumed to be zero at the lower boundary of the model, $p = p_{oo}$. This assumption would

introduce serious errors only if the terrain were very rough. Since the model is designed to investigate shear instabilities, without mountain effects, the assumption is justifiable.

Computationally, (5) requires one boundary condition on ω', and (4) requires one condition on ϕ'. Physical insight, however, provides two boundary conditions on ω', and none on ϕ'. It is necessary, then, to use the second condition on ω' to derive a boundary condition on ϕ'. If the condition $\omega' = 0$ at $p = p_{oo}$ is enforced, then an alternative statement of the condition $\omega' = 0$ at $p = 0$ is $\int_{p_{oo}}^{o} dp \frac{\partial \omega'}{\partial p} = 0$. Furthermore, this condition must be met at all times. Then

$$\frac{\partial}{\partial t}\left\{ \int_{p_{oo}}^{o} dp \ \frac{\partial \omega'}{\partial p} \right\} = 0 \tag{7}$$

Using (5), this becomes

$$\frac{\partial}{\partial t}\left\{ \int_{p_{oo}}^{o} dp \left(\frac{\partial u'}{\partial x} + \frac{\partial v'}{\partial y} \right) \right\} = 0$$

$$\int_{p_{oo}}^{o} dp \left(\frac{\partial}{\partial x}\frac{\partial u'}{\partial t} + \frac{\partial}{\partial y}\frac{\partial v'}{\partial t} \right) = 0 \tag{8}$$

If the momentum equations (1) and (2) are rewritten as

$$\frac{\partial u'}{\partial t} = \eta' - \frac{\partial \phi'}{\partial x} \tag{1a}$$

$$\frac{\partial v'}{\partial t} = \zeta' - \frac{\partial \phi'}{\partial y} \tag{2a}$$

then (8) becomes

$$\int_{p_{oo}}^{o} dp \left(\frac{\partial \eta'}{\partial x} + \frac{\partial \zeta'}{\partial y} - \frac{\partial^2 \phi'}{\partial x^2} - \frac{\partial^2 \phi'}{\partial y^2} \right) = 0$$

$$\int_{p_{oo}}^{o} dp \left(\frac{\partial^2 \phi'}{\partial x^2} + \frac{\partial^2 \phi'}{\partial y^2} \right) = \int_{p_{oo}}^{o} dp \left(\frac{\partial \eta'}{\partial x} + \frac{\partial \zeta'}{\partial y} \right) \tag{9}$$

Since the limits of integration are independent of x and y, the order of operations may be reversed, and the lefthand side of (9) becomes

$$\left(\frac{\partial^2}{\partial x^2} + \frac{\partial}{\partial y^2} \right) \int_{p_{oo}}^{o} dp \ \phi' \tag{10}$$

From (4), $\phi'(p) = - R \int_{p_{oo}}^{p} dp^* \frac{T'}{p^*} + \phi'(p_{oo})$. Substituting this expression into (10) yields

$$\left(\frac{\partial^2}{\partial x^2} + \frac{\partial^2}{\partial y^2} \right) \left\{ p_{oo} \ \phi'(p_{oo}) - R \int_{p_{oo}}^{o} dp \int_{p_{oo}}^{p} dp^* \frac{T'}{p^*} \right\} = \int_{p_{oo}}^{o} dp \left(\frac{\partial \eta'}{\partial x} + \frac{\partial \zeta'}{\partial y} \right)$$

Since T', η', and ζ' can all be computed without ϕ', this is an elliptic equation in the boundary condition $\phi'(p_{oo})$:

$$\left(\frac{\partial^2}{\partial x^2} + \frac{\partial^2}{\partial y^2} \right) \phi'(p_{oo}) = \frac{1}{p_{oo}} \int_{p_{oo}}^{o} dp \left\{ \frac{\partial \eta'}{\partial x} + \frac{\partial \zeta'}{\partial y} + \frac{\partial^2}{\partial x^2} + \frac{\partial^2}{\partial y^2} R \int_{p_{oo}}^{p} dp^* \frac{T'}{p^*} \right\} \tag{11}$$

This specification of $\phi'(p_{oo})$, in conjunction with the requirement that $\omega'(p_{oo}) = 0$, assures that $\omega' = 0$ at the top of the atmosphere, thereby imposing a rigid lid on the atmosphere. This condition eliminates the possibility of a false input of energy at the upper boundary, but it can introduce reflections from the rigid lid. In order to prevent these reflections from contaminating the results at lower levels, a radiation condition is required. Such a condition allows energy to be exported from the region of interest, but does not allow a spurious energy source. The easiest manner in which to simulate a radiation condition without introducing additional levels near the upper boundary, is to include a Rayleigh friction term in the momentum equations (1) and (2) at upper levels of the model. This term assumes the form $\vec{F}_R = - \alpha(p) \vec{v}'$. The values of α used in the model were $\alpha(100 \text{ mb}) = .4 \text{ day}^{-1}$, $\alpha(300 \text{ mb}) = .15 \text{ day}^{-1}$, $\alpha(p > 300 \text{ mb}) = 0$. This choice of α effectively damps out reflections from the top of the atmosphere. Experiments with different values of α showed that the solution at 500 mb and below is unaffected by the choice of α.

Values of the prognostic variables u', v', and T' must be specified initially. Since T' is expected to remain small throughout the integration, it is initialized to zero. To avoid adjustment problems, a geostrophic initial state is specified. With T' equal to zero, this means that $\frac{\partial u'}{\partial p}$ and $\frac{\partial v'}{\partial p}$ must also be equal to zero. Then in order to satisfy the boundary condition on ω', $\frac{\partial u'}{\partial x} + \frac{\partial v'}{\partial y}$ must vanish everywhere. This means that the initial state is barotropic. This is consistent with the notion that tropical motions are essentially horizontal. The horizontal structure of the initial perturbation is fairly arbitrary, the only constraint being that it satisfy the boundary conditions at the equator

and 30°N. The form of v' used in most applications of the model is a gaussian centered at 15°N. The amplitude of v' is reduced by a factor 1/e within 2.5° of its maximum, and by a factor .01 within 6°.

With the initial conditions specified, ω' is computed from (5), subject to the condition $\omega' = 0$ at $p = p_{oo}$. η' and ζ' are then formed, and (11) is solved for ϕ' at $p = p_{oo}$. Values of ϕ' at other pressure levels are found using (4). Finally, new values for u', v', and T' are computed, using (1a), (2a), and (3). From this point the process repeats.

2. Specification of the Model Parameters

The mean zonal flow $[\bar{u}]$ must be specified before the model can be run. $[\bar{u}]$ is based on the mean state of the African atmosphere in August as determined by Burpee (1972). His data was interpolated subjectively to the required resolution. The model requires that $[\bar{u}]$ be defined at all points at which u', v', or T' is defined. This means the horizontal resolution of $[\bar{u}]$ is .625°. Since barotropic instability is expected to be an important mechanism in wave generation, and because barotropic instability depends critically on the behavior of $\frac{\partial^2[\bar{u}]}{\partial y^2}$, the horizontal interpolation is crucial. In order to avoid the introduction of spurious small scale fluctuations in $\frac{\partial^2[\bar{u}]}{\partial y^2}$ without smoothing the physical features out of the flow, the following procedure was followed. First, values of $\frac{\partial^2[\bar{u}]}{\partial y^2}$ were computed on the coarse, irregular grid on which data is available. A smooth curve was fit subjectively to these points. The values of $\frac{\partial^2[\bar{u}]}{\partial y^2}$ at .625° intervals were then integrated with respect to y to obtain $[\bar{u}]$ at all points. This process was applied at every level up to 300 mb. Since the purpose of the model is to investigate the instability of the

low level jet, the upper jet at 200 mb is not included in the $[\bar{u}]$ field. The model atmosphere is barotropic above 300 mb. The resulting field of $[\bar{u}]$ is shown in Figure 4.2, along with the field of $\frac{\partial^2[u]}{\partial y^2}$. Once $[\bar{u}]$ is defined, $\frac{\partial[\bar{u}]}{\partial y}$ and $\frac{\partial[\bar{u}]}{\partial p}$ are easily defined at those grid points at which u' is computed, using centered differences.

A knowledge of the mean temperature field is also required. Values of $\tilde{T}$ are needed to specify the static stability, σ. Values of $[\bar{T}]^*$ are needed to specify the meridional gradient of the temperature, and to specify the deviations from σ, $\left(\frac{\partial[\bar{T}]^*}{\partial p} - \frac{\kappa[\bar{T}]^*}{p}\right)$. Since both $[\bar{v}]$ and $[\bar{\omega}]$ have been assumed to vanish, the thermal wind equation (3.13) determines the value of $\frac{\partial[\bar{T}]}{\partial y}$ at all points. These values were used to compute $[\bar{T}]^*$, the deviation of $[\bar{T}]$ from its average value on a constant pressure surface. These values were used to compute $\left(\frac{\partial[\bar{T}]^*}{\partial p} - \frac{\kappa[\bar{T}]^*}{p}\right)$. Values of $[\bar{\phi}]^*$ were computed hydrostatically from $[\bar{T}]^*$. The fields of $[\bar{T}]^*$ and $[\bar{\phi}]^*$ are shown in Figure 4.3. In order to specify σ, an average value of θ at each pressure level was obtained from the temperature structure reported by Burpee (1972). These values were differentiated to find σ. The resulting profile of σ is shown in Figure 4.4. σ is negative at all levels, and its magnitude increases upward. The contribution to the stability due to $\left(\frac{\partial[\bar{T}]^*}{\partial p} - \frac{\kappa[T]^*}{p}\right)$ is generally positive in the northern part of the region at low levels, and negative near the equator. The positive values of $\left(\frac{\partial[\bar{T}]^*}{\partial p} - \frac{\kappa[\bar{T}]^*}{p}\right)$ may tend to destabilize the atmosphere, but their magnitude is at most about 10% of the magnitude of σ. Thus, the overall stability of the atmosphere to gravitational perturbations is essentially determined by σ. It is slightly stable at low levels, and becomes more stable at upper levels.

Figure 4.2. Fields of $[\bar{u}]$ and $\frac{\partial^2[\bar{u}]}{\partial y^2}$ used in linear model.

$[\bar{u}]$ contour interval = 6 m sec^{-1}

$\frac{\partial^2[\bar{u}]}{\partial y^2}$ contour interval = .8 x 10^{-10} m^{-1} sec^{-1}

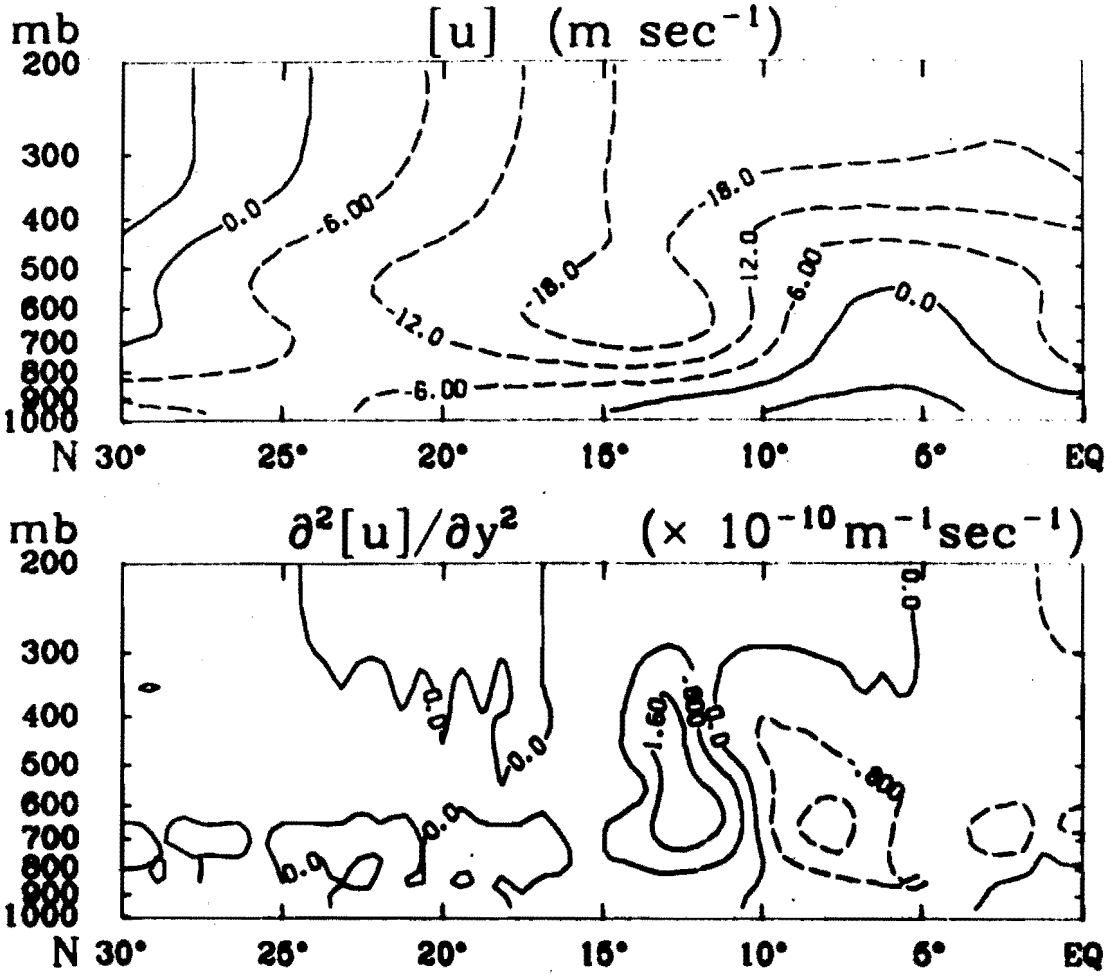
mb
[u] (m sec⁻¹)
200
300
400
500
600
700
800
900
1000
0.0
-6.00
-12.0
-18.0
12.0
6.00
N 30°
25°
20°
15°
10°
6°
EQ
mb
∂²[u]/∂y² (× 10⁻¹⁰m⁻¹sec⁻¹)
200
300
400
500
600
700
800
900
1000
0.0
N 30°
25°
20°
15°
10°
6°
EQ

Figure 4.3. Geostrophically determined temperature and geopotential fields for the mean state.
$[\bar{T}]^*$ contour interval = 2.0 C
$[\bar{\phi}]^*$ contour interval = 200 m^2 sec^{-2}

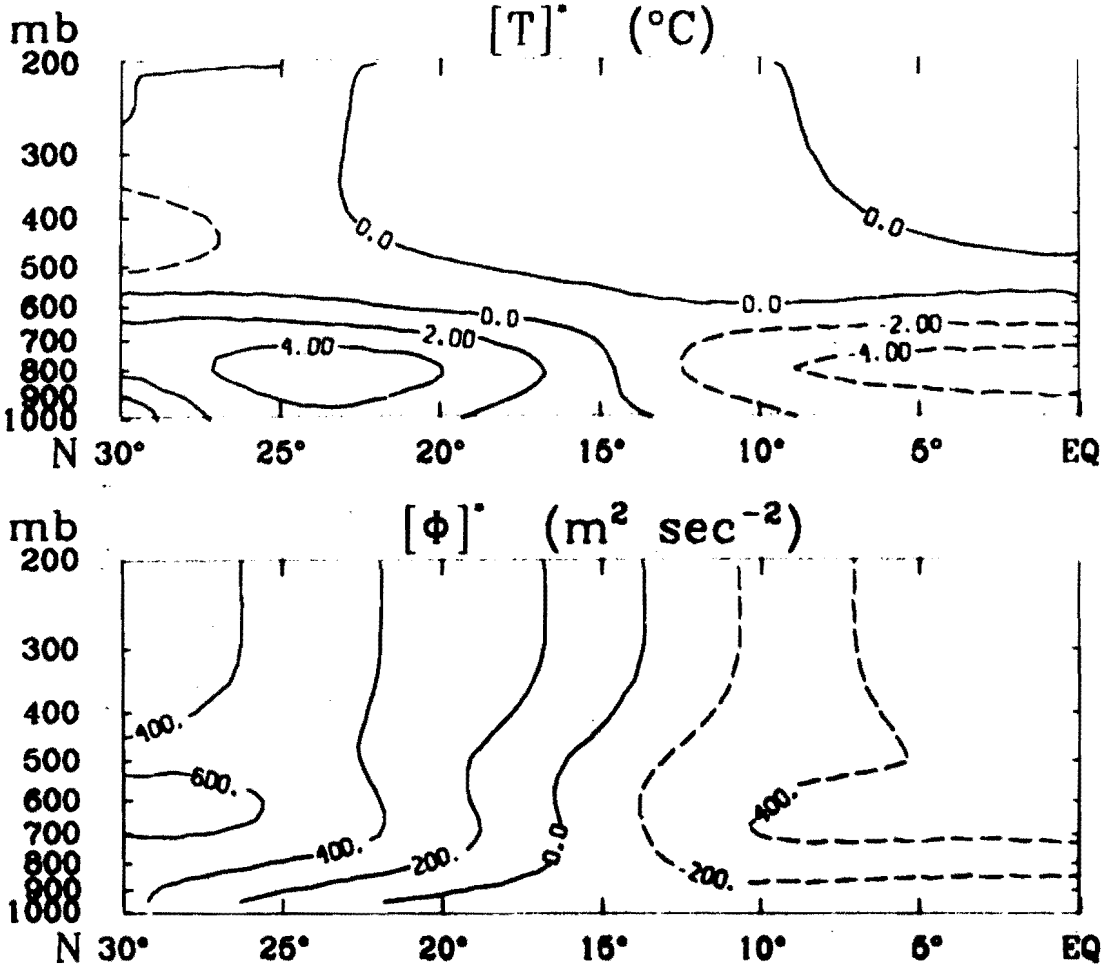
mb
[T]* (°C)
200
300
400
500
600
700
800
900
1000
0.0
0.0
0.0
2.00
4.00
-2.00
-4.00
N 30° 25° 20° 15° 10° 5° EQ
mb
[Φ]* (m² sec⁻²)
200
300
400
500
600
700
800
900
1000
400.
600.
400.
200.
0.0
400.
-200.
N 30° 25° 20° 15° 10° 5° EQ

Figure 4.4. Vertical profile of σ (°C mb^{-1}).

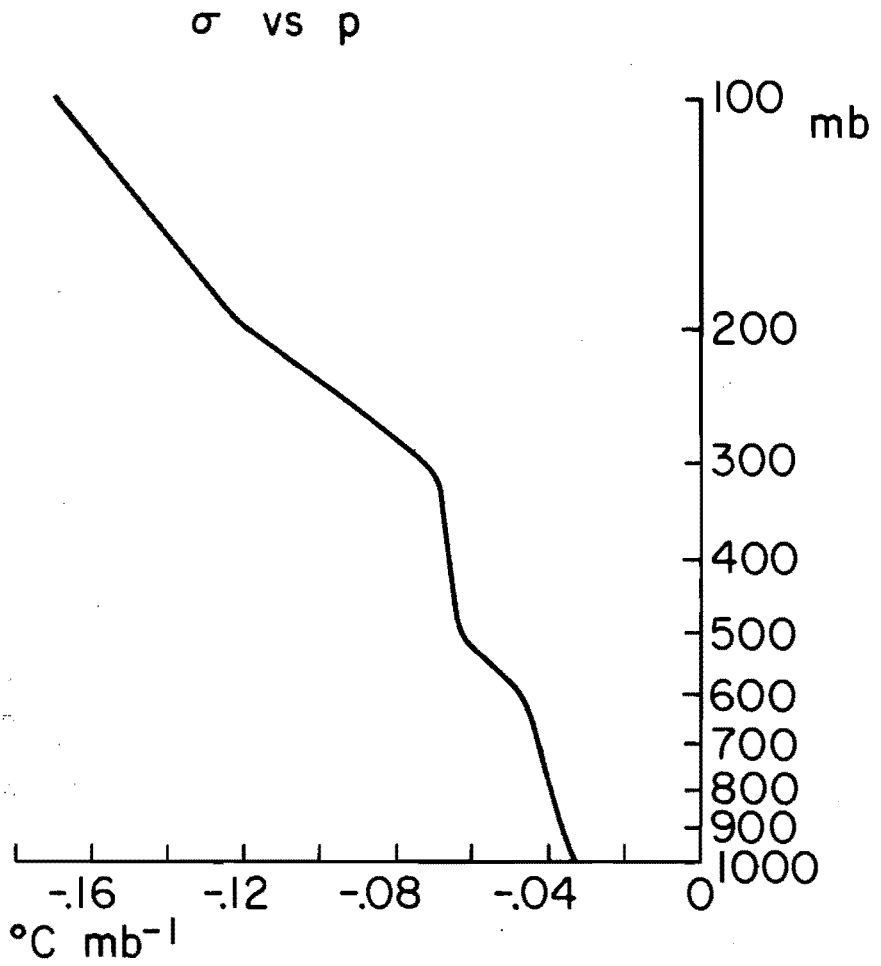
σ vs p
100
mb
200
300
400
500
600
700
800
900
1000
-.16
-.12
-.08
-.04
0
°C mb⁻¹

The configuration of the low level jet is determined by $[\bar{u}]$. However, the magnitude of the jet may be adjusted by varying an overall multiplicative factor, U. By changing U, the stability of jets of different intensities may be studied. This is desirable because it allows the minimum jet intensity required for instability to be found. Furthermore, because Burpee's data represent an eight year average, and the jet is known to vary in both time and space, the actual intensity of the jet at any given time can be significantly greater than the average value. Since $[\bar{T}]^*$ is computed by the thermal wind equation, its magnitude also changes when U is changed. The value of U used in Figures 4.2 and 4.3 is 22.6 m sec^{-1}.

The model only determines the amplitude and phase of the perturbation variables as functions of time and space. The wavelength, λ, of the disturbance must be specified. By varying λ, the stability of a given jet to perturbations of different wavelengths can be studied.

Equation (3) includes a diabatic heat source Q'. For most applications of the model, the motions of the atmosphere were assumed to be adiabatic, so that $Q' = 0$. By specifying $Q' \neq 0$, the effects of moisture on the instability can be crudely parameterized. The specification of Q' depends upon the fact that when saturated air is lifted, water vapor condenses, releasing latent heat.

The zonally averaged, time independent moisture field is given by $[\bar{q}]$. Then the rate at which moisture is converged into a column of the atmosphere of unit cross sectional area is given by:

$$M = -\frac{1}{g} \int_{o}^{p_{oo}} dp \left\{ \frac{\partial}{\partial x} (u[q]) + \frac{\partial}{\partial y} (v[q]) \right\}$$

$$M = -\frac{1}{g} \int_{o}^{p_{oo}} dp \left\{ [\bar{q}] \left(\frac{\partial u'}{\partial x} + \frac{\partial v'}{\partial y} \right) + \frac{\partial [\bar{q}]}{\partial y} v' \right\}$$

The maximum possible latent heat release would occur if all the moisture converged into a column were to condense. In that case, the amount of energy released per unit mass and time is $\frac{g}{p_{oo}}$ LM, where L is the latent heat of condensation.

The quantity M depends on the perturbation wind field. It is itself a perturbation quantity, and as such may be written as $M = M_1 \sin kx + M_2 \cos kx$. This quantity can assume both positive and negative values. Only the heat released in the atmosphere due to condensation is of interest here. Any evaporational cooling due to the divergence of moisture is negligible. Then E', the energy released in a column of the atmosphere is given by

$$E = \begin{cases} \frac{g}{p_{oo}} LM & M > 0 \\ 0 & M \leq 0 \end{cases}$$

This type of term cannot be handled in a linear model, which does not allow coupling of different wavenumbers. Therefore, E' must be expanded as a fourier series in x, and only the term in kx retained. Then

$$E' = \pm \frac{1}{2} \frac{g}{p_{oo}} L \{M_1 \sin kx + M_2 \cos kx\}$$

where the sign depends on the relative magnitudes of M_1 and M_2.

The vertical distribution of E' in a column is specified on the basis of empirical evidence. Figure 4.5 shows the vertical distribution of heating determined by Reed and Recker (1971) in a study of easterly waves in the Pacific. This is the distribution assumed by the model. Also shown in Figure 4.5 is the distribution of $[\bar{q}]$ as determined by Newell (1972).

With this formulation of the heating due to condensation, the diabatic heat source in (3) is given by $Q' = \xi(p) \frac{E'}{c_p}$, where $\xi(p)$ is the heating distribution shown in Figure 4.5. This treatment of the effects of moisture is admittedly crude, but it should give a reliable order of magnitude estimate of the influence of latent heat release on the generation of African waves. It should over estimate the magnitude of E', since it assumes that all the moisture which is converged into a column condenses. In fact, the air is far from saturated, so some of the converged moisture must remain in the vaporized state.

3. Interpretation of Model Results

In order to get a maximum of useful information from the model, the results must be treated in such a way as to display the features of the solution most clearly. One of the most important physical quantities to be considered in an instability study is the energy of the disturbance, and how it changes with time. The kinetic and available potential energies of the perturbation are easily computed using finite difference analogs to their definitions. These may be finite differenced with respect to time to give $\frac{\partial EKE}{\partial t}$ and $\frac{\partial EAPE}{\partial t}$.

Figure 4.5. a) Vertical distribution of heating due to condensation. (after Reed and Recker, 1971)

b) Distribution of moisture at 5°E. Contour interval = 3 gm kg^{-1}. (after Newall et al., 1972)

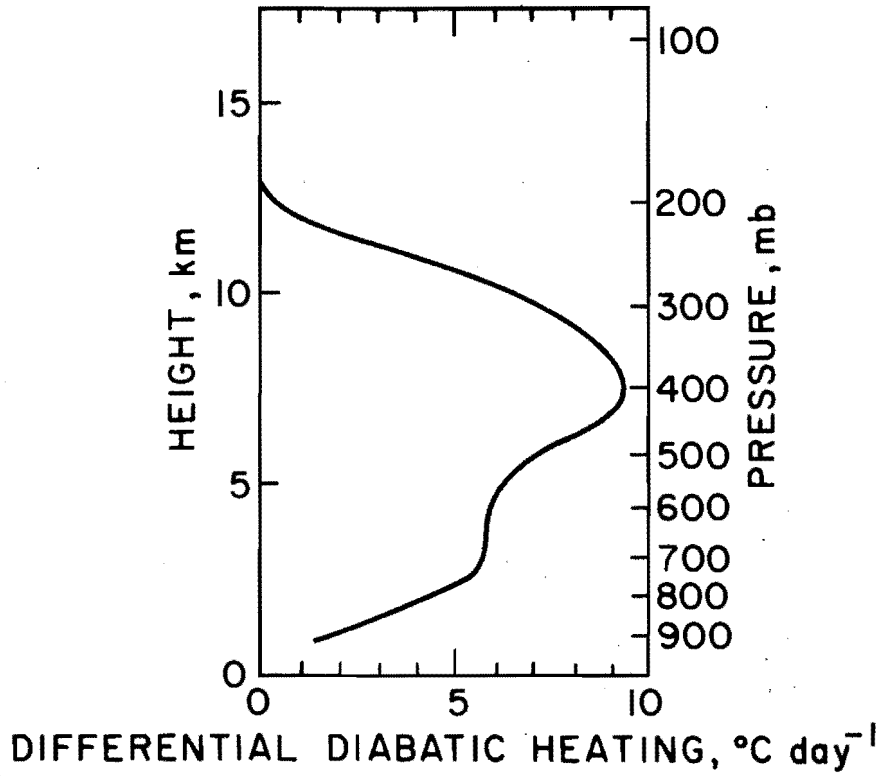
HEIGHT, km
PRESSURE, mb
0
5
10
15
100
200
300
400
500
600
700
800
900
0
5
10
DIFFERENTIAL DIABATIC HEATING, °C day⁻¹

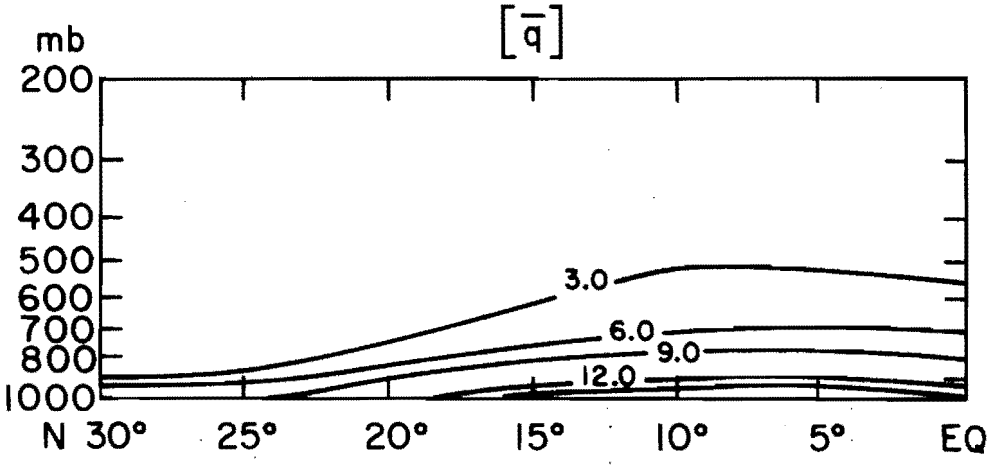
[q̄]
mb
200
300
400
500
600
700
800
1000
3.0
6.0
9.0
12.0
N 30°
25°
20°
15°
10°
5°
EQ

In a linear model, the disturbance may be expected to grow exponentially with time, making it difficult to handle such quantities as EKE or $\frac{\partial EKE}{\partial t}$ over long time intervals. A more useful measure of the growth of disturbances is the growth rate, the rate at which the disturbance grows (or decays) with respect to the total magnitude of the disturbance. The usual definition of the growth rate is based on a normal mode analysis, in which any perturbation may be represented by $Re\{\xi exp[ik(x-ct)]\}$. This is an oscillating function of order 1, multiplied by an amplitude, $\xi exp(kc_i t)$, which grows without limit (for $c_i > 0$) as t increases. The rate at which the amplitude increases, kc_i, is the growth rate. During each time interval $\tau = 1/kc_i$, the amplitude increases by a factor e.

An alternate derivation of the growth rate requires the formation of the energy of the disturbance. The energy per unit mass averaged over one wavelength is $E = \frac{1}{4}|\xi|^2 \exp(2kc_i t)$. $\frac{\partial E}{\partial t}$ is then given by $2kc_i E$. The growth rate, kc_i, may be defined as $\frac{1}{2}\frac{\partial E/\partial t}{E}$.

When a single normal mode is present, the two definitions give identical values of the growth rate. For a given disturbance, this growth rate is independent of time. However, when the disturbance is a superposition of a number of normal modes, the definition involving c_i becomes ambiguous, because each normal mode has a different value for c_i. The alternate definition, $\frac{1}{2}\frac{\partial E/\partial t}{E}$ is well defined, regardless of how many normal modes of the system are excited. This quantity is time dependent (if more than one mode is present). The growth rate changes as the relative magnitudes of the different modes change.

Since the model contains no explicit information regarding the normal modes of the system, the second formulation of the growth rate must be used.

There are three growth rates which are relevant to the African wave system: those based on EKE, EAPE, and ETE. These are given by

$$\text{growth rate (EKE)} = \frac{1}{2} \frac{\partial EKE/\partial t}{EKE} \tag{12}$$

$$\text{growth rate (EAPE)} = \frac{1}{2} \frac{\partial EAPE/\partial t}{EAPE} \tag{13}$$

$$\text{growth rate (ETE)} = \frac{1}{2} \frac{\partial EKE/\partial t + \partial EAPE/\partial t}{EKE + EAPE} \tag{14}$$

Another important physical characteristic of the disturbance is its phase speed in the $\hat{x}$ direction. As is the case for the growth rate, the treatment of the phase speed is complicated by the presence of a superposition of normal modes. Since the model computes the amplitude and phase of the perturbation at every point, a useful definition of the period of the wave, T, is the time required for the phase of the wave to change from $\alpha + 2\pi$ at a given point. The phase speed is then given by $\frac{\lambda}{T}$. This is a point-wise definition. Presumably, the phase speed so defined could be quite different at every grid point. However, this is not the case. The phase speed varies by only a small amount throughout the central portion of the perturbation where ETE is large. Therefore, a point in the center of the domain (15°N, at 700 mb) is arbitrarily chosen as the point at which the phase speed is defined.

Further details of the characteristics of the waves may be seen from the amplitudes and phases of the perturbation variables as functions of space. These are output by the model directly. The variation of the phase of the disturbance with respect to latitude and pressure is of particular importance because this gives the horizontal and vertical slopes of the wave axis.

Essential information about the mechanisms by which the waves are generated is contained in the local energy conversion terms. If the atmosphere is divided into segments of length λ, width Δy, and depth Δp, the local change of energy in each segment can be computed. The equations governing the time rates of change of kinetic and available potential energy throughout the domain were derived in Chapter 3. The local change of energy in each segment is found in the same manner, except that the integral is over a single element of mass $\Delta M = \lambda \Delta y \frac{\Delta p}{g}$ and surface area $\Delta s = \lambda \Delta y$, instead of the entire atmosphere. The resulting equations, to be evaluated at each grid point, are:

$$\frac{\partial EKE}{\partial t} = \frac{\Delta p}{g} \left\{ - \frac{\partial [\bar{u}]}{\partial y} [u'v'] - \frac{\partial [\bar{u}]}{\partial p} [u'\omega'] - \frac{R}{p} [T'\omega'] - \frac{\partial}{\partial y} [\phi'v'] - \frac{\partial}{\partial p} [\phi'\omega'] \right\} \tag{15}$$

$$\frac{\partial EAPE}{\partial t} = \frac{\Delta p}{g} \left\{ \frac{R}{p\sigma} \frac{\partial [\bar{T}]}{\partial y} [T'v'] + \frac{R}{p} [T'\omega'] + \frac{R}{p\sigma} \left(\frac{\partial [\bar{T}]^*}{\partial p} - \frac{\kappa [\bar{T}]^*}{p} \right) [T'\omega'] \right.$$

$$\left. - \frac{R}{p\sigma} [T'Q'] \right\} \tag{16}$$

For convenience, the following definitions are made:

$$CE_1 \equiv - \frac{\Delta p}{g} \frac{\partial [\bar{u}]}{\partial y} [u'v'] \tag{17}$$

$$CE_2 \equiv - \frac{\Delta p}{g} \frac{\partial [\bar{u}]}{\partial p} [u'\omega'] \tag{18}$$

$$CE_3 \equiv \frac{\Delta p}{g} \frac{R}{p\sigma} \frac{\partial [\bar{T}]}{\partial y} [T'v'] \tag{19}$$

$$CE_4 \equiv \frac{\Delta p}{g} \frac{R}{p} [T'\omega'] \tag{20}$$

$$CE_5 \equiv - \frac{\Delta p}{g} \frac{\partial}{\partial y} [\phi' v'] \tag{21}$$

$$CE_6 \equiv - \frac{\Delta p}{g} \frac{\partial}{\partial p} [\phi' \omega'] \tag{22}$$

$$CE_7 \equiv \frac{\Delta p}{g} \frac{R}{p\sigma} \left(\frac{\partial [\bar{T}]^*}{\partial p} - \frac{\kappa [\bar{T}]^*}{p} \right) [T' \omega'] \tag{23}$$

$$CE_8 \equiv - \frac{\Delta p}{g} \frac{R}{p\sigma} [T' Q'] \tag{24}$$

The physical significance of CE_1, CE_2, CE_3, and CE_4 has been discussed in Chapter 3. CE_1 and CE_2 represent the conversion of ZKE to EKE, CE_3 represents the conversion of ZAPE to EAPE, and CE_4 represents the conversion of EKE to EAPE. The additional terms, CE_5 and CE_6, represent boundary fluxes. Because the boundary conditions imposed on the model do not allow for any energy flux across the model boundaries, these terms vanish when the equations are integrated over the entire model atmosphere. However, they do not necessarily vanish in an individual segment. CE_5 represents a redistribution of EKE by the perturbation height (pressure) field as it responds to the changing horizontal velocity perturbation. This is essentially a pressure-work term, and is important to the local energetics of the wave. CE_6 is an analogous term, representing adjustments in the vertical. However, CE_6 is always at least two orders of magnitude smaller than the other terms contributing to $\frac{\partial EKE}{\partial t}$. Its numerical value is negligible; it is included here only for the sake of completeness. The term CE_7 is similar to CE_4. It represents the conversion of EKE to EAPE by means of overturning. The difference between the two terms is that the stability of the atmosphere is due to the deviations from the mean in

CE_7, whereas the mean static stability is used to define CE_4. CE_8 is the addition of energy to the system by means of diabatic heating.

The relative magnitudes of the different energy conversion terms indicate the importance of the various mechanisms in the generation of African waves. The distribution of the conversions with respect to latitude and pressure indicates which features of the mean flow supply significant amounts of energy to the wave.

4. Verification of the Model

Before applying the model to the actual mean state of the African atmosphere, it is useful to consider a few simplified cases, for which some features of the solution may be derived analytically.

One such case is that of a mean state which is uniform with respect to p, and which has a horizontal structure given by $[\bar{u}] = -U\sin^2 \frac{\pi y}{2a}$. The flow is confined to a channel with rigid walls at $y = 0$ and $y = 2a$. The analysis of this case differs very little from that done by Kuo (1949) for a westerly flow with the same profile, except that the long wave cutoff for instability found by Kuo does not exist for the easterly jet. (Nitta and Yanai, 1969). This particular flow is of additional interest because it may be considered a first order approximation to the 700 mb flow over Africa. The mean flow is said to have a critical point at every point at which $\frac{\partial^2[\bar{u}]}{\partial y^2} - \beta = 0$. The existence of such points is significant, because the flow cannot support instabilities unless $\frac{\partial^2[\bar{u}]}{\partial y^2} - \beta$ changes sign. It can be shown (Kuo, 1949) that if there is exactly one critical point y_k in the domain, then exactly one neutral wave can exist, with $c_i = 0$, $c_r = [\bar{u}](y_k)$, and $\lambda = \lambda_k$. For the case under consideration, there is one and only one critical point when

$U = \frac{2a^2\beta}{\pi^2}$. The critical point is located at $y_k = a$. The wavelength of the neutral wave is given by $\lambda_k = \frac{4a}{\sqrt{3}}$. The barotropic equation can be solved analytically for the one case of a neutral wave with $\lambda = \lambda_k$ and $U = \frac{2a^2\beta}{\pi^2}$. Then, the streamfunction is given by $\psi' = A \sin \frac{\pi y}{a} \cos \alpha (x-c_r t)$, where $\alpha = \frac{2\pi}{\lambda_k}$ and $c_r = [\bar{u}](y_k)$. For a channel between the equator and 30°N, the values of the relevant parameters are $U = 10.1$ m sec^{-1}, $\lambda_k = 3500$ km, $c_r = -10.1$ m sec^{-1}.

The model was run using $[\bar{u}] = -10.1 \sin^2 \frac{\pi y}{2a}$ and $\lambda = 3500$ km. The initial perturbation v' was specified as a sine, centered at the midpoint of the channel. A time-latitude cross section of the meridional perturbation is shown in Figure 4.6. The model distorts the shape of the normal mode only slightly. The amplitude of the perturbation at any given latitude is essentially constant over three periods of the wave. There is a slight increase in the total energy of the disturbance, but the growth rate implied by the change in energy is less than 5×10^{-3} day^{-1}. The phase speed of the wave is seen from the lines of constant phase in the figure. At any given time, the phase of the wave is independent of latitude, indicating that all parts of the wave are moving with the same phase speed, as required if only one normal mode is present. The phase speed determined from the figure is -10 m sec^{-1}, as predicted by the theory.

According to the theory, if $U > 10.1$ m sec^{-1}, waves with $\lambda > 3500$ km are unstable; waves with $\lambda < 3500$ km decay. In all cases, c_r should be greater than $[\bar{u}](y_k)$. In order to further test the model, two additional cases were run, with $U = 11.3$ m sec^{-1}; and $\lambda = 1200$ km, $\lambda = 3600$ km. For this case, $[\bar{u}](y_k) = -10.7$ m sec^{-1}. The amplitude

Figure 4.6. Time latitude cross section of neutral wave solution for $[\bar{u}] = - U \sin^2 \frac{\pi y}{2a}$. Solid lines are amplitude of v'. Dashed lines are lines of constant phase of v'. U = 10.1 m sec^{-1}, λ = 3500 km. v' contour interval = .01 m sec^{-1} phase contour interval = 90°.

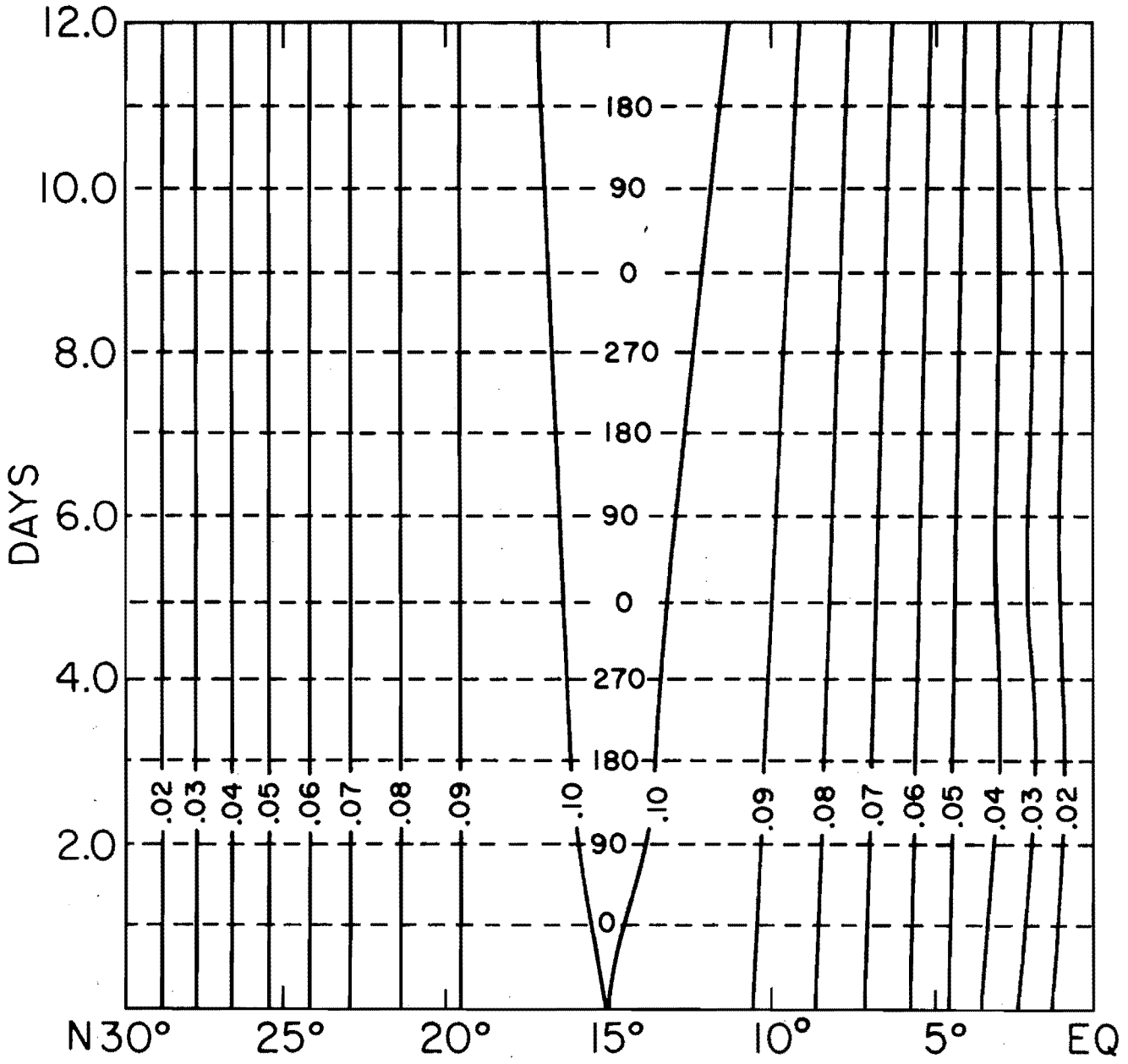
12.0
10.0
8.0
6.0
4.0
2.0
DAYS
180
90
0
270
180
90
0
270
180
90
0
.02
.03
.04
.05
.06
.07
.08
.09
.10
.10
.09
.08
.07
.06
.05
.04
.03
.02
N30°
25°
20°
15°
10°
5°
EQ

and phase of v' for the two cases are shown in Figures 4.7 and 4.8. The neutral wave solution is no longer a normal mode of the system, so the shape of the disturbance need not remain constant with time. For the case of the short wave, Figure 4.7, the amplitude of v' decreases with time. The growth rate of the disturbance is about -.1 day^{-1}. The phase speed shows some dependence on y. The value of c_r computed at y_k is - 10.6 m sec^{-1}, which is greater than $[\bar{u}]$ at that point. The amplitude of the 3600 km wave grows with time. (Figure 4.8) The wavelength is only slightly greater than that of the neutral wave, so the growth rate is small, but positive. It is equal to .08 day^{-1}. The phase speed of this wave is fairly constant with respect to time and latitude, and is equal to - 10.8 m sec^{-1}, which is just slightly less than $[\bar{u}](y_k)$.

These results indicate that the model successfully solves the equations of motion when given a barotropic mean state. The numerical solution satisfies the constraints placed upon it by theoretical considerations quite closely.

It is more difficult to test the behavior of the model under baroclinic conditions. Most of the simple theoretical work which has been done on baroclinic theory has been applied to a quasi-geostrophic atmosphere at mid latitudes where the vertical shear of $[\bar{u}]$ is westerly, and approximately linear. Often, the perturbation is assumed to be independent of latitude. None of these conditions is directly applicable to the model. However, an attempt was made to compare the results of a slightly modified model to those of a theoretical, two level, quasi-geostrophic model.

Figure 4.7. Same as Figure 4.5, but for a damped disturbance. $U = 11.3$ m sec^{-1}, $\lambda = 1200$ km.

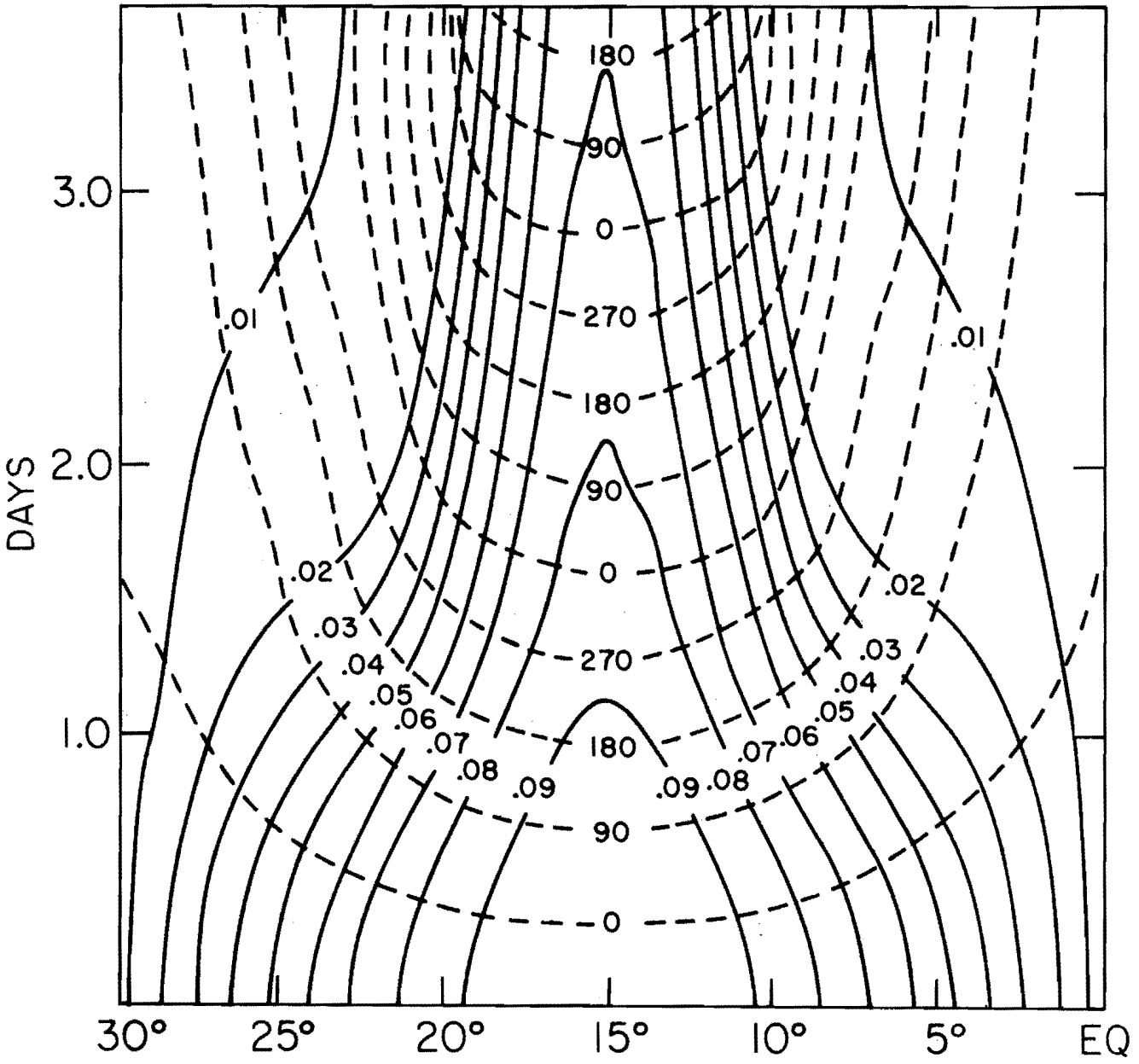
DAYS
3.0
2.0
1.0
30°
25°
20°
15°
10°
5°
EQ
180
90
0
270
180
90
0
270
180
90
0
.01
.02
.03
.04
.05
.06
.07
.08
.09
.09
.08
.07
.06
.05
.04
.03
.02
.01

Figure 4.8. Same as Figure 4.4, but for an amplified disturbance. $U = 11.3$ m sec^{-1}, $\lambda = 3600$ km, v' contour interval $= .02$ m sec^{-1}.

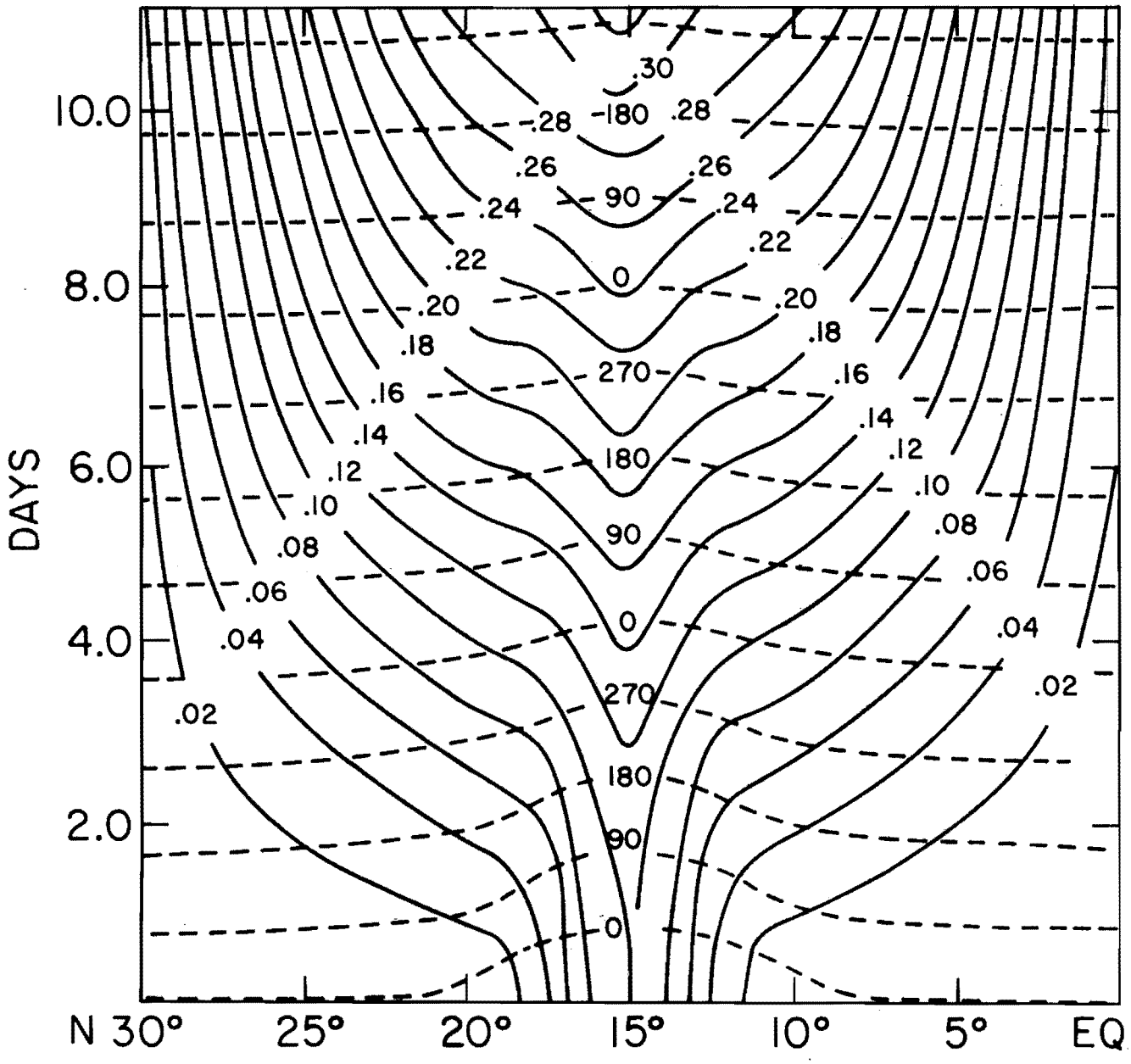
DAYS
10.0
8.0
6.0
4.0
2.0
N 30°
25°
20°
15°
10°
5°
EQ
.30
.28
.26
.24
.22
.20
.18
.16
.14
.12
.10
.08
.06
.04
.02
-180
90
0
270
180
90
0

By changing the value of the coriolis parameter, the center of the channel was moved from 15°N to 45°N without changing the width of the channel. The vertical resolution of the model was changed so that Δp = 400 mb. Then, velocities were computed at 800 mb and 400 mb. Temperature and vertical velocity were computed at 600 mb. The upper and lower boundary conditions were applied at 200 mb and 1000 mb, respectively. In this form, the model is similar, although not identical, to a typical two level quasi-geostrophic model, such as that discussed by Holton (1972).

An easterly shear of 12 m sec^{-1} between 1000 mb and 600 mb was prescribed, with $\frac{\partial[\bar{u}]}{\partial y} = 0$. According to quasi-geostrophic theory, a westerly shear of this magnitude should be unstable. The wavelength of maximum instability should be approximately 6000 km. The growth rates produced by the model for several different wavelength are shown in Figure 4.9. For wavelengths shorter than 2400 km, the waves are stable. For all other wavelengths tested, the waves grow. The most unstable wavelength is about 6000 km. Considering the differences between the theory and the model, this is considered good agreement.

The final checks on the validity of the model involve the initial conditions, and the degree of truncation error introduced by the spatial and temporal finite differencing. The initial conditions used throughout the research allow no vertical structure of the horizontal wind. Geostrophy then requires that the initial temperature perturbation be zero. In order to determine whether or not these initial conditions prevent the development of large temperature perturbations, a test was made in which v' was distributed according to a gaussian in the vertical, as well as in the horizontal. The field of T' required by geostrophy

Figure 4.9. Growth rate vs. wavelength for waves excited in a linear vertical shear profile.

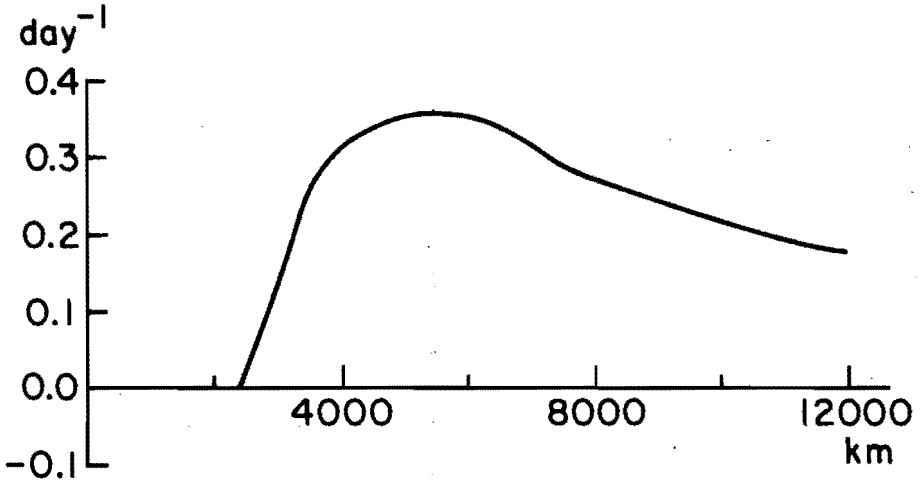
day^{-1}
0.4
0.3
0.2
0.1
0.0
-0.1
4000
8000
12000
km

then had a maximum amplitude of about 0.02C. The model results remained virtually unchanged by this variation of the initial conditions. If $\Delta y, \Delta p$, or Δt is too large, errors in both the amplitude and phase of the waves can be generated by truncation error. To test this, Δy, Δp, and Δt were each halved (independently) and the model re-run. Again, the results were unchanged, indicating that the horizontal, vertical and temporal resolution of the model are sufficient to represent the solution properly.

V. LINEAR MODEL RESULTS

1. Introduction

The model is applied to the African wave problem in three stages. First, $\frac{\partial[\bar{u}]}{\partial p}$ is constrained to be zero, and since the initial perturbation has no vertical structure, the system reduces to a barotropic system. Then, $[\bar{u}]$ is allowed to have both horizontal and vertical shear, and the generalized baroclinic system is studied. Finally, the thermodynamic equation is altered to include the effect of latent heat release on the dynamics of the wave.

The barotropic model allows only one mechanism by which the waves can grow, the conversion of ZKE to EKE by the horizontal Reynolds stresses. Since the mean zonal wind field at 700 mb has been shown to satisfy the condition for barotropic instability, it has been suggested that this instability may be the principal mechanism by which the waves are generated. The barotropic model can then provide a simple conceptual background against which the results of subsequent, more complex, models may be viewed.

The dry primitive equation model allows the atmosphere to have a vertical structure and permits ZAPE as well as ZKE to be a source of disturbance energy. The only constraints placed on the motions are that they be adiabatic and hydrostatic. The model is run with the assumption that the modification of the static stability due to the deviations of the temperature from its average value on a constant pressure surface is negligible. The consequences of relaxing this assumption are also investigated. The results of the primitive equation model reveal the importance of non-barotropic processes, and their effect on the barotropic processes in the generation of African waves.

Diabatic heating due to latent heat release is allowed by the moist model. Otherwise, it is identical to the dry primitive equation model. The crude parameterization scheme described in Chapter 4 is used, which can only be expected to provide an order of magnitude estimate of the effect of latent heating.

2. Barotropic Model

The wind field displayed in Figure 4.2 is representative of the observed state of the atmosphere. However, it is not appropriate for use in a barotropic system. It must be approximated by a mean flow which depends on latitude only. Such a zonal flow is shown in Figure 5.1. Here, the observed flow at 700 mb is assumed to exist throughout the depth of the atmosphere. Comparison with Figure 4.2 shows that this assumption leads to significant distortion of $[\bar{u}]$ both above and below the 700 mb level. The 700 mb level was chosen to define the barotropic flow, because the disturbances first appear at this level, and attain their maximum intensity there. If the barotropic instability is an important mechanism for the growth of the waves, it follows that the mean flow at 700 mb must support such an instability.

After the mean state has been perturbed, the disturbance propagates, and is allowed to grow or decay, depending on the stability of the particular modes which have been excited. Only those modes which have a positive growth rate can become finite amplitude disturbances. If several unstable modes are excited, the one with the largest growth rate will dominate after a sufficiently long time.

Figure 5.1. $[\bar{u}]$ used in barotropic model. Contour interval = 6.0 m sec^{-1}.

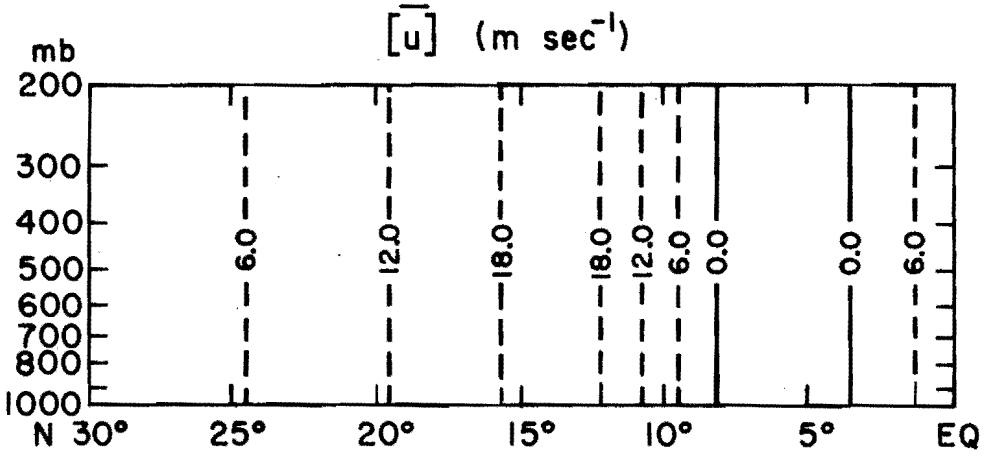
[ū] (m sec⁻¹)
mb
200
300
400
500
600
700
800
1000
6.0
12.0
18.0
18.0
12.0
6.0
0.0
0.0
6.0
N 30°
25°
20°
15°
10°
5°
EQ

It may be assumed that in nature all possible modes are excited by infinitesimal perturbations. The disturbances which are observed represent the most unstable of these. In order that the most unstable mode may be identified by the model, the mean state must be perturbed by disturbances of several different wavelengths. Each perturbation has a gaussian dependence on latitude, in order to excite a large number of the possible modes of motion. As the disturbance develops, the most unstable mode becomes dominant. When this happens the motion approaches its asymptotic limit.

The intensity of the mean flow is varied by changing the value of the adjustable parameter, U. The choice of U is based on the observed intensity of the flow. According to Burpee (1972) the eight year average value of U for the months of July and August is somewhat less than 15 m sec^{-1}. As noted previously, the position and intensity of the jet vary with time and space, so that the actual value of U is often considerably greater than its average value. The two values of U used in the barotropic model are U = 17 m sec^{-1} representing a flow of moderate strength, and U = 22.6 m sec^{-1}, representing a relatively intense flow. Disturbances are introduced into each of these flows. The asymptotic values of the growth rates of the waves are shown in Figure 5.2 for each value of U. The periods of the waves are also shown.

As predicted by barotropic theory, the growth rates increase and the periods decrease as the intensity of the jet is increased. In each case, the most unstable disturbance has a wavelength between 3000 km and 3600 km. The wavelength of maximum instability is slightly shorter for the weaker jet. In that case the growth of the most unstable wave is

Figure 5.2. Growth rate and period vs. wavelength in the barotropic model.

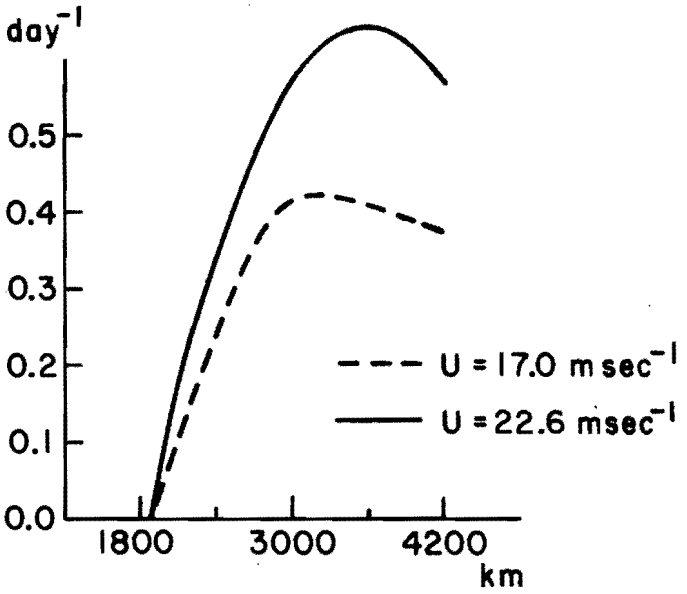
day^{-1}
0.5
0.4
0.3
0.2
0.1
0.0
1800
3000
4200
km
U = 17.0 m sec^{-1}
U = 22.6 msec^{-1}

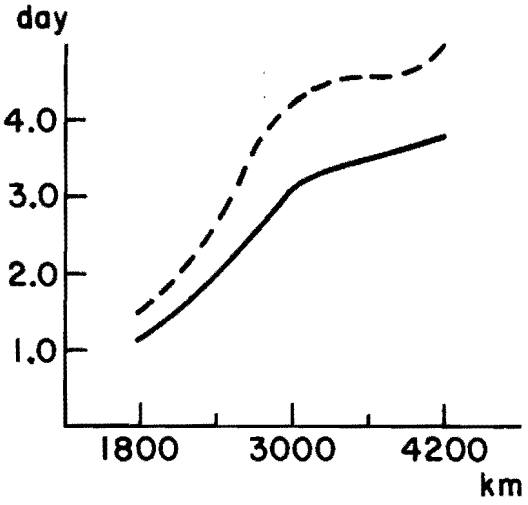
day
4.0
3.0
2.0
1.0
1800
3000
4200
km

.43 day^{-1} and its period is 4.5 days. This corresponds roughly with the the characteristic wavelength and period computed by Burpee (1972) from spectral data. For the stronger jet, the maximum growth rate is .64 day^{-1} with a period of about 3.5 days. The 3.5 day period agrees with composite (Burpee, 1974) and synoptic (Carlson, 1969; 1971) observations.

Except for the 1800 km wave, which decays, all the waves supported by the 22.6 m sec^{-1} jet display many of the same characteristics. The magnitudes of the wind perturbations are on the order of 1 m sec^{-1}. The disturbances grow by converting ZKE to EKE through the barotropic conversion process. For all wavelengths, the effect is largest near 10°N. Although the exact shape of the disturbance depends on the wavelength, the meridional wind always reaches a maximum value near 7°N, and the zonal wind displays a maximum of slightly greater magnitude near 10°N.

One feature of the waves which exhibits a qualitative dependence on wavelength is the tilt of the trough axis. Burpee (1975) reported that the axis of the observed waves tilts from southwest to northeast from the equator to 20°N, with the most pronounced tilt to the south of the jet maximum. Figure 5.3 shows the position of the trough axis for the five different wavelengths in the case of the strong jet.

The physical significance of the tilt of the trough axis may be seen from Figure 5.4 which shows a schematic view of an unstable disturbance to the south of an easterly jet. The meridional perturbation is sinusoidal in x, and the axis of the disturbance slopes from southwest to northeast. The direction of zonal momentum transport may be seen by considering the flow near the point A. Due to the tilt of the disturbance, $\frac{\partial v'}{\partial y} \neq 0$, even though the amplitude of the wave is independent of latitude. At the point

Figure 5.3. Tilt of the trough axis for five different wavelengths.

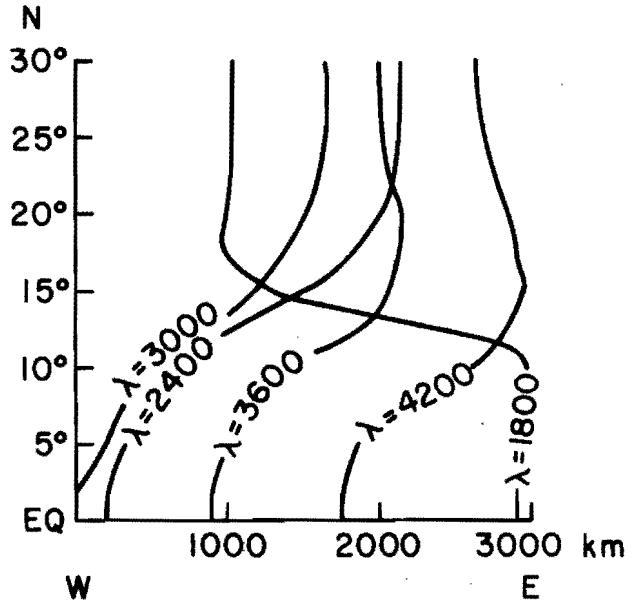
N
30°
25°
20°
15°
10°
5°
EQ
W
E
1000
2000
3000 km
λ=3000
λ=2400
λ=3600
λ=4200
λ=1800

Figure 5.4. Schematic representation of v', showing the physical significance of the tilt of the trough axis in terms of momentum transport.

At B, $\frac{\partial v'}{\partial y} > 0$

at A, $\frac{\partial v'}{\partial y} = 0 \quad \Rightarrow \quad$ at A, $\frac{\partial^2 v'}{\partial x \partial y} < 0 \Rightarrow \frac{\partial^2 u'}{\partial x^2} > 0 \Rightarrow u' < 0$

at C $\frac{\partial v'}{\partial y} < 0$ $\quad \therefore$ negative u' is transported southward.

At D, $\frac{\partial v'}{\partial y} < 0$

at E, $\frac{\partial v'}{\partial y} = 0 \quad \Rightarrow \quad$ at E, $\frac{\partial^2 v'}{\partial x \partial y} > 0 \Rightarrow \frac{\partial^2 u'}{\partial x^2} < 0 \Rightarrow u' > 0$

at F, $\frac{\partial v'}{\partial y}$ 0 $\quad \therefore$ positive u' is transported northward.

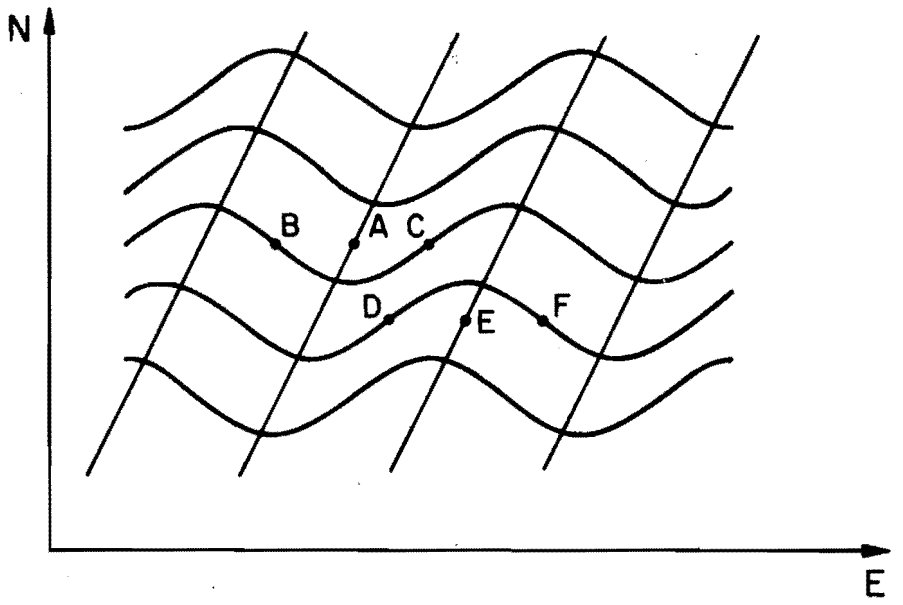
N
B
A
C
D
E
F
E

marked A on the figure, the value of $\frac{\partial v'}{\partial y}$ decreases from west to east, so that $\frac{\partial^2 v'}{\partial x \partial y} < 0$. Then the continuity equation (in the absence of vertical structure) requires that $\frac{\partial^2 u'}{\partial x^2} > 0$. This implies that the zonal perturbation at A must be negative. Then, since v' is negative at A, the disturbance transports easterly momentum southward, away from the maximum of easterly momentum at the jet. Similar arguments may be applied at point B to show that westerly momentum is transported toward the jet. Thus, the tilt of the trough axis determines the direction of transport of zonal momentum by the waves.

For the stable wave (λ = 1800 km) the axis slopes sharply southeast-northwest between 10°N and 17°N. Elsewhere, the slope is southwest-northeast, but the magnitude of the slope is very small. This is to be expected. It reflects the fact that the horizontal Reynolds stress transports easterly momentum toward the jet, as must be the case for a stable wave. For $\lambda \geq$ 2400 km, the disturbances become unstable, and the picture changes. To the south of the jet maximum, disturbances of all wavelengths display a southwest-northeast tilt, the magnitude of which is greatest between 8°N and 12°N. Since this is the region of maximum mean zonal wind shear, it is also the region of maximum conversion from ZKE to EKE. North of the jet maximum the slope of the wave axis depends on the wavelength of the perturbation, even among the unstable waves. For λ = 2400 km and λ = 3000 km, the trough axis continues to slope southwest-northeast. But, because the meridional gradient of the mean zonal current changes sign at this point, the sense of the energy conversion is reversed. That is, north of the jet axis, easterly momentum is transported toward the jet, so that energy is converted from EKE to ZKE. This is particularly true from

13°N to 23°N. Beyond 23°N the orientation of the wave axis is essentially north-south, and very little energy is transferred between the jet and the disturbance. When $\lambda \geq 3600$ km, the tilt of the wave axis reverses near the center of the jet and becomes southeast-northwest north of about 13°N. This behavior ensures that easterly momentum is transported away from the jet throughout the domain (although the magnitude of the transport is much smaller to the north of the jet than to the south) and the Reynolds stress acts to convert ZKE to EKE everywhere.

Although the 3600 km wave has a slightly larger growth rate, the 3000 km wave is selected for detailed analysis because it displays the kind of tilt suggested by the data. Its growth rate is not much smaller than that of the 3600 km wave, and its period falls within the range of observed periods.

Figure 5.5 shows the perturbation wind field after 4.6 days. The center of cyclonic circulation is found at about 7°N. The maximum meridional wind perturbation is found at this latitude as well. The maximum zonal perturbation lies a few degrees to the north. The position of the trough axis is also marked on the figure. The overall tilt of the trough axis is southwest-northeast. The tilt is a maximum near 10°N and approaches zero north of 20°N. The wave at 5°N leads that at 30°N by about a quarter wavelength. The data coverage in the northern part of the region is quite sparse, so that estimates of the tilt of the wave axis north of 15°N are rather crude, but Burpee (1975) reported a tilt of the trough axis similar to that generated by the model. Since the magnitude of the barotropic energy conversion is proportional to the slope of the wave axis, it follows that the largest perturbation should be in the region of maximum tilt.

Figure 5.5. Perturbation wind field after 4.6 days. Position of the trough axis is indicated by the dashed line.

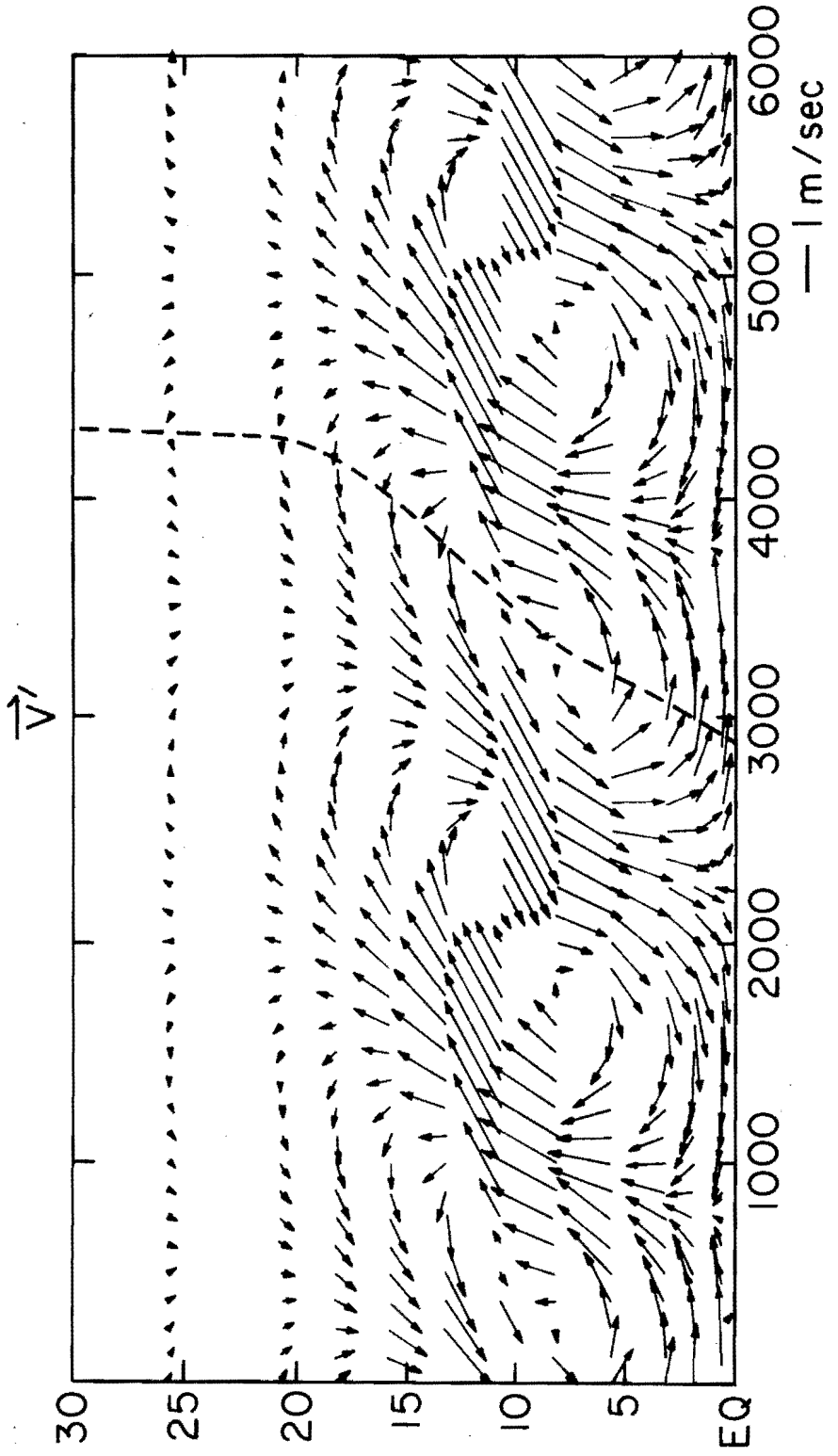
$\overrightarrow{V'}$
30
25
20
15
10
5
EQ
1000
2000
3000
4000
5000
6000
— 1 m/sec

The energetics of the barotropic wave are fairly simple. The source of kinetic energy is the kinetic energy of the mean flow, ZKE. The only mechanism by which ZKE may be converted to EKE in a barotropic system is the transport of zonal momentum away from the jet by the horizontal Reynolds stress. The perturbation pressure field adjusts to the changing velocity disturbance and redistributes EKE. Thus, the local change in perturbation kinetic energy is given by

$$\frac{\partial EKE}{\partial t} = CE_1 + CE_5 \tag{1}$$

where CE_1 and CE_5 are defined by equations (4.17) and (4.21). All other energy conversion terms are identically zero in the barotropic system. Only CE_1 represents a net production of EKE, since CE_5 must vanish when integrated over the entire model atmosphere.

Figure 5.6 shows the distribution of CE_1 and CE_5 with respect to latitude. The solid line represents the sum of the two terms. CE_1 is large and positive in a 3° latitude band centered near 10°N. Elsewhere, CE_1 has both positive and negative values, but is smaller in magnitude. In the latitude band in which CE_1 is large, CE_5 is of somewhat smaller magnitude, and negative. CE_5 is positive south of 8°N and north of 12°N. Thus, kinetic energy is created via the barotropic conversion process and is dispersed throughout the region between the equator and 16°N by the perturbation pressure field. The net increase of kinetic energy is nowhere negative, and is greater than .01 watts m^{-2} at all points south of 13°N, which is the approximate center of the jet. South of the jet axis, the disturbance grows steadily; north of the jet axis, the wave maintains constant intensity, or grows slowly.

Figure 5.6. Energy conversions (watts m^{-2}) as a function of latitude.

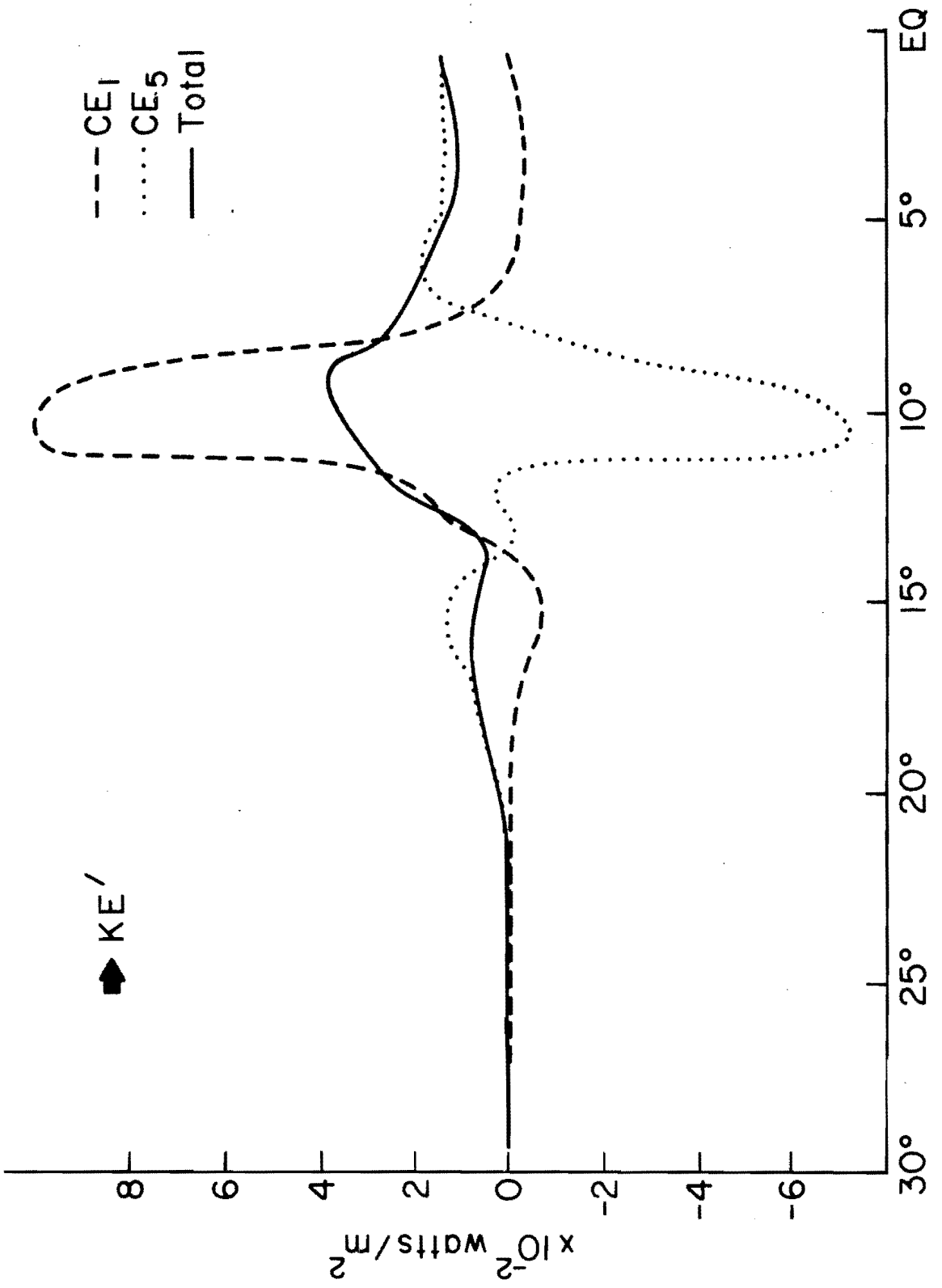
CE1
CE5
Total
KE'
EQ
5°
10°
15°
20°
25°
30°
8
6
4
2
0
-2
-4
-6
x 10⁻² watts/m²

Up to this point, the results have been generated by a pure barotropic model. Not only has the coupling between different levels of the atmosphere been ignored, but the existence of different flow fields at different levels has been ignored as well. As may be seen from Figure 4.2, the horizontal shear of the mean zonal wind changes with height. If the 500 mb field of $[\bar{u}]$ were used to define a barotropic atmosphere, it would display different stability characteristics than does the barotropic atmosphere defined by $[\bar{u}]$ at 700 mb. Consequently, the growth rates obtained with the barotropic model could not be expected to correspond to those of the actual disturbances in the atmosphere, even if the only means by which EKE could be generated were the barotropic process. In fact, the flow at other levels is more stable than that at 700 mb. Disturbances must grow more slowly, if they grow at all, in the more stable layers of the atmosphere. Thus the growth rate given by the barotropic model must over estimate the growth of the waves, since is is based on the instability at 700 mb, the most unstable level. In order to allow the barotropic response of the atmosphere to vary with height without allowing any vertical coupling, $[\bar{u}]$ at each of 900, 700, 500, and 300 mb is used to determine the mean jet in a barotropic system. Each jet is modeled independently, and the results are composited at the end of the integration. Subsequent references to the barotropic results will refer to these composited results.

The growth rates are obtained by averaging over the four levels of the model, and are shown in Figure 5.7. They are somewhat smaller than the 700 mb growth rates, but the two curves are qualitatively quite smaller. This indicates that most of the perturbation energy is found in the 700 mb

Figure 5.7. Growth rate vs. wavelength. Growth rates are obtained by compositing the results of four different barotropic models.

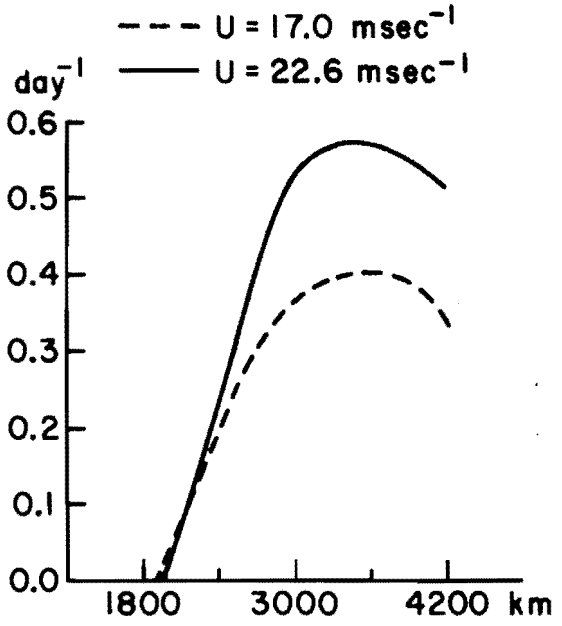
U = 17.0 msec⁻¹
U = 22.6 msec⁻¹
day⁻¹
0.6
0.5
0.4
0.3
0.2
0.1
0.0
1800
3000
4200 km

disturbance. The energy of the perturbation at other levels is not very significant.

Further analysis of the 3000 km wave in the strong jet gives more insight into the structure of the disturbance supported by the mean jet when the levels are not allowed to interact. Figure 5.8 shows the growth rate and energy density at different pressure levels. From this figure it is quite clear that the disturbance energy is concentrated at 700 mb. Thus, the total growth rate is very nearly equal to that determined using the 700 mb results alone. This is to be expected, in view of the distribution of $\frac{\partial^2[\bar{u}]}{\partial y^2}$ shown in Figure 4.2. Clearly, the large region in which $\frac{\partial^2[\bar{u}]}{\partial y^2}$ assumes large positive values at 700 mb contributes to the instability at this level. The amplitudes of u' and v' and the rate of energy generation CE_1 are shown in Figure 5.9. The disturbance is greatest at 700 mb and around 7°-10°N. The amplitude of the disturbance falls off rapidly above and below this level. The maximum amplitude of v' at 700 mb is 1.4 m sec^{-1}. It falls to .4 m sec^{-1} at both 900 mb and 500 mb. The maximum zonal perturbation of 1.8 m sec^{-1} occurs at 10°N at 700 mb and likewise falls below .4 m sec^{-1} at 900 mb and at 500 mb. This behavior is consistent with the distribution of CE_1 which is significantly positive only between 7°N and 12°N and between 850 mb and 500 mb.

These results lead to the conclusion that certain aspects of African waves are well simulated by the barotropic model. Allowing only for barotropic processes, the most unstable disturbances have a wavelength in the range 3000 km to 3600 km. The period of these disturbances is between 3 and 4 days. Their growth rates are sufficiently large to allow waves to develop in three days or less. These are all characteristics of the

Figure 5.8. Growth rate and energy density at different levels after 4.6 days

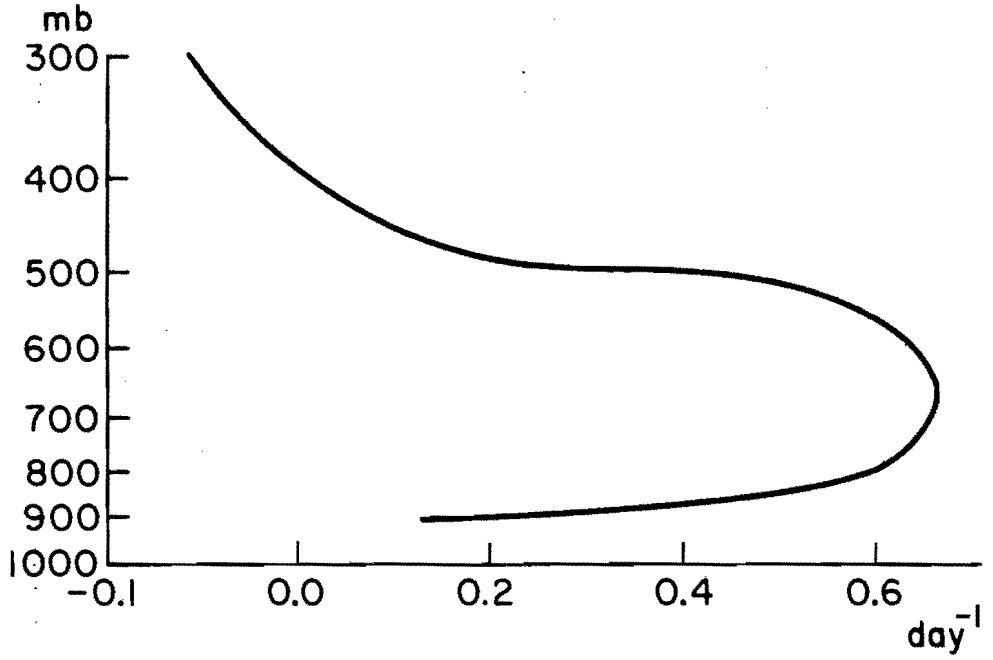
mb
300
400
500
600
700
800
900
1000
-0.1
0.0
0.2
0.4
0.6
day⁻¹

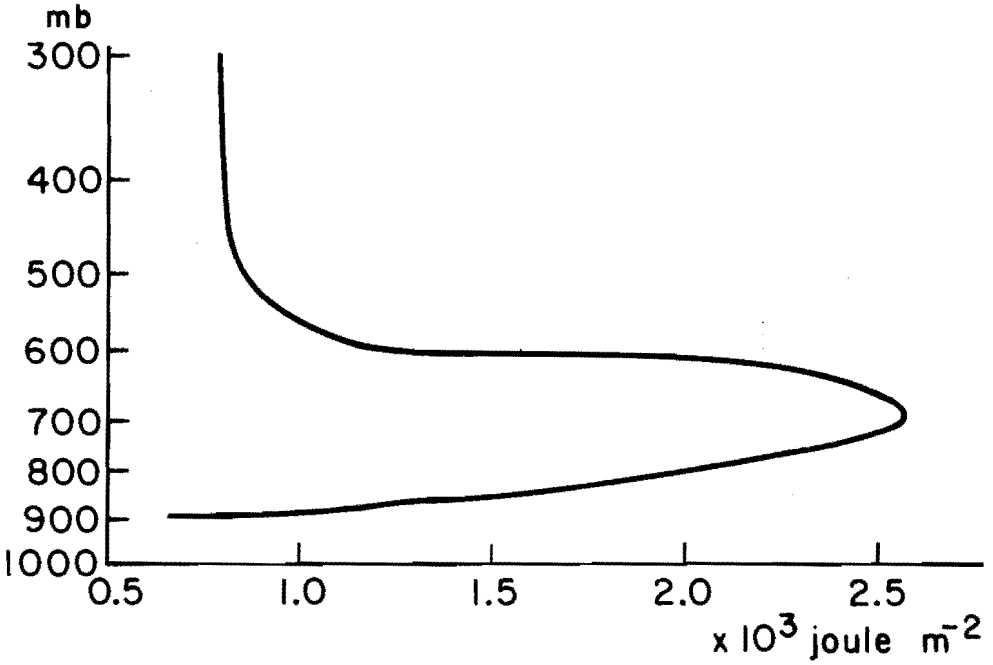
mb
300
400
500
600
700
800
900
1000
0.5
1.0
1.5
2.0
2.5
x 10³ joule m⁻²

Figure 5.9. Amplitude of u' and v' and CE, after 4.6 days. u' contour interval = .3 m sec^{-1}. v' contour interval = .2 m sec^{-1}. CE, contour interval = .03 watts m^{-2}.

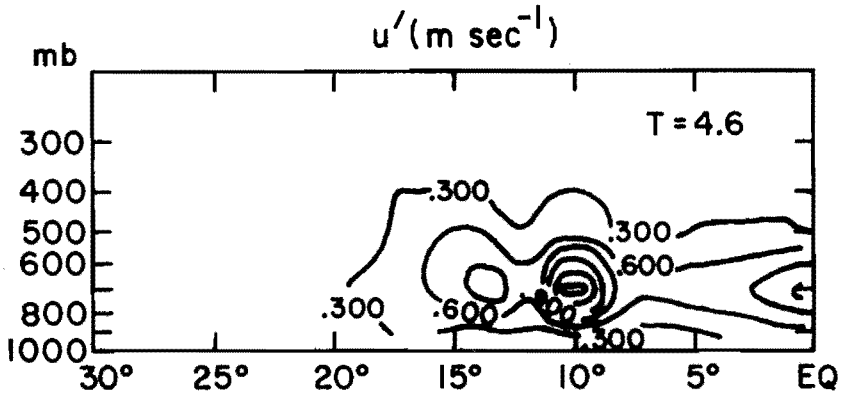
u′(m sec⁻¹)
mb
T = 4.6
300
400
500
600
800
1000
.300
.300
.300
.600
.600
.300
30°
25°
20°
15°
10°
5°
EQ

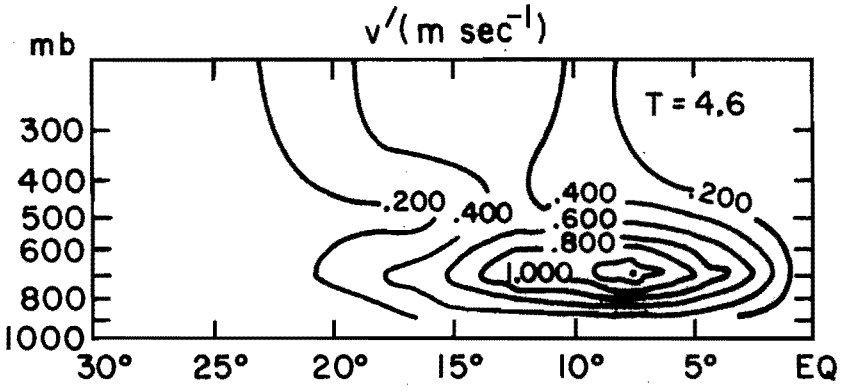
v′(m sec⁻¹)
mb
T = 4.6
300
400
500
600
800
1000
.200
.400
.400
.600
.800
1.000
.200
30°
25°
20°
15°
10°
5°
EQ

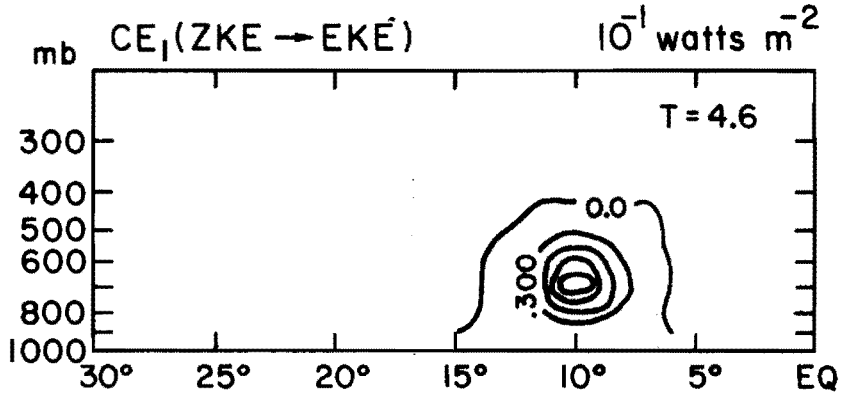
CE₁(ZKE → EKE′)
10⁻¹ watts m⁻²
mb
T = 4.6
300
400
500
600
800
1000
0.0
.300
30°
25°
20°
15°
10°
5°
EQ

observed waves. Furthermore, it is the 700 mb flow which becomes unstable in the atmosphere as well as in the barotropic model. The structure of the 3000 km wave at 700 mb is also quite similar to that of the observed waves. The largest disturbance is found near 10°N, where the zonal and meridional perturbations are of about equal magnitude. The trough axis slopes from southwest to northeast throughout the wave region.

The barotropic model can provide very little further information about the waves. Additional features of the waves, such as the temperature field, the vertical velocity field, and the vertical tilt of the wave axis cannot be investigated using a barotropic model. Furthermore, features which depend on these quantities, such as horizontal and vertical heat transport, vertical momentum transport, the roles of convection and of static stability, all of which may be estimated from the available data, are not treated by the barotropic model. In summary, the barotropic model does a rather good job of simulating the gross characteristics of African waves at 700 mb, but cannot represent many of the finer aspects of the waves.

3. Dry Primitive Equation Model

In order to simulate African waves more closely, the assumption of barotropy must be dropped and a general baroclinic mean state assumed. The primitive equations permit all types of atmospheric motions which are of meteorological importance. Different levels of the atmosphere are free to interact with each other. The horizontal divergence of the perturbation wind field is not constrained to be zero, so there is a non-vanishing vertical wind. Because the mean zonal wind $[\bar{u}]$ exhibits a vertical shear, thermal wind arguments require that the meridional gradient

of the mean zonal temperature, $\frac{\partial[\bar{T}]}{\partial y}$, be nonzero. Easterly momentum may be transported vertically, as well as horizontally, and heat is transported both vertically and horizontally. For the first applications of the model, the thermodynamic equation in the form of (3.19) is used; the contribution due to the term $\frac{\partial[\bar{T}]^*}{\partial p} - \frac{\kappa[T]^*}{p}$ is neglected.

The stability of the mean flow represented in Figure 4.2 is investigated with the primitive equation model. Figure 5.10 shows the growth rates and periods of the waves generated in this flow as functions of jet intensity and of wavelength. When U = 17.0 m sec^{-1} the maximum growth rate attained by any disturbance is .22 day^{-1}, by the 3000 km wave. This is quite a bit smaller than the growth rate of the corresponding wave in the barotropic model. Indeed, it is too small to really be considered an unstable wave. However, when U is increased to 22.6 m sec^{-1}, wavelengths between 2400 km and 4200 km become significantly unstable. The growth rates of the waves supported by this jet increase rather quickly as the wavelength is increased from 1800 km to 3000 km. For wavelengths greater than 3000 km, the growth rate falls off gradually from its maximum value of .37 day^{-1}. The slope of the curve for small wavelengths is great enough so that waves shorter than 3000 km are not likely to exist. But waves somewhat longer than 3000 km may be allowed, because the growth rate falls off slowly in this region. When U is increased further, to 28.3 m sec^{-1}, the waves become unstable for all wavelengths tested. The maximum growth rate is .54 day^{-1} for a wavelength of 3600 km. The peak is fairly well defined, so that wavelengths between 3000 km and 4000 km may be expected to be dominant.

Comparison of Figures 5.7 and 5.10 reveals the effects of non-barotropic interactions on the growth rate of the waves. For wavelength less than about 2600 km, the growth rates generated by the primitive equation model are greater than those of the barotropic model. When $\lambda > 2600$ km, the barotropic model produces the larger growth rates. The interactions between the vertical levels of the atmosphere tend to destabilize short wavelength perturbations ($\lambda < 2600$ km) and to stabilize longer wavelengths ($\lambda > 2600$ km).

For a given value of U, the period of the waves is a linear function of wavelength (i.e. the phase speed is essentially independent of wavelength). The period is always smaller in the primitive equation model than in the barotropic model. The maximum difference between the periods computed for the same wavelength by the two models is one day, for the 3000 km wave.

The waves which are most likely to correspond to African waves are those supported by the 22.6 m sec^{-1} jet. The waves generated by the 17.0 m sec^{-1} jet are rejected because of their small growth rates. As discussed previously, 17.0 m sec^{-1} is probably a relatively small value for U even though the eight year average value is only 12.2 m sec^{-1}. U = 22.6 m sec^{-1} is more representative of the observed flow at any given time. However, the flow rarely attains an intensity of 28.3 m sec^{-1}, and it is quite unlikely that such a jet is ever sustained for several days at a time. Therefore, further detailed analysis of the model results will concentrate on the waves supported by the 22.6 m sec^{-1} jet.

As seen from Figure 5.10, the most unstable waves supported by the 22.6 m sec^{-1} jet have wavelengths from 3000 to 4000 km. Of these, the

Figure 5.10. Growth rate and period vs. wavelength for 3 different values of U.

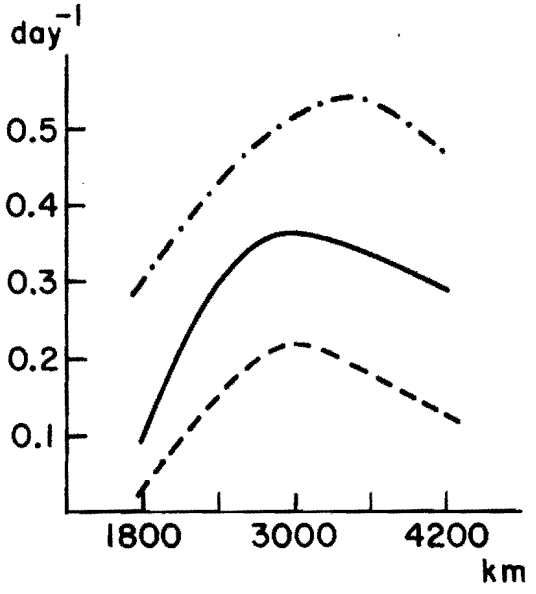
day⁻¹
0.5
0.4
0.3
0.2
0.1
1800
3000
4200
km

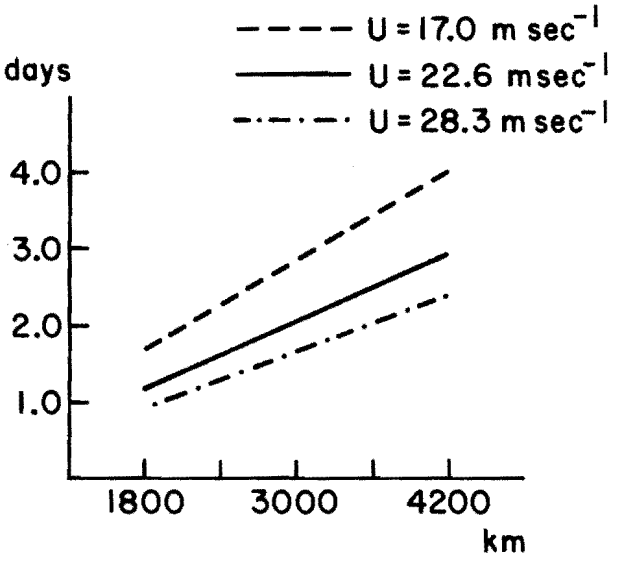
U = 17.0 m sec⁻¹
U = 22.6 m sec⁻¹
U = 28.3 m sec⁻¹
days
4.0
3.0
2.0
1.0
1800
3000
4200
km

3000 km wave is chosen for detailed analysis. This wavelength is within the bounds of observations of the real waves. The period of the wave is 2.2 ± .2 days. This is somewhat shorter than that of the observed waves, but falls within a reasonable uncertainty of the observations.

Figure 5.11 shows the growth rates of kinetic energy (EKE), available potential energy (EAPE), and total energy (ETE) as functions of time for the wave under consideration. The growth rate for EAPE is quite large at small times because the initial value of EAPE is zero. Even at large times, the growth rate fluctuates considerably. These fluctuations are due to the fact that EAPE is still small compared to EKE. Therefore, small changes in $\frac{\partial EAPE}{\partial t}$ result in relatively large changes in the growth rate. The growth rates of EKE and ETE vary smoothly from zero to their asymptotic value of .36 day^{-1}. At all times, the growth rate of ETE is approximately equal to that of EKE. This is an indication of the fact that the kinetic energy of the perturbation is much greater than is the available potential energy. Indeed, the value of EKE after 4.6 days of integration is about 420 joules m^{-2}, whereas the value of EAPE at the same time is only 42 joules m^{-2}. Therefore, the total energy must grow at approximately the same rate as does the kinetic energy. This supports the hypothesis that the primary source of disturbance energy is the kinetic energy of the mean zonal flow, rather than the potential energy of the mean zonal flow.

The structure of the perturbation after 4.6 days is shown in height-latitude cross section in Figure 5.12. The initial perturbation (not shown) is independent of height. Its latitudinal dependence is given by a gaussian centered at 15°N with a maximum magnitude of .29 m sec^{-1}. After 4.6 days, both the latitudinal symmetry and the height independence of the

Figure 5.11. Growth rate of EKE, EAPE, and ETE vs. time for $u = 22.6$ m sec^{-1}, $\lambda = 3000$ km.

Growth Rate vs Time

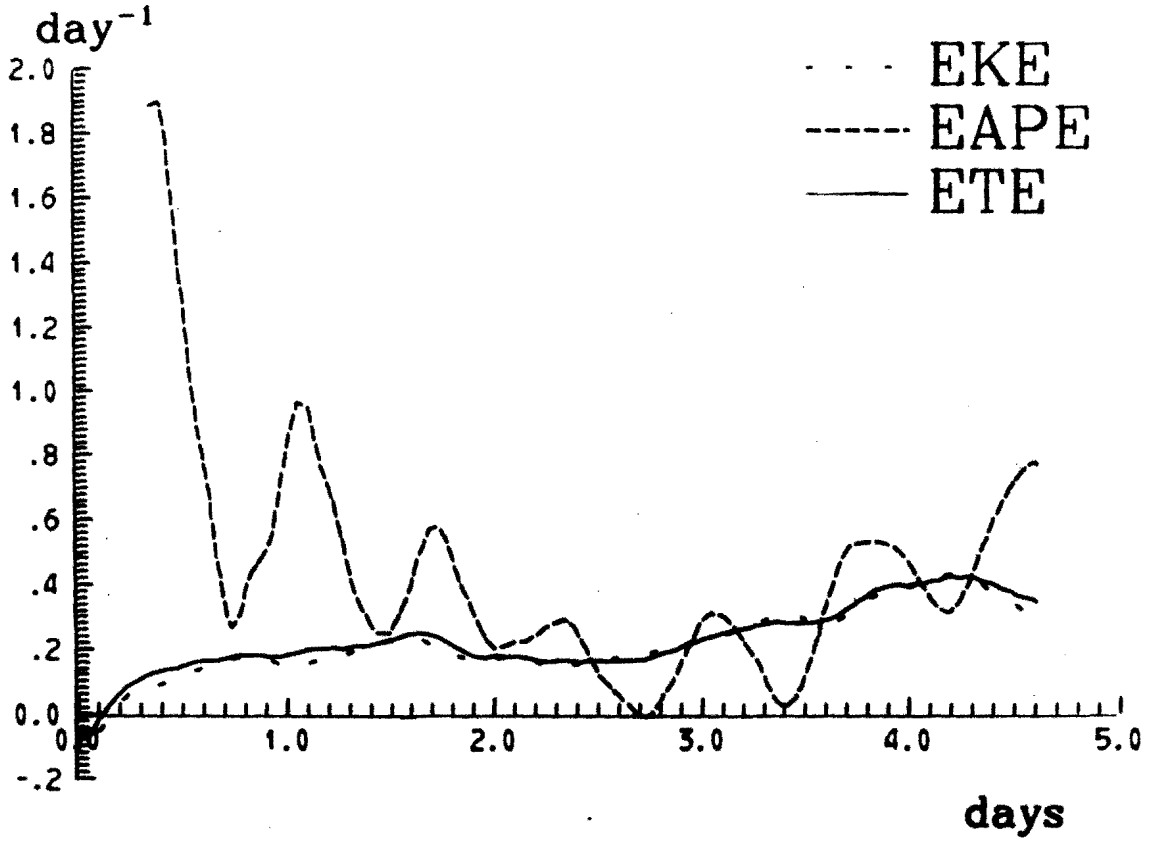

Figure 5.12. Cross sections of the wind perturbations after 4.6 days for $U = 22.6$ m sec^{-1}, $\lambda = 3000$ km. u' contour interval = .5 m sec^{-1}, v' contour interval = .2 m sec^{-1}, ω' contour interval = $.5 \times 10^{-4}$ mb sec^{-1}.

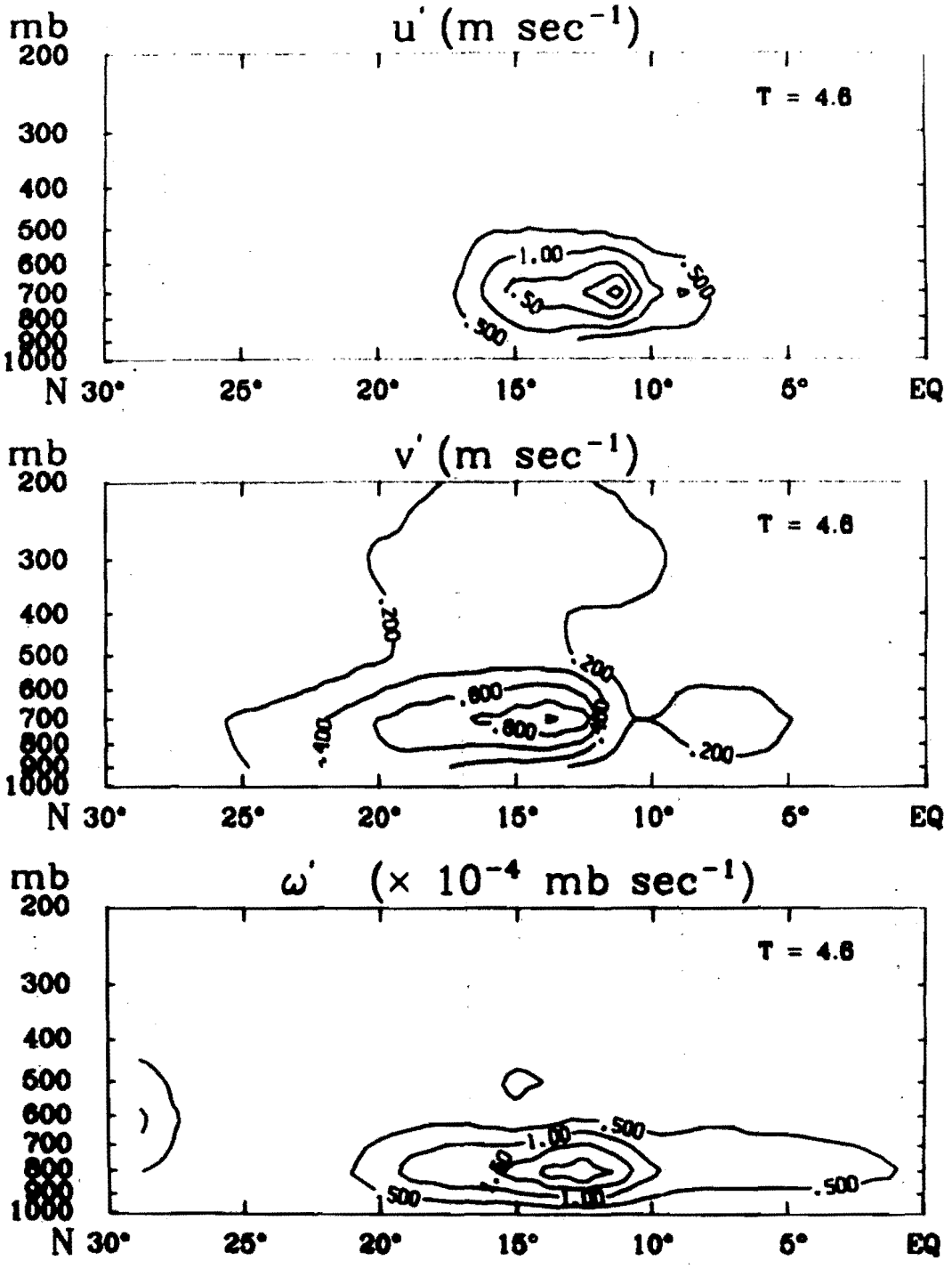
mb
u' (m sec⁻¹)
T = 4.6
200
300
400
500
600
700
800
900
1000
1.00
.50
.500
N 30° 25° 20° 15° 10° 5° EQ
mb
v' (m sec⁻¹)
T = 4.6
.200
.600
.800
.400
N 30° 25° 20° 15° 10° 5° EQ
mb
ω' (× 10⁻⁴ mb sec⁻¹)
T = 4.6
1.00
.500
N 30° 25° 20° 15° 10° 5° EQ

initial disturbance have been destroyed. The maximum perturbation is at 700 mb, at 14°N. Its magnitude is about 1 m sec^{-1}. At 500 mb and at 300 mb, the maximum perturbations are still located at 15°N and their magnitudes are only slightly greater than their initial magnitudes. At 900 mb, however, the wave exhibits more activity. At this level the largest perturbation is .5 m sec^{-1} and is located at 20°N. It is significant to note that, as observed by Burpee (1974), the maximum disturbance near the surface is found somewhat to the north of the 700 mb maximum.

The amplitude of the zonal perturbation after 4.6 days is also shown in Figure 5.12. The maximum amplitude of the perturbation is about 2.5 m sec^{-1} and is found at 11°N at 700 mb. This is about 300 km to the south of the maximum meridional perturbation. The maximum amplitude at 900 mb is .6 m sec^{-1} at 14°N. Thus, the latitudinal position of the maximum zonal perturbation varies much less with height than does that of the meridional perturbation. The central maximum of u' is about 2.5 times greater than the maximum value of v', and the isopleths of u' are far more concentrated than are those of v'. Despite the significant difference in their maximum amplitudes, about 600 km away from their maxima the two perturbations are of approximately equal magnitude. Between the equator and 8°N, and between 18°N and 30°N, the meridional perturbation is greater than the zonal perturbation.

The vertical velocity, ω', is calculated from the horizontal wind field using the equation of continuity. The largest values of ω' are found at 800 mb near 14°N. There, the amplitude of ω' is 2.5×10^{-4} mb sec^{-1}, which corresponds to $w' \simeq .25$ cm sec^{-1}. This is the same

latitude as that at which the meridional perturbation is large, but it is somewhat to the north of the maximum zonal perturbation. The vertical velocity falls off rapidly with height and above 500 mb it is everywhere less than $.2 \times 10^{-4}$ mb sec^{-1}, i.e. $w' < .04$ cm sec^{-1}.

These values for ω' may seem small. Carlson (1971) reported vertical velocities of up to 2 cm sec^{-1}. Reed and Recker (1971) reported similar vertical velocities associated with easterly waves in the Pacific. However, the large values of w' are measured at upper levels, near 300-400 mb. They are due to convective activity along the axis of well developed waves. A dry model representing the initiation of the waves should not be expected to reproduce these vertical velocities.

The temperature perturbation associated with the disturbance is quite small. Its amplitude is shown in Figure 5.13. It reaches a maximum value of .24 C near 13°N at 800 mb. As is the case for the vertical velocity, the temperature perturbation is largest at the lowest level at which it is computed. The small values for the temperature fluctuations are consistent with spectral and composite analysis of easterly wave data. Burpee (1972) reported that the variance of temperature is too small to be resolved by spectral techniques, and Reed and Recker (1971) reported temperature fluctuations on the order of .2 C.

The variation of geopotential height is fairly small also. (Figure 5.13) The maximum perturbation is 16.1 m^2 sec^{-2} at 13°N at 700 mb. This corresponds to a pressure perturbation of about .1 mb. The position of the maximum corresponds to the position of the largest meridional perturbation. There is a secondary maximum of 8.9 m^2 sec^{-2} at 900 mb. It is located at 20°N and coincides with the 900 mb wind maximum. Although the

Figure 5.13. Temperature and geopotential perturbations after 4.6 days for $U = 22.6$ m sec^{-1}, $\lambda = 3000$ km. T' contour interval = .04C, ϕ' contour interval = 3 $m^2 sec^{-2}$.

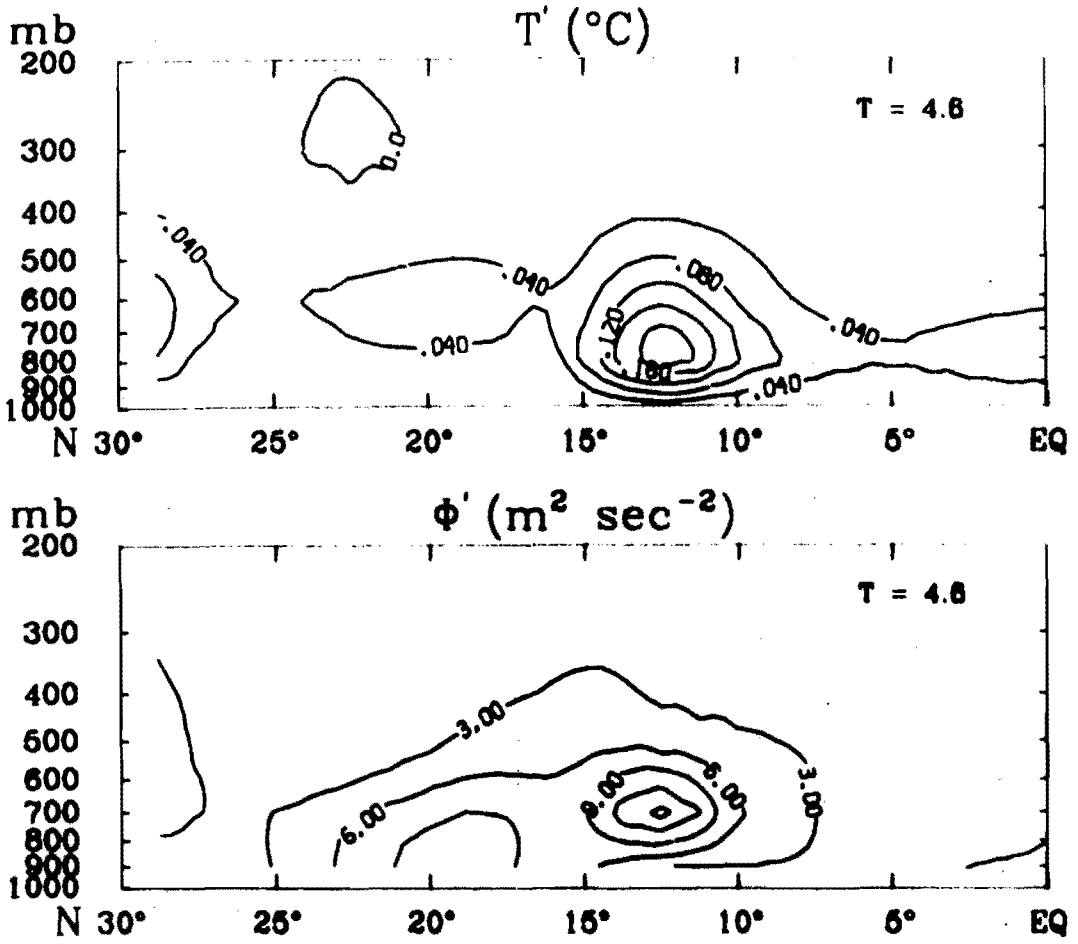
mb
T' (°C)
T = 4.8
200
300
400
500
600
700
800
900
1000
.040
.080
.120
0.0
N 30°
25°
20°
15°
10°
5°
EQ
mb
Φ' (m² sec⁻²)
T = 4.8
3.00
6.00
9.00
N 30°
25°
20°
15°
10°
5°
EQ

geopotential variation is significantly smaller at 900 mb than at 700 mb, because of the greater density at 900 mb, the corresponding pressure fluctuation is only slightly smaller than that at 700 mb.

The energetics of the wave generated by the primitive equations are more complicated than those of the barotropic wave. Both the kinetic energy and the available potential energy of the zonal flow represent energy sources for the disturbance. ZKE may be converted to EKE by horizontal transport of zonal momentum, as in a barotropic system, or by vertical transport of zonal momentum. No direct conversions between ZAPE and EKE are allowed, but the conversion may take place indirectly. ZAPE may be converted to EAPE by transport of heat down the horizontal temperature gradient. EAPE is converted to EKE by the sinking of cool air and rising of warm air. The perturbation pressure field adjusts to the changes in the flow field and redistributes EKE both vertically and horizontally.

The local energy balance for the disturbance may be written as follows:

$$\frac{\partial EKE}{\partial t} = CE_1 + CE_2 + CE_5 + CE_6 \tag{3}$$

$$\frac{\partial EAPE}{\partial t} = CE_3 + CE_4 \tag{4}$$

where the energy conversion terms are defined by equations (4.17) - (4.22).

Contours of CE_1, CE_2, CE_3, CE_4, and CE_5 are shown in Figures 5.14 and 5.15. Several points are immediately obvious upon inspection of these figures. First, the conversions are generally consistent with the wind

Figure 5.14. Energy conversions after 4.6 days for U = 22.6 m sec^{-1}, λ = 3000 km. CE_1 contour interval = .01 watts m^{-2}, CE_2 contour interval = 4 x 10^{-3} watts m^{-2}, CE_3 contour interval = 9 x 10^{-4} watts m^{-2}.

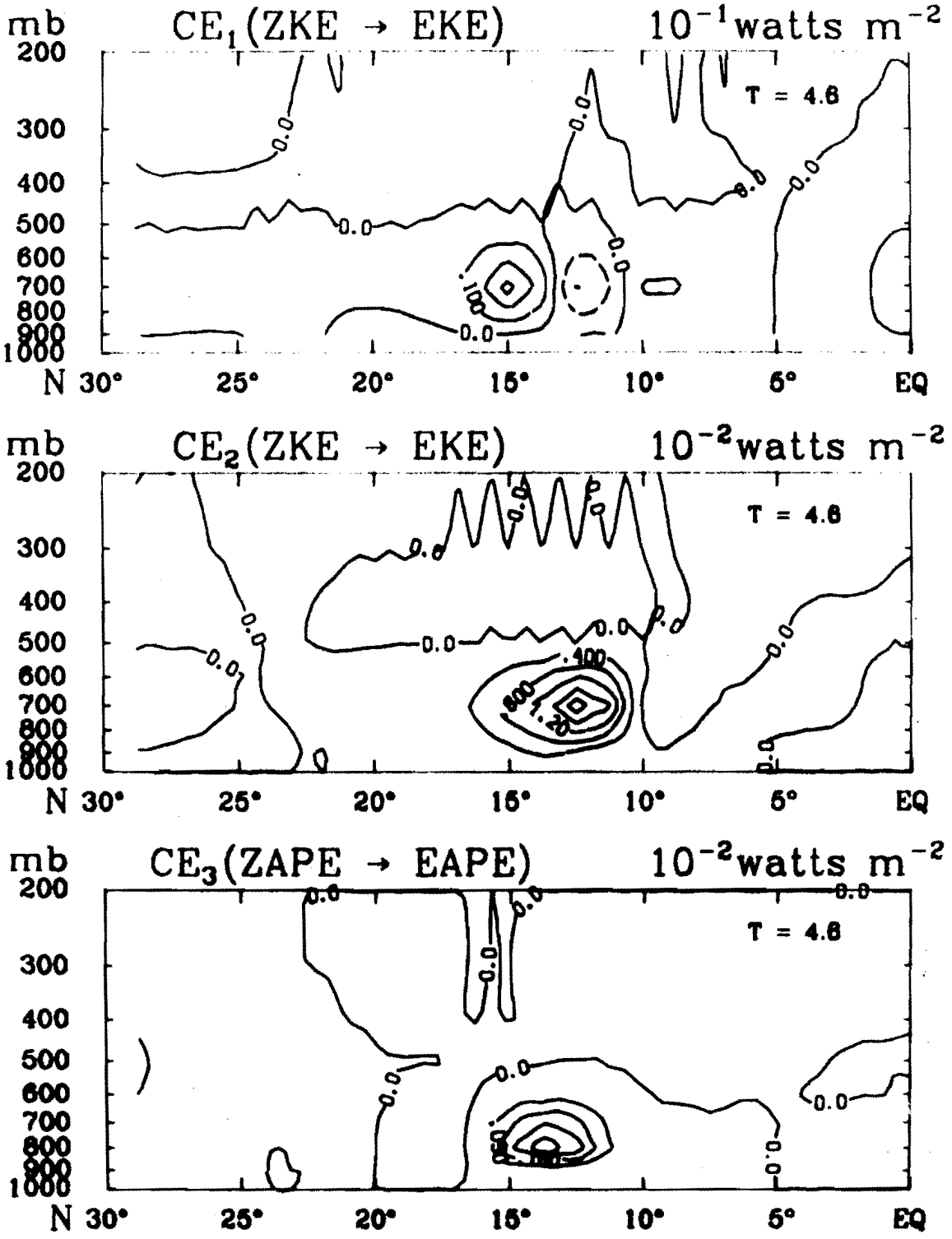
mb
CE_1(ZKE → EKE)
10^{-1}watts m^{-2}
T = 4.6
mb
CE_2(ZKE → EKE)
10^{-2}watts m^{-2}
T = 4.6
mb
CE_3(ZAPE → EAPE)
10^{-2}watts m^{-2}
T = 4.6
200
300
400
500
600
700
800
900
1000
N 30° 25° 20° 15° 10° 5° EQ

Figure 5.15. Energy conversions after 4.6 days for U = 22.6 m sec^{-1}, λ = 3000 km. CE_4 contour interval = 1 x 10^{-3} watts m^{-2}, CE_5 contour interval = .01 watts m^{-2}.

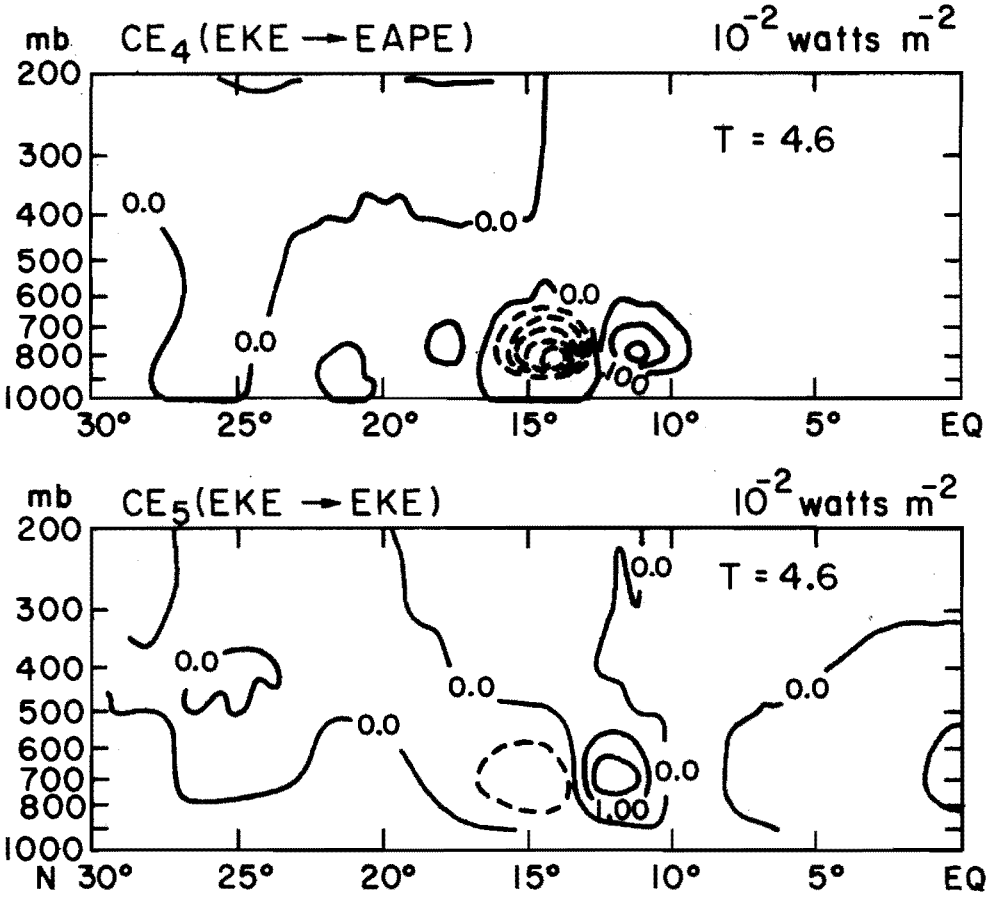
mb
CE4(EKE → EAPE)
10⁻² watts m⁻²
T = 4.6
200
300
400
500
600
700
800
1000
0.0
0.0
0.0
0.0
1.00
30°
25°
20°
15°
10°
5°
EQ
mb
CE5(EKE → EKE)
10⁻² watts m⁻²
T = 4.6
200
300
400
500
600
700
800
1000
0.0
0.0
0.0
0.0
0.0
0.0
1.00
N 30°
25°
20°
15°
10°
5°
EQ

and temperature fields. Since the perturbation kinetic energy per unit surface area is defined by $EKE = \frac{\frac{1}{2}\int dM(u'^2 + v'^2)}{\int ds}$, Figure 5.12 shows that most of the kinetic energy of the disturbance is confined to the lower atmosphere, below 500 mb. The maximum concentration of EKE is at 700 mb between 10°N and 15°N. The energy density decreases quite rapidly in all directions, particularly upward. Figures 5.14 and 5.15 show that the generation of EKE is largest in this same region. The available potential energy of the perturbation is given by $EAPE = \frac{-\frac{1}{2}\int dM \frac{R}{p\sigma} T'^2}{\int ds}$. According to Figure 5.13, T', and therefore EAPE, is a maximum at the lowest level and is negligible above 500 mb, so that EAPE is concentrated between the surface and 500 mb, and between 10°N and 15°N. Figures 5.14 and 5.15 show that CE_3 and CE_4 assume their largest values in the same region. Thus, both EKE and EAPE are large in the same regions in which they are generated.

It is important to notice that the conversion terms involving EAPE are smaller than those involving EKE by roughly an order of magnitude. CE_1 and CE_2 both reach maximum values in excess of 2.2×10^{-2} watts m^{-2}. CE_3 and CE_4, on the other hand, are always smaller than 5.7×10^{-3} watts m^{-2}. As a result, EAPE can never become a large fraction of the total energy of the disturbance.

Since the waves are most active between 800 mb and 650 mb, it is instructive to study the disturbance in more detail at this level. In order to represent the disturbance more clearly, and in particular to illustrate the phase relationships between the variables, the velocity

fields, the geopotential perturbation, and the temperature perturbation are plotted on a horizontal plane at the level of maximum intensity. These are shown in Figures 5.16 - 5.19. The horizontal wind and geopotential perturbations are plotted at 700 mb; the vertical velocity and temperature perturbations are at 800 mb. The latitudinal extent of each diagram is from the equator to 30°N. Two wavelengths of the disturbance are represented, a zonal extent of 6000 km.

The magnitude and direction of the horizontal wind disturbance are plotted in Figure 5.16. Distinct cyclone-anticyclone pairs are found at two latitudes. The southern disturbance is centered at about 5°N. This is basically a perturbation on the meridional wind field. The magnitude of the perturbation is less than .3 m sec^{-1}. The zonal perturbation is very weak. Although the circulation is not very strong, the disturbances exhibit a definite tilt from southwest to northeast. Farther to the north, extending from 12°N to 25°N, is another set of disturbances. These disturbances are much stronger than those at 5°N, and are nearly zonal. They are strongest at 12°N, where the wind perturbation approaches 2.5 m sec^{-1}. The meridional perturbation increases and the zonal perturbation decreases from 12°N to the center of the circulation at about 18°N. As shown in Figure 5.12, the maximum meridional perturbation of 1.0 m sec^{-1} is located at 14°N. At the center of the circulation the magnitude of the wind is as small as .5 m sec^{-1}. The trough axis, as defined by the meridional wind shift, tilts from southeast to northeast. North of 18°N the trough axis displays essentially no tilt at all.

Contours of the vertical velocity field at 800 mb are plotted in Figure 5.17. The strongest vertical motions are found near 13°N, in the

Figure 5.16. Horizontal wind perturbation shown on an x-y plane at 700 mb after 4.6 days. $U = 22.6$ m sec^{-1}, $\lambda =$ 3000 km. Trough axis is indicated by dashed lines.

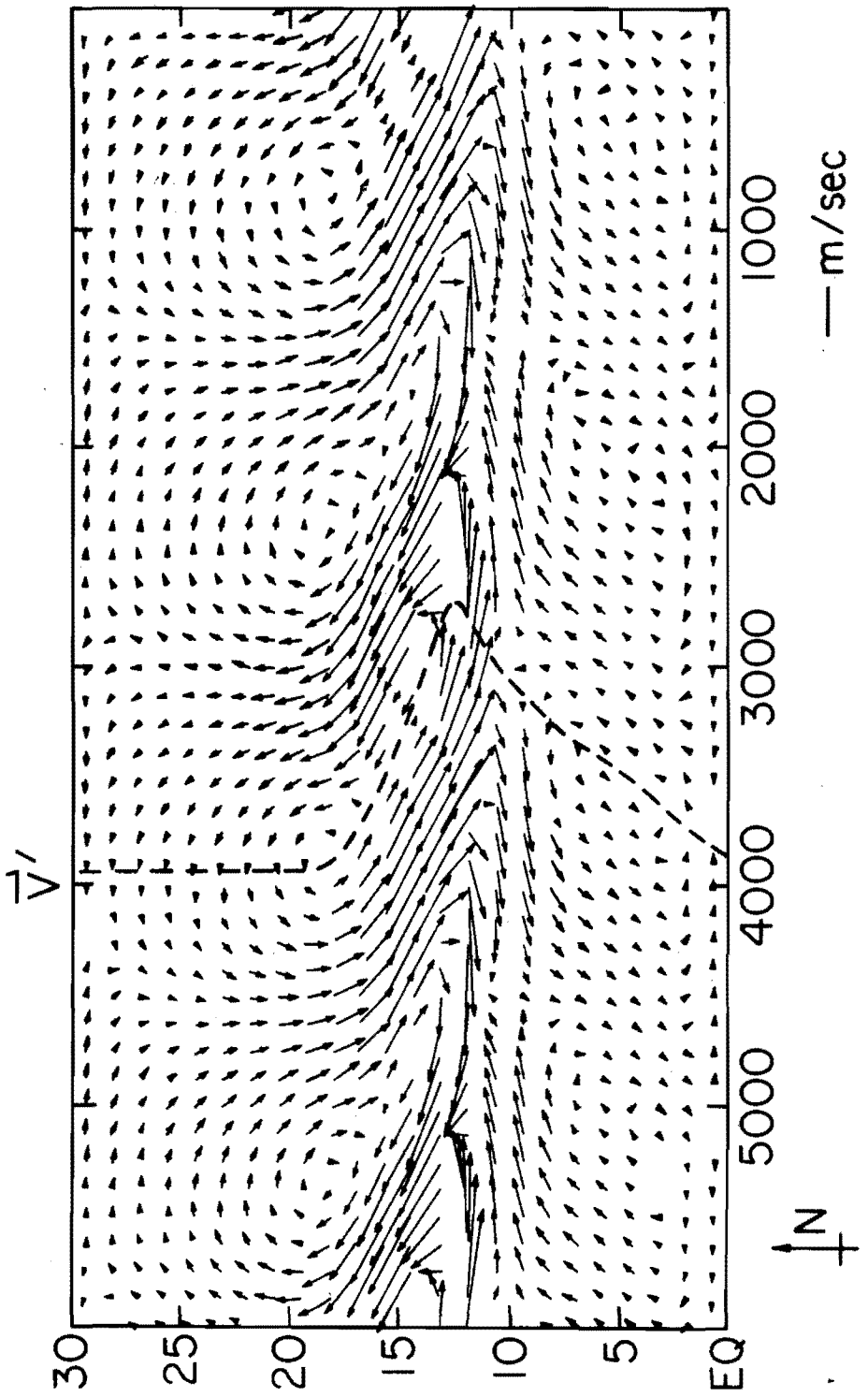
$\overline{V}'$
30
25
20
15
10
5
EQ
5000
4000
3000
2000
1000
N
— m/sec

Figure 5.17. Vertical velocity perturbation shown on x-y plane at 800 mb after 4.6 days. $U = 22.6$ m sec^{-1}, $\lambda =$ 3000 km. Contour interval = $.5 \times 10^{-4}$ mb sec^{-1}.

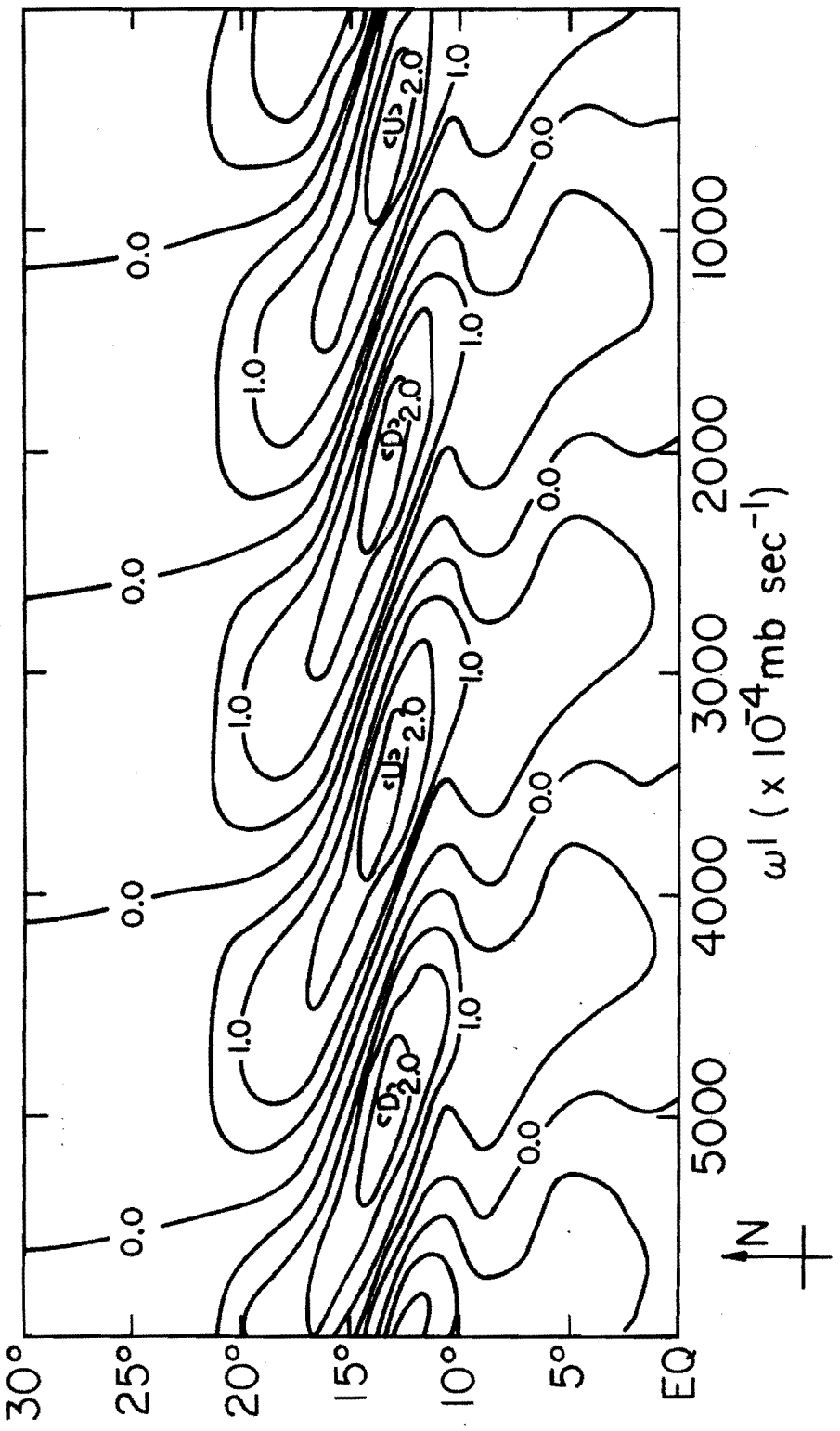
30°
25°
20°
15°
10°
5°
EQ
1000
2000
3000
4000
5000
ω' (x 10⁻⁴mb sec⁻¹)
N
0.0
1.0
2.0
<U>
<D>

Figure 5.18. Geopotential perturbations shown on x-y plane at 700 mb after 4.6 days. $U = 22.6$ m sec^{-1}, $\lambda = 3000$ km. Contour interval = 6.0 m^2 sec^{-2}.

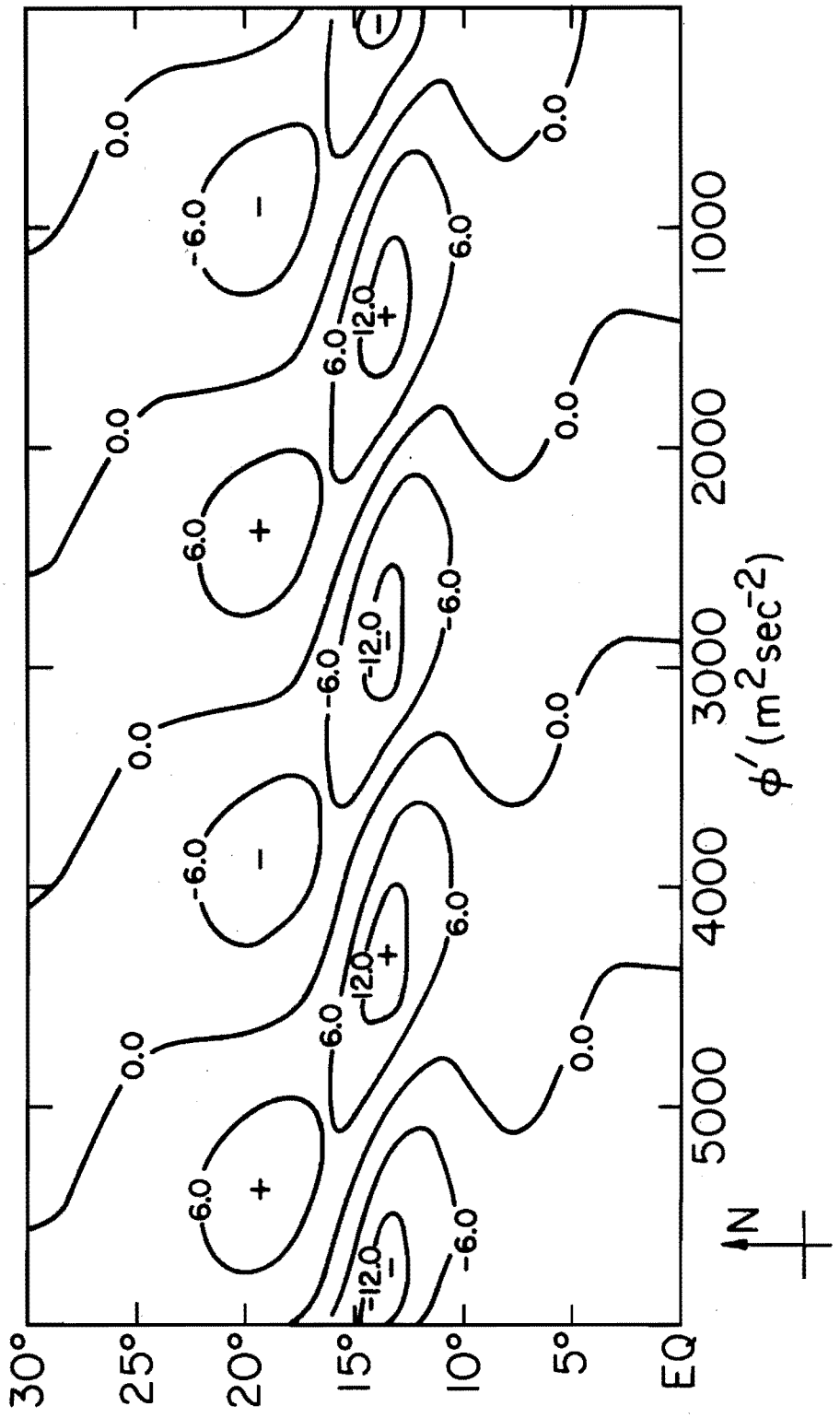
30°
25°
20°
15°
10°
5°
EQ
1000
2000
3000
4000
5000
ϕ' (m^{2}sec^{-2})
N
0.0
6.0
-6.0
12.0
-12.0
+
-

Figure 5.19. Temperature perturbations shown on x-y plane at 800 mb after 4.6 days. U = 22.6 m sec^{-1}, λ = 3000 km. Contour interval = .05C.

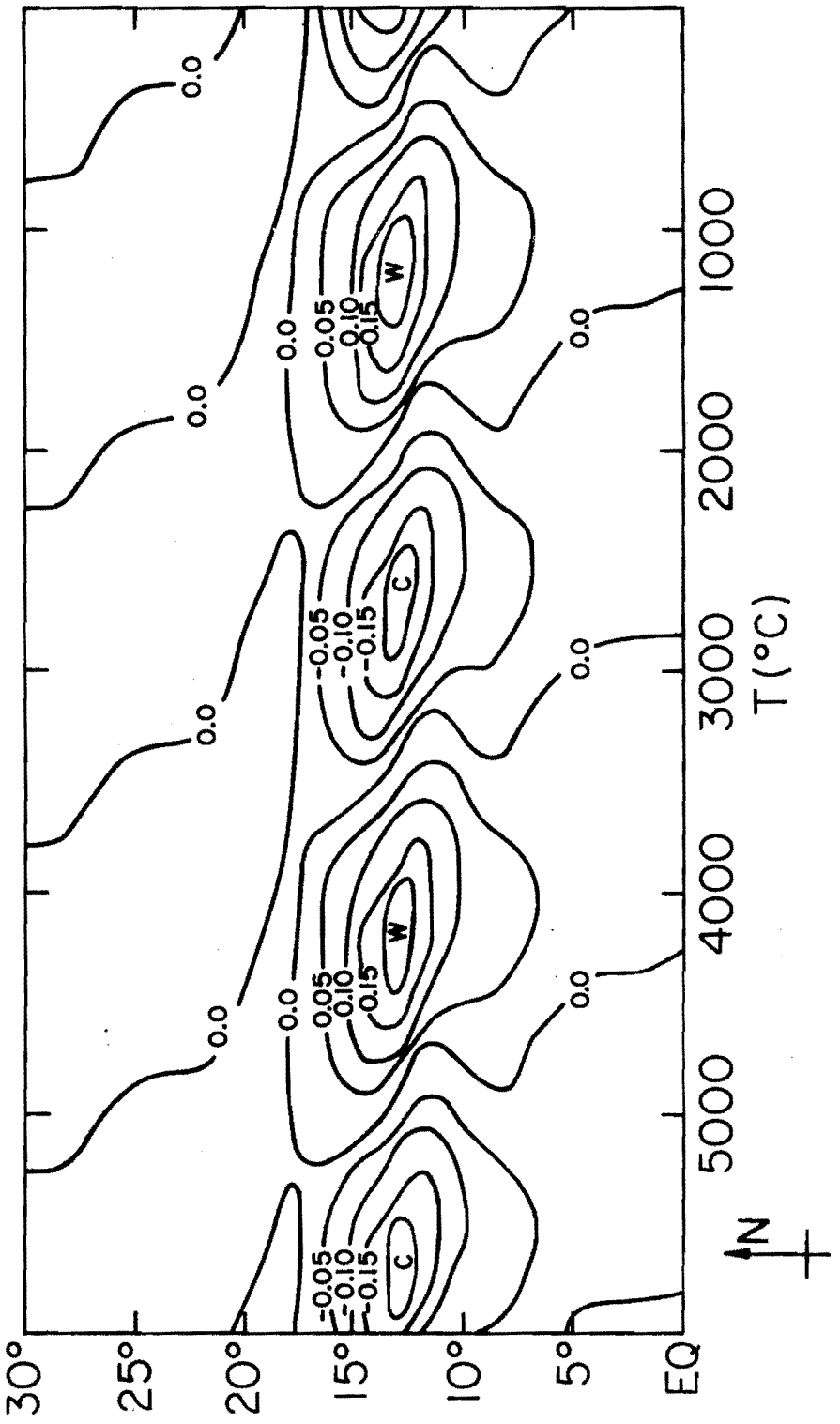
0.0
0.0
0.0
0.0
0.0
0.0
0.0
0.0
0.05
0.10
0.15
W
-0.05
-0.10
-0.15
C
0.05
0.10
0.15
W
-0.05
-0.10
-0.15
C
30°
25°
20°
15°
10°
5°
EQ
5000
4000
3000
2000
1000
T (°C)
N

region of strong zonal perturbation. The axis of the wave trough corresponds to a region of near zero vertical velocity. Upward motion is found just ahead of the trough axis in the region of convergence to the west of the trough. It is difficult to compare these results with the observed vertical velocity fields because the observations do not reveal a consistent pattern of vertical velocities except near the west coast of Africa. There, the vertical motions are more intense than those generated by the model, but the position of the strongest updraft is just ahead of the 700 mb trough, as in the model.

The geopotential perturbation at 700 mb is shown in Figure 5.18. The maximum perturbations coincide with the wind maxima near 13°N, with secondary maxima further north, at 18°N. The regions of negative geopotential perturbation (trough regions) are approximately located at the centers of cyclonic circulation. The phase difference between the geopotential and the meridional wind is such that v' leads ϕ' by slightly less than $\frac{\pi}{2}$.

As seen from Figure 5.19, the magnitude of the temperature perturbation at 800 mb is quite small. However, its relationship to the velocity perturbation is of some interest. The temperature perturbation reaches its largest magnitude near 13°N. This is the same latitude at which the horizontal wind disturbance is large. The center of cyclonic curvature of perturbation wind coincides with the region of coldest air. Thus, below 700 mb, the wave disturbances have cold cores. The region of cold air also coincides with the region in which the vertical motion vanishes. Thus, there can be very little vertical heat transport.

The magnitudes of all the energy conversion terms at the level of maximum wave activity are shown in Figures 5.20 and 5.21. The values of CE_1, CE_2, $-CE_4$, and CE_5 at 700 mb are plotted as functions of latitude in Figure 5.20. The solid line represents the sum of the four terms, i.e. it is the local value of $\frac{\partial EKE}{\partial t}$. This is positive everywhere. CE_1 CE_2, and CE_5 are of approximately equal magnitude and are all important to the growth of the disturbance. CE_4, on the other hand, is smaller than the other terms and may be considered negligible. Large values of the energy conversion terms are confined to the region between 7°N and 20°N.

In the region of principal wave activity, the horizontal Reynolds stress term, CE_1, assumes both positive and negative values. CE_1 contributes to the growth of the disturbance except in the region between 12°N and 14.5°N. It attains its largest positive value, 3.4×10^{-2} watts m^{-2} near 16°N. This represents maximum conversion from zonal kinetic energy to perturbation kinetic energy. The maximum conversion from perturbation to zonal kinetic energy is 2.2×10^{-2} watts m^{-2} near 12.5°N. It is interesting to note that near 12°N, where CE_1 is most negative, the density of perturbation kinetic energy is a maximum. The foregoing implies that CE_1 only partially describes the energetics of the wave in this region. Near 16°N, however, EKE is still large (although not as large as at 12°N) and CE_1 is large and positive. Thus, CE_1 acts as either a source (near 16°N) or a sink (near 12°N) of EKE.

CE_2, the generation of EKE from ZKE by the vertical Reynolds stress, is positive everywhere. Near 15°N it reaches its maximum value of 2.2×10^{-2} watts m^{-2}. Throughout the region of strong wave activity, CE_2

Figure 5.20. Contributions to $\frac{\partial EKE}{\partial t}$ at 700 mb after 4.6 days. $U = 22.6$ m sec^{-1}, $\lambda = 3000$ km.

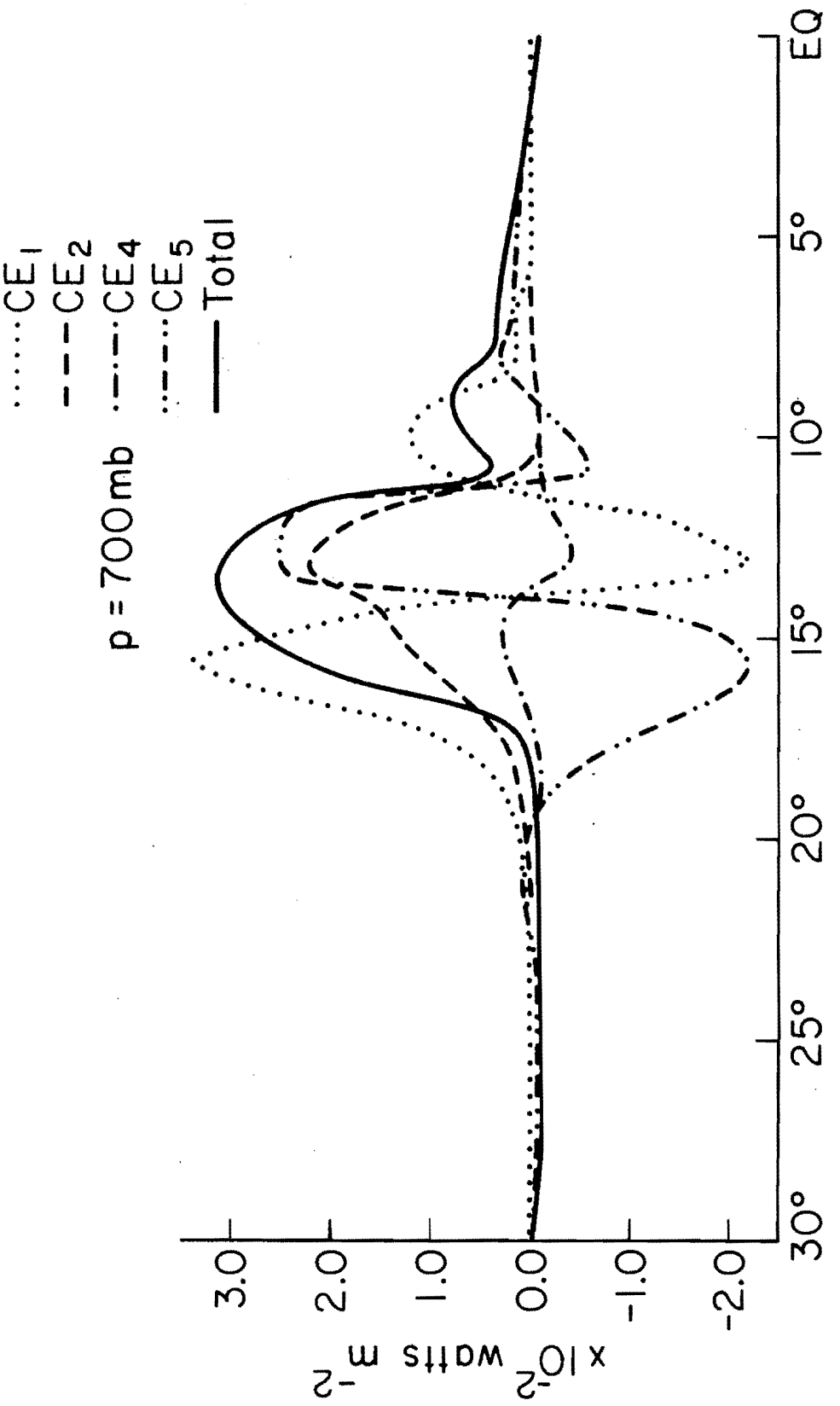
CE1
CE2
CE4
CE5
Total
p = 700 mb
x 10⁻² watts m⁻²
3.0
2.0
1.0
0.0
-1.0
-2.0
30°
25°
20°
15°
10°
5°
EQ

Figure 5.21. Contributions to $\frac{\partial EAPE}{\partial t}$ at 800 mb after 4.6 days. $U = 22.6$ m sec^{-1}, $\lambda = 3000$ km.

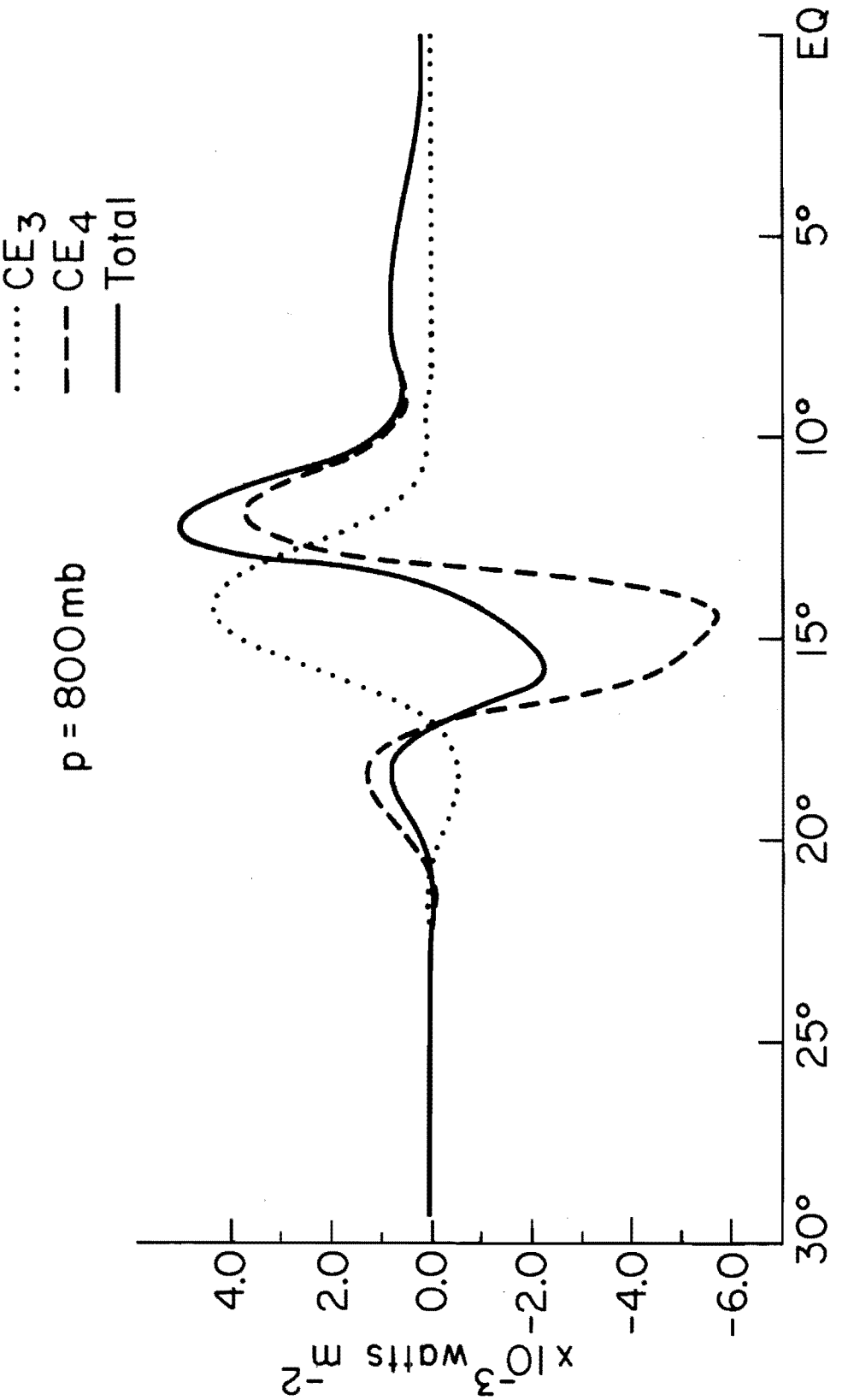
CE3
CE4
Total
p = 800 mb
x 10⁻³ watts m⁻²
4.0
2.0
0.0
-2.0
-4.0
-6.0
30°
25°
20°
15°
10°
5°
EQ

accounts for half or more of the total value of $\frac{\partial EKE}{\partial t}$. CE_2 represents a departure from barotropy, since it depends upon the vertical structure of both the mean jet and the disturbance. However, it does represent a conversion between the mean kinetic energy of the jet and the kinetic energy of the disturbance.

The distribution of CE_5 is almost the inverse of that of CE_1. CE_5 is large and positive where CE_1 is negative. It attains a maximum value of 2.5×10^{-2} watts m^{-2} at 13°N. Farther north, where CE_1 is positive, CE_5 is negative. This means that the pressure gradients which arise as a response to the changing flow field tend to disperse the energy of the disturbance and make the lateral distribution of EKE more uniform.

Although CE_4 is not very significant to the budget of EKE, it is important to the budget of EAPE. The values of CE_3 and CE_4 at 800 mb are plotted in Figure 5.21. Again, the solid line is the sum of the two terms: the local value of $\frac{\partial EAPE}{\partial t}$. Nonzero values of $\frac{\partial EAPE}{\partial t}$ are found at approximately the same latitudes as those at which significant values of $\frac{\partial EKE}{\partial t}$ are found. But the magnitude of $\frac{\partial EAPE}{\partial t}$ is much smaller. Whereas $\frac{\partial EKE}{\partial t}$ approaches 3.2×10^{-2} watts m^{-2}, the maximum value of $\frac{\partial EAPE}{\partial t}$ is only 5.0×10^{-3} watts m^{-2}. Both CE_3 and CE_4 contribute significantly to $\frac{\partial EAPE}{\partial t}$.

CE_3 converts ZAPE to EAPE. It is largest near 15°N. CE_4, the rate to transfer of energy from EKE to EAPE, is positive near 12°N and negative near 15°N. The correlation of CE_3 and CE_4 is such that CE_4 determines the sign of $\frac{\partial EAPE}{\partial t}$ almost everywhere.

These results were obtained under the assumption that the stability of the atmosphere with respect to gravitational overturning is due solely to the stratification of T. The contribution due to the deviations of the temperature from its average value on a constant pressure surface was neglected. In order to determine the consequences of this assumption, an additional term, $\left(\frac{\partial [\bar{T}]^*}{\partial p} - \frac{\kappa [\bar{T}]^*}{p} \right) \omega'$, was included in the thermodynamic equation. The temperature perturbation was then governed by (4.3) with $Q' = 0$. This change modifies the energy equation for EAPE, (4), by adding the term CE_7, defined by (4.23).

The effect of this modification of the model may be anticipated by considering the relative magnitudes of σ and $\left(\frac{\partial [\bar{T}]^*}{\partial p} - \frac{\kappa [\bar{T}]^*}{p} \right)$. At 800 mb, the level at which $[T'\omega']$ is largest, the magnitude of $\left(\frac{\partial [\bar{T}]^*}{\partial p} - \frac{\kappa [\bar{T}]^*}{p} \right)$ is at most 10% of the magnitude of σ. Thus, it is not surprising that, aside from a slight increase in EAPE, the model results are nearly unchanged by inclusion of lateral variations of the stability parameter. The growth rate of ETE is about .40 day^{-1}, instead of .36 day^{-1}. The perturbation fields after 4.6 days are shown in Figures 5.22 and 5.23. Comparison of these figures with Figures 5.12 and 5.13 shows that the magnitudes of the perturbations have been increased slightly, but their form is unchanged.

The results of the dry primitive equation model indicate that the most unstable wave generated by the model, the 3000 km wave, is quite similar to the observed African waves. The disturbance is essentially horizontal in nature; the vertical velocity and temperature perturbations associated with it are small. The wave energy is confined primarily to the 700 mb level, and to the latitude band between 7°N and 20°N. The

Figure 5.22. Wind perturbations after 4.6 days with lateral variations of the stability parameter included in the thermodynamic equation. $U = 22.6$ m sec^{-1}, $\lambda = 3000$ km. u' contour interval = .5 m sec^{-1}. v' contour interval = .2 m sec^{-1}. ω' contour interval = $.6 \times 10^{-4}$ mb sec^{-1}.

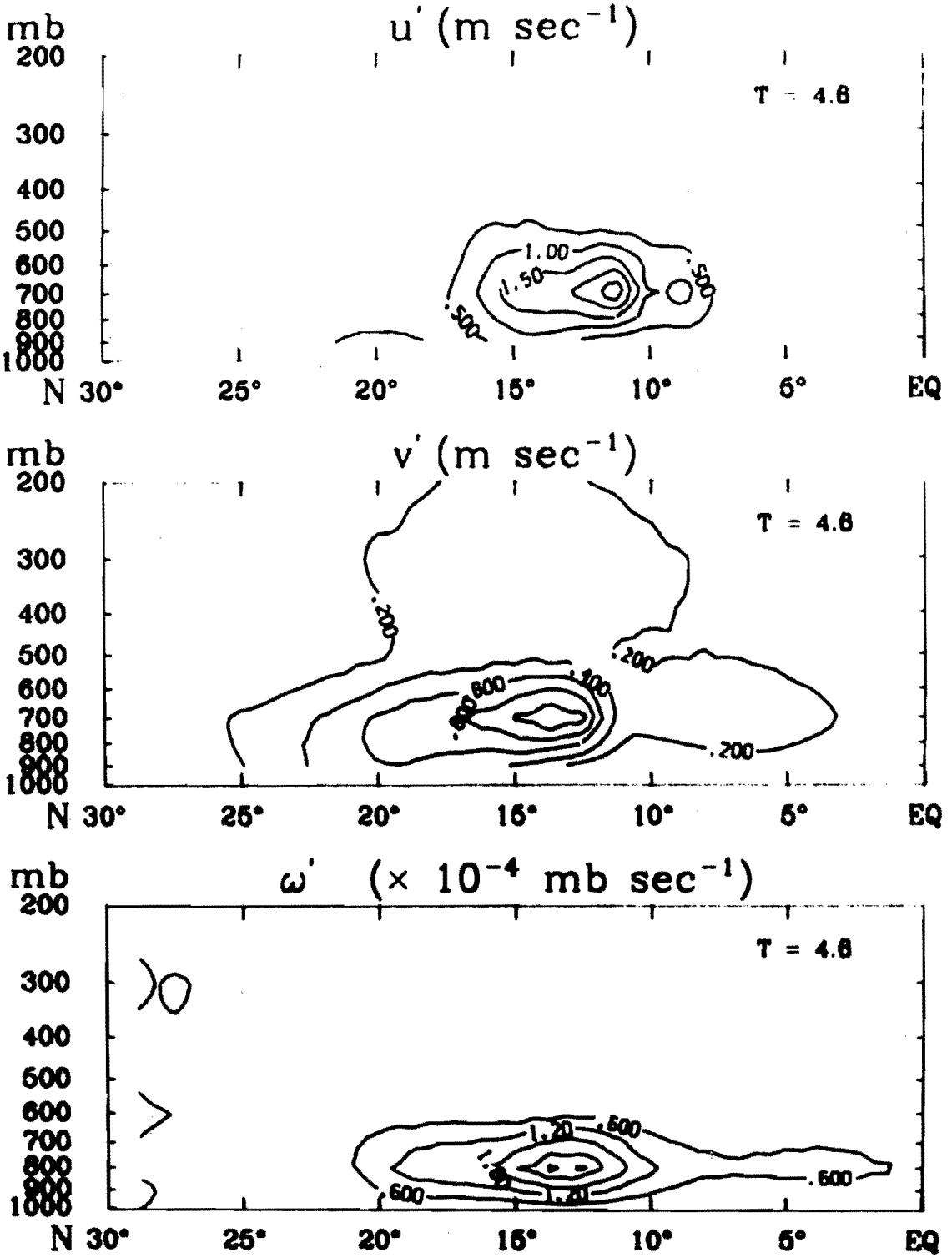
mb
u' (m sec⁻¹)
T = 4.6
1.00
1.50
.500
.500
mb
v' (m sec⁻¹)
T = 4.6
.200
.200
.600
.400
.200
mb
ω' (× 10⁻⁴ mb sec⁻¹)
T = 4.6
1.20
.600
.600
1.20
200
300
400
500
600
700
800
900
1000
N 30°
25°
20°
15°
10°
5°
EQ

Figure 5.23. Temperature and geopotential perturbations after 4.6 days with lateral variations of the stability parameter included in the thermodynamic equation. U = 22.6 m sec^{-1}, λ = 3000 km. T' contour interval = .05 C. ϕ' contour interval = 3.0 m^2 sec^{-2}.

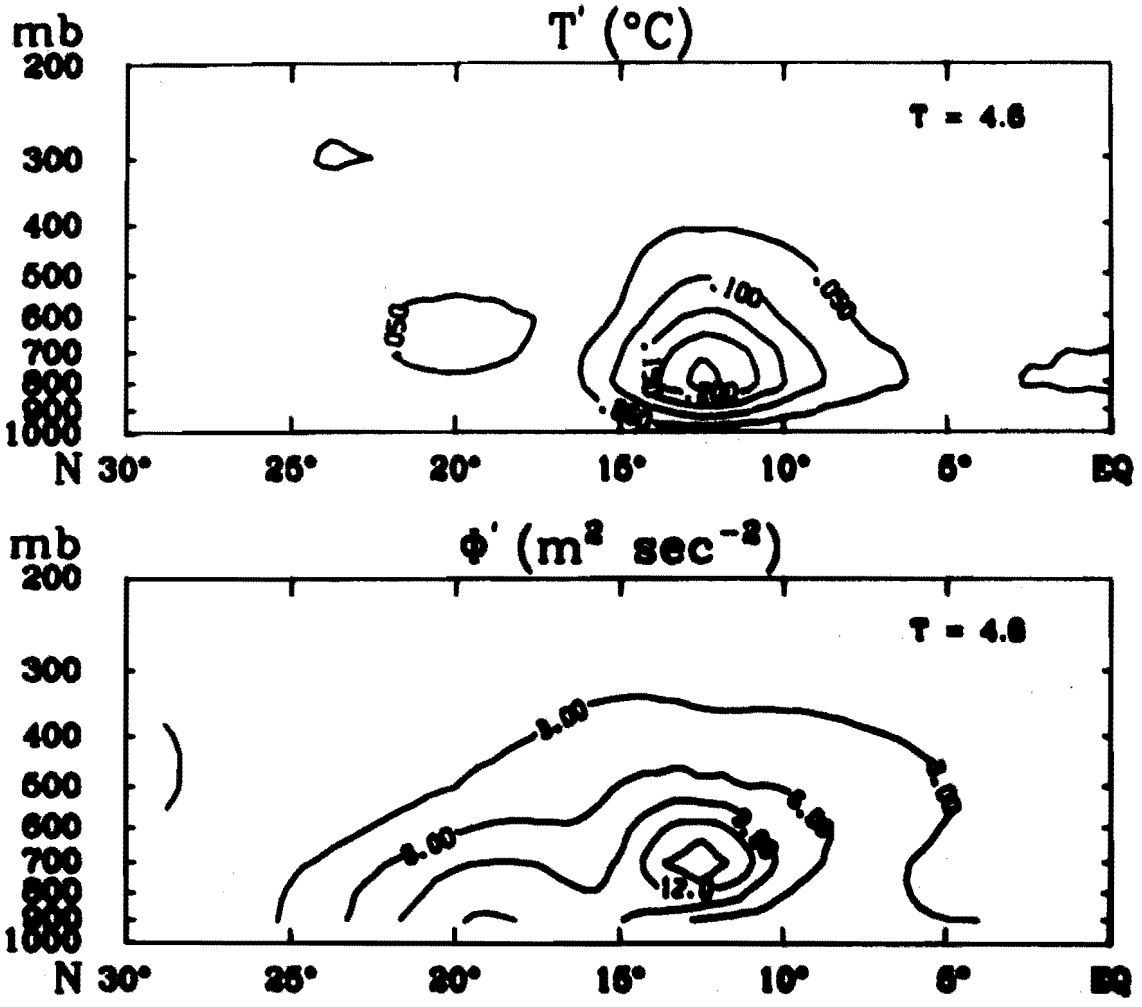
T' (°C)
mb
200
300
400
500
600
700
800
900
1000
T = 4.6
.050
.100
.050
N 30°
25°
20°
15°
10°
5°
EQ
Φ' (m² sec⁻²)
mb
200
300
400
500
600
700
800
900
1000
T = 4.6
4.00
8.00
12.
N 30°
25°
20°
15°
10°
5°
EQ

geopotential perturbation lags the meridional velocity perturbation by slightly less than $\frac{\pi}{2}$. The temperature perturbation, however, is approximately in phase with the geopotential perturbation, so that the disturbance has a cold core.

The most noticable difference between the observed waves and those generated by the model concerns the horizontal slope of the trough axis. Between the equator and about 13°N the trough axis at 700 mb is fairly well defined in the data (Burpee, 1975), and slopes from southwest to northeast. The model wave exhibits similar behavior in this region. Near the center of the jet, the observed slope of the trough axis becomes much more gradual, up to 20°N. To the north of 20°N the upper air data is too sparse to allow the tilt of the trough axis to be defined. The axis of the model wave behaves somewhat differently. Near the jet maximum, the tilt of the trough axis reverses, and slopes quite strongly from southeast to northwest. While this would seem to be in marked disagreement with the observations, it must be remembered that the absence of upper air stations makes it extremely difficult to estimate the tilt reliably. Furthermore, the data does indicate a reversal of the tilt of the wave if the ridge axis, rather than the trough axis, is considered. (See Figure 2.5)

The wave is maintained and grows at the expense of the kinetic energy of the jet. Easterly momentum is transported away from the jet by the vertical Reynolds stress and, north of 14°N, by the horizontal Reynolds stress. Between 11°N and 14°N the disturbance loses energy to the mean flow through the horizontal Reynolds stress, but this is compensated for by a redistribution of the disturbance energy generated farther north.

The net effect is that the disturbance energy increases everywhere. The source of the energy is the kinetic energy of the mean zonal flow. The available potential energy of the mean zonal flow is of little importance in the overall energy budget, since very little of it is converted to disturbance energy.

The role of the horizontal transport of easterly momentum in the generation of the waves is as expected. The observed mean flow at 700 mb easily satisfies the theoretical condition necessary for instability. The results of the barotropic model confirm that the flow at 700 mb can support instabilities on the scale of African waves, due to its horizontal shear. The primitive equation model shows that this mechanism continues to operate in a baroclinic atmosphere, although the lateral distribution of the momentum transport is altered by the inclusion of non-barotropic processes.

From the standpoint of linear stability theory, it is not obvious that the vertical transport of horizontal momentum should be important. Although the vertical profile of the mean flow does exhibit an inflection point, the stable stratification is expected to prevent the growth of inflection point instabilities. That this is indeed the case was demonstrated by using the model to investigate the stability of a mean flow which is horizontally uniform, and which has a vertical structure defined by that of the observed flow at 15°N. The results show that the only instability in this case is due to conversion of ZAPE to EAPE, and then to EKE. The vertical transport of easterly momentum acts as a sink of disturbance energy. A quasi-geostrophic system would not allow the mechanism to operate at all. This implies that the role of vertical

momentum transport in the generation of African waves is due to interactions between barotropic and baroclinic mechanisms, not to a singly identifiable effect.

The horizontal transport of heat, and the accompanying overturning are of minor importance in the generation of the waves. This result is expected on the basis of quasi-geostrophic theory, and is confirmed by the model.

4. Moist Model

Based on the results of a crude parameterization of latent heat release, the importance of moisture in the generation of African waves may be estimated. The results of the moist model can be applied only to the generation and initial growth of the waves, because the parameterization scheme ignores factors, such as the southwest monsoon circulation in the Gulf of Guinea, which affect the moisture field near the west coast of Africa. However, despite the crudeness of the model, it should give a good indication of how moisture affects the early development of the waves. After 4.6 days of integration, the wind perturbations generated by the model are of the same magnitude as those of the observed waves. At that same time, the model generates about 2.5 mm day^{-1} of rainfall in the trough regions. This is compatible with Burpee's observation (1974) that the excess rainfall in the trough region over the ridge region is about 3 mm day^{-1}.

The disturbance to be considered in detail is the 3000 km wave in a mean jet with maximum intensity 22.6 m sec^{-1}. The most striking feature of the results is that they differ only slightly from those of

the dry model. The growth rate of total energy after 4.6 days is .33 day^{-1}. This differs little from the growth rate attained by the disturbance in the dry model, but it is less clear that a single normal mode is dominating the disturbance and that the system has reached its asymptotic state. Both EKE and EAPE are slightly larger in the moist model than in the dry model, but EKE still accounts for about 90% of the total energy. Figure 5.24 shows the amplitudes of the horizontal wind and temperature perturbations for the moist model. The distributions of these quantities are very similar to those for the dry model. The only significant difference is the increased magnitude of the temperature perturbation.

The energetics of the moist model are very similar to those of the dry model. The kinetic energy budgets for the two systems are exactly the same. The budget for available potential energy contains an additional term which depends on the diabatic heating rate. The local energy balance equations are:

$$\frac{\partial EKE}{\partial t} = CE_1 + CE_2 - CE_4 + CE_5 + CE_6$$

$$\frac{\partial EAPE}{\partial t} = CE_3 + CE_4 + CE_8$$

where the conversion terms are defined by (4.17) - (4.24).

The impact of CE_8 on the energetics of the system can be evaluated from Figures 5.25 and 5.26. CE_8 itself is generally positive, and attains its maximum value of about 3.5×10^{-3} watts m^{-2} near 13°N. This is slightly larger than the maximum value of $\frac{\partial EAPE}{\partial t}$ in the dry model. CE_4, the term representing exchange between EKE and EAPE has a very sharp peak near 13°N where EKE is converted to EAPE at the rate of 12.6×10^{-3}

Figure 5.24. Horizontal wind and temperature perturbations after 4.6 days for the moist model. $U = 22.6$ m sec^{-1}, $\lambda = 3000$ km. u' contour interval = .5 m sec^{-1}. v' contour interval = .2 m sec^{-1}. T' contour interval = .04 C.

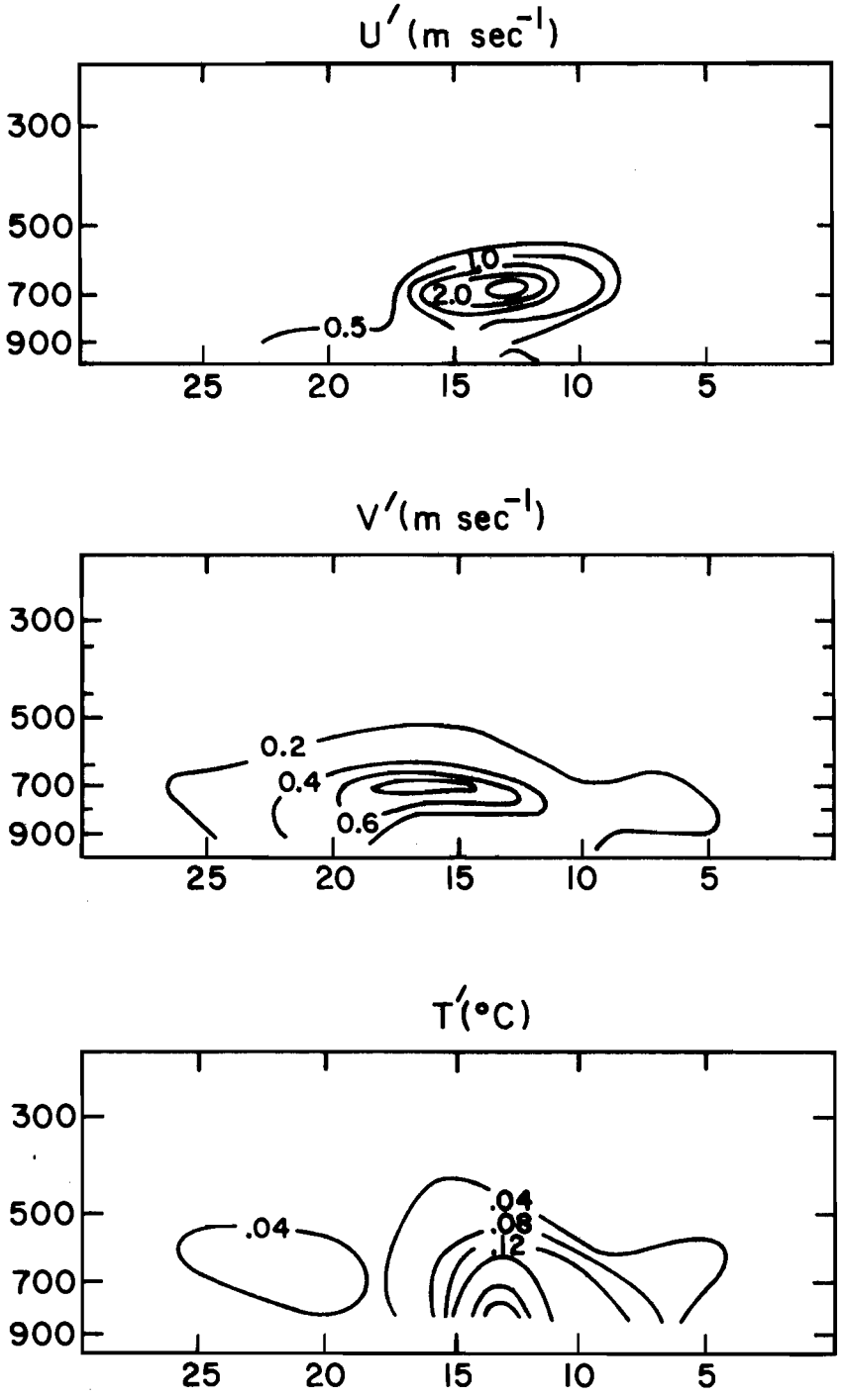
U′(m sec⁻¹)
300
500
700
900
1.0
2.0
0.5
25
20
15
10
5
V′(m sec⁻¹)
300
500
700
900
0.2
0.4
0.6
25
20
15
10
5
T′(°C)
300
500
700
900
.04
.04
.08
.12
25
20
15
10
5

watts m^{-2}. Since CE_3 is not greatly affected by the release of latent heat, it loses relative importance in the budget of EAPE. CE_4 and CE_8 essentially determine that budget in the moist model.

Despite the fact that release of latent heat significantly influences the EAPE budget, it is not very significant to the overall energetics of the wave. According to Figure 5.25, the maximum values attained by CE_1 and CE_2 are slightly larger in the moist model than in the dry model, but their general characteristics are quite similar in the two models. Although CE_4 is large compared to CE_3 in the moist model, it is still very small compared to other sources of kinetic energy.

The results of the moist model indicate that the generation of EAPE is enhanced by the release of latent heat. However, because EAPE represents only a small percentage of the total wave energy, the resultant increase in EAPE is insufficient to significantly change the stability of the disturbance. Diabatic heating due to the release of latent heat cannot be of vital importance in the generation of African waves.

Figure 5.25. Contributions to $\frac{\partial EKE}{\partial t}$ at 700 mb in moist model after 4.6 days. U = 22.6 m sec^{-1}, λ = 3000 km.

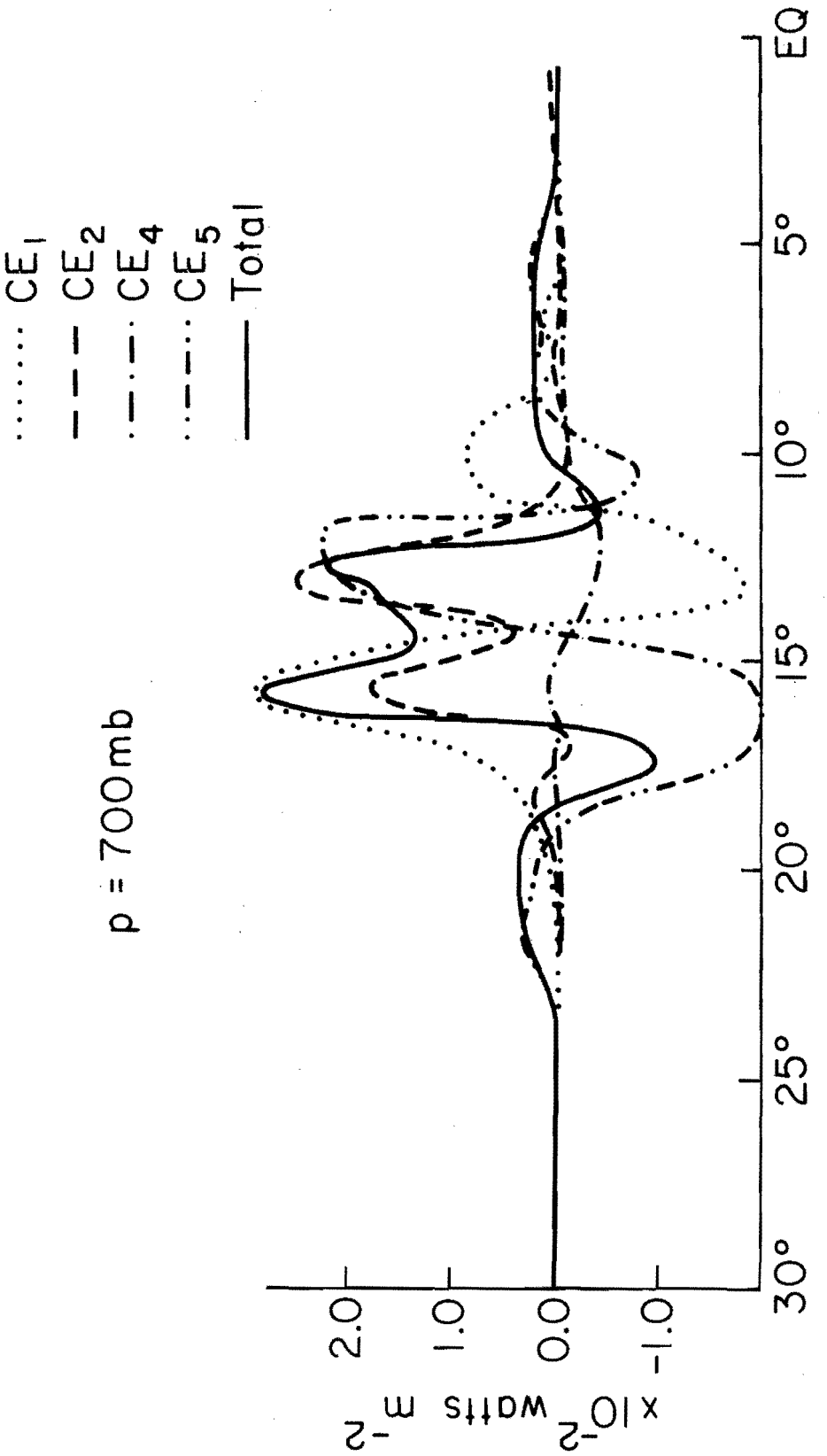
CE1
CE2
CE4
CE5
Total
p = 700 mb
x 10-2 watts m-2
2.0
1.0
0.0
-1.0
30°
25°
20°
15°
10°
5°
EQ

Figure 5.26. Contributions to $\frac{\partial EAPE}{\partial t}$ at 800 mb in moist model after 4.6 days. $U = 22.6$ m sec^{-1}, $\lambda = 3000$ km.

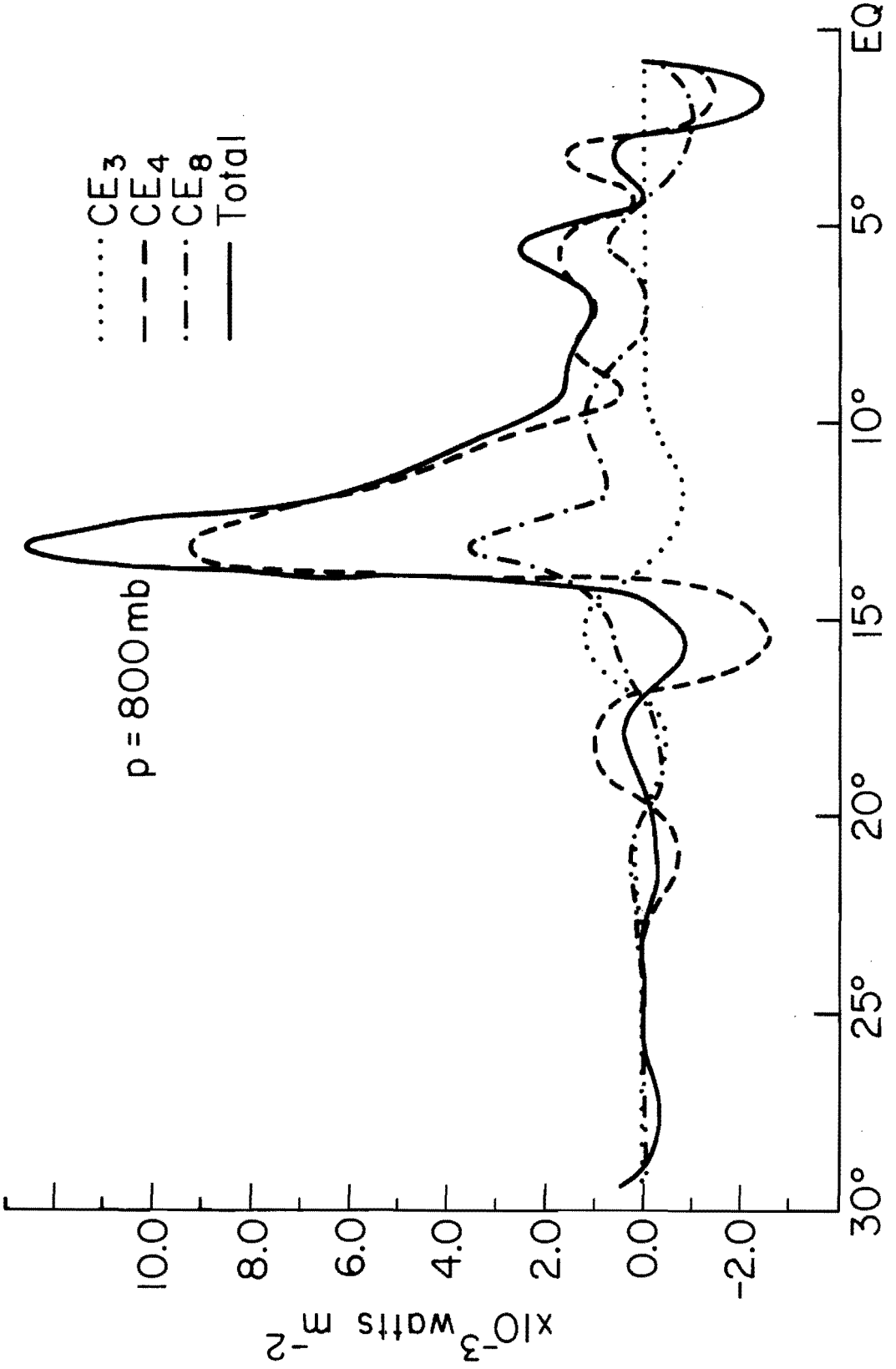
CE3
CE4
CE8
Total
p = 800mb
EQ
5°
10°
15°
20°
25°
30°
10.0
8.0
6.0
4.0
2.0
0.0
-2.0
x10⁻³ watts m⁻²

VI. NONLINEAR MODEL

1. Structure of the Nonlinear Model

The linear model shows that the observed zonal flow is unstable to disturbances on the scale of African waves. The source of the wave energy is the kinetic energy of the mean zonal flow. Observations show that the waves are generated continuously throughout a two to three month season. Thus the mean flow must provide a continuous source of energy to the waves. This transfer of energy from the mean flow to the waves can continue only as long as the instability of the mean flow is maintained. As the waves extract energy from the mean flow, they can alter the mean flow, and stabilize it. Since the major instability mechanism depends upon the curvature of the flow, it can be quite sensitive to small changes in the zonal wind field.

The linear model breaks down when the perturbation becomes large enough so that the nonlinear terms which were neglected in equations (3.14) - (3.16) are significant when compared to the linear terms. After 4.6 days, the zonal wind perturbation is sufficiently large so that the magnitude of the largest nonlinear terms is about 30% of the magnitude of the smallest linear terms. This is about the limit of the validity of the linear model. In addition to its inability to represent the nonlinear terms in the perturbation equations, the linear model also fails to represent the response of the basic state to the growth of the waves. In order to investigate the maintenance of the instability of the jet, it is necessary to consider nonlinear effects. The complexity of the

fully nonlinear primitive equations can be avoided, however, by considering the physical phenomena to be modeled.

There are two essential points which a model must address. The first is the extent to which the waves modify the stability of the zonally averaged flow. To do this, the model must allow a two way interaction between the waves and the zonally averaged flow. [u] cannot be forced to remain constant with respect to time. Processes which convert ZKE to EKE must indeed deplete the supply of ZKE, and thus change the zonally averaged wind field, rather than leave ZKE unaltered, under the assumption that any such changes are small, and therefore negligible. In addition to finding the response of the basic state to the wave motions, the model is also required to determine the nature of the meridional circulation generated in response to surface heating.

Burpee (1972) has suggested that the low level jet is maintained by a thermally direct low level circulation driven by the surface temperature gradient. According to his hypothesis, waves are generated as instabilities on the low level jet, and grow at the expense of the jet energy. The instability of the jet is maintained by a meridional circulation in which warm air rises at the northern edge of the desert (near 25°N) and (relatively) cool air sinks near the equator. This implies a southerly flow at the surface, with the return flow at mid levels. The southward moving air near 600-700 mb must be turned westward in order to conserve absolute angular momentum, thereby acting to maintain the jet.

Simple computations using the thermal wind equation (3.13) lend some support to this model. Figure 6.1 shows the observed surface temperature and vertical shear of the zonal wind between the surface and 700 mb. Also shown is the vertical wind shear derived geostrophically,

Figure 6.1. Surface temperatures at 5°E (solid line), observed wind shear between the surface and 700 mb (dotted line), and wind shear computed from surface temperature gradient from the geostrophic thermal wind equation (dashed line).

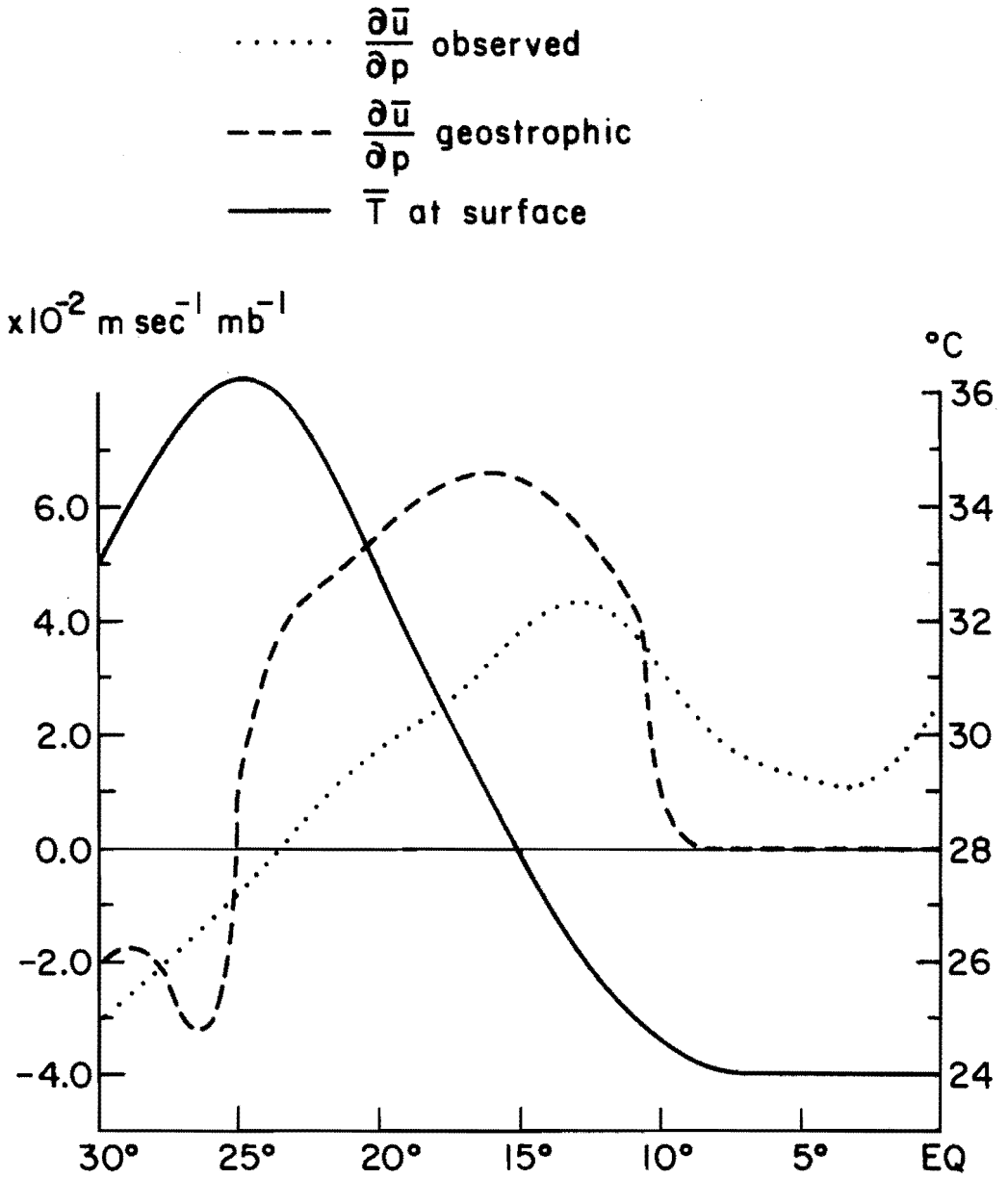
$\frac{\partial \bar{u}}{\partial p}$ observed
$\frac{\partial \bar{u}}{\partial p}$ geostrophic
$\bar{T}$ at surface
x10^{-2} m sec^{-1} mb^{-1}
°C
6.0
4.0
2.0
0.0
-2.0
-4.0
36
34
32
30
28
26
24
30°
25°
20°
15°
10°
5°
EQ

from the surface temperature gradient. The agreement between the two shear curves is somewhat questionable. The surface temperature gradient is sufficiently strong to support the observed vertical shear. Indeed, the maximum shear implied by the temperature gradient is about 50% greater than the largest observed shear. The latitudinal variation of the observed vertical shear is considerably different from that computed from the thermal wind equation. However, knowledge of the average horizontal temperature gradient throughout the layer between the surface and 700 mb, rather than just the surface temperature gradient, would be required to accurately compute the vertical shear of the geostrophic zonal wind. Thus, it is not clear whether the disagreement between the two curves for $\frac{\partial[\bar{u}]}{\partial p}$ is due to the fact that the surface temperature gradient does not accurately reflect the temperature gradient throughout the layer, or to the importance of ageostrophic effects.

In order to investigate these two points, the zonal average of the primitive equations (3.1 - 3.3) is taken. The resulting equations governing the zonally averaged flow are:

$$\frac{\partial[u]}{\partial t} + [v]\frac{\partial[u]}{\partial y} + [\omega]\frac{\partial[u]}{\partial p} - f[v] + [u'\frac{\partial u'}{\partial x}] + [v'\frac{\partial u'}{\partial y}] + [\omega'\frac{\partial u'}{\partial p}] = 0 \quad (1)$$

$$\frac{\partial[v]}{\partial t} + [v]\frac{\partial[v]}{\partial y} + [\omega]\frac{\partial[v]}{\partial p} + f[u] + \frac{\partial[\phi]^*}{\partial y} + [u'\frac{\partial v'}{\partial x}] + [v'\frac{\partial v'}{\partial y}] + [\omega'\frac{\partial v'}{\partial p}] = 0 \quad (2)$$

$$\frac{\partial[T]^*}{\partial t} + [v]\frac{\partial[T]^*}{\partial y} + [\omega]\left(\frac{\partial[T]^*}{\partial p} - \frac{\kappa[T]^*}{p}\right) + [\omega]\sigma + [u'\frac{\partial T'}{\partial x}] + [v'\frac{\partial T'}{\partial y}] + [\omega'\left(\frac{\partial T'}{\partial p} - \frac{\kappa T'}{p}\right)] = [Q]^* \quad (3)$$

$$\frac{\partial [\phi]^*}{\partial p} + \frac{R[T]^*}{p} = 0 \tag{4}$$

$$\frac{\partial [v]}{\partial y} + \frac{\partial [\omega]}{\partial p} = 0 \tag{5}$$

These equations are subtracted from the primitive equations to obtain the equations governing the perturbations:

$$\frac{\partial u'}{\partial t} + [u]\frac{\partial u'}{\partial x} + [v]\frac{\partial u'}{\partial y} + v'\frac{\partial [u]}{\partial y} + [\omega]\frac{\partial u'}{\partial p} + \omega'\frac{\partial [u]}{\partial p} - fv' + \frac{\partial \phi'}{\partial x}$$

$$+ u'\frac{\partial u'}{\partial x} - [u'\frac{\partial u'}{\partial x}] + v'\frac{\partial u'}{\partial y} - [v'\frac{\partial u'}{\partial y}] + \omega'\frac{\partial u'}{\partial p} - [\omega'\frac{\partial u'}{\partial p}] = 0 \tag{6}$$

$$\frac{\partial v'}{\partial t} + [u]\frac{\partial v'}{\partial x} + [v]\frac{\partial v'}{\partial y} + v'\frac{\partial v'}{\partial y} + [\omega]\frac{\partial v'}{\partial p} + \omega'\frac{\partial [v]}{\partial p} + fu' + \frac{\partial \phi'}{\partial y}$$

$$+ u'\frac{\partial v'}{\partial x} - [u'\frac{\partial v'}{\partial x}] + v'\frac{\partial v'}{\partial y} - [v'\frac{\partial v'}{\partial y}] + \omega'\frac{\partial v'}{\partial p} - [\omega'\frac{\partial v'}{\partial p}] = 0 \tag{7}$$

$$\frac{\partial T'}{\partial t} + [u]\frac{\partial T'}{\partial x} + [v]\frac{\partial T'}{\partial y} + v'\frac{\partial [T]^*}{\partial y} + [\omega]\left(\frac{\partial T'}{\partial p} - \frac{\kappa T'}{p}\right) + \omega'\left(\frac{\partial [T]^*}{\partial p} - \frac{\kappa [T]^*}{p}\right)$$

$$+ \omega'\sigma + u'\frac{\partial T'}{\partial x} - [u'\frac{\partial T'}{\partial x}] + v'\frac{\partial T'}{\partial y} - [v'\frac{\partial T'}{\partial y}] + \{\omega'\frac{\partial T'}{\partial p} - \frac{\kappa T'}{p}$$

$$- [\omega'(\frac{\partial T'}{\partial p} - \frac{\kappa T'}{p})]\} = Q' \tag{8}$$

$$\frac{\partial \phi'}{\partial p} + \frac{RT'}{p} = 0 \tag{9}$$

$$\frac{\partial u'}{\partial x} + \frac{\partial v'}{\partial y} + \frac{\partial \omega'}{\partial p} = 0 \qquad (10)$$

The notation used here is the same as that used in Chapter 2.

The only terms in equations (6) - (10) which are nonlinear in perturbation variables are those which represent the transport of the momentum or heat associated with the perturbation by the perturbation wind field. It is through these terms that disturbances of different wavelengths are coupled. But the interaction between different wavelengths is of no particular interest for this study. The linear model indicates that the mean flow supports unstable disturbances in only a limited range of wavelengths. Then, any waves which are generated by nonlinear interactions between unstable waves are not unstable themselves. Instead, they are damped, and dissipate their energy through turbulent motions. Thus, the nonlinear terms act primarily as a small sink for wave energy. They may be approximated by a term which is proportional to the magnitude of the perturbation, and opposite to it in sign. This formulation is similar to that used by Holton and Colton (1972). It is assumed that the wave motions are adiabatic, so that $Q' = 0$.

With these approximations, equations (6), (7), and (8) become

$$\frac{\partial u'}{\partial t} + [u]\frac{\partial u'}{\partial x} + [v]\frac{\partial u'}{\partial y} + v'\frac{\partial [u]}{\partial y} + [\omega]\frac{\partial u'}{\partial p} + \omega'\frac{\partial [u]}{\partial p} - fv' + \frac{\partial \phi'}{\partial x} - \alpha u' = 0 \qquad (11)$$

$$\frac{\partial v'}{\partial t} + [u]\frac{\partial v'}{\partial x} + [v]\frac{\partial v'}{\partial y} + v'\frac{\partial [v]}{\partial y} + [\omega]\frac{\partial v'}{\partial p} + \omega'\frac{\partial [v]}{\partial p} + fu' + \frac{\partial \phi'}{\partial y} - \alpha v' = 0 \qquad (12)$$

$$\frac{\partial T'}{\partial t} + [u]\frac{\partial T'}{\partial x} + [v]\frac{\partial T'}{\partial y} + v'\frac{\partial [T]^*}{\partial y} + [\omega]\left(\frac{\partial T'}{\partial p} - \frac{\kappa T'}{p}\right) + \omega'\left(\frac{\partial [T]^*}{\partial p} - \frac{\kappa [T]^*}{p}\right)$$

$$+ \omega'\sigma - \alpha T' = 0 \qquad (13)$$

Equations (11), (12), and (13), along with (9) and (10) govern the deviations from the zonal mean in the nonlinear model.

The perturbation terms in the zonally averaged equations can be simplified somewhat by writing them in flux form. For example,

$$[u'\frac{\partial u'}{\partial x}] + [v'\frac{\partial u'}{\partial y}] + [\omega'\frac{\partial u'}{\partial p}] = [\frac{\partial}{\partial x} u'u'] + [\frac{\partial}{\partial y} u'v'] + [\frac{\partial}{\partial p} u'\omega']$$

$$- [u'\frac{\partial u'}{\partial x} + u'\frac{\partial v'}{\partial y} + u'\frac{\partial \omega'}{\partial p}]$$

Making use of the continuity equation for the perturbation, (10), noting that the zonal averaging operation [ ] is independent of y and p and therefore commutes with $\frac{\partial}{\partial y}$ and $\frac{\partial}{\partial p}$, and assuming that the perturbations are periodic in x, so that $\frac{\partial}{\partial x} u'u' = 0$, this expression becomes

$$\frac{\partial}{\partial y} [u'v'] + \frac{\partial}{\partial p} [u'\omega']$$

It is convenient to define a zonally averaged stream function $[\chi]$ such that $[v] = -\frac{\partial [\chi]}{\partial p}$ and $[\omega] = \frac{\partial [\chi]}{\partial y}$. Then (5) is satisfied identically, and the momentum equations (1) and (2) may be rewritten:

$$\frac{\partial [u]}{\partial t} - J([u], [\chi]) - f[v] + \frac{\partial}{\partial y} [u'v'] + \frac{\partial}{\partial p} [u'\omega'] = 0 \qquad (14)$$

$$\frac{\partial [v]}{\partial t} - J([v], [\chi]) + f[u] + \frac{\partial [\phi]^*}{\partial y} + \frac{\partial}{\partial y}[v'v'] + \frac{\partial}{\partial p}[v'\omega'] = 0 \quad (15)$$

where $J(a,b)$ is the jacobian of a and b, defined by $J(a,b) = \frac{\partial a}{\partial y}\frac{\partial b}{\partial p} - \frac{\partial b}{\partial y}\frac{\partial a}{\partial p}$.

The diabatic heating, $[Q]^*$, is assumed to vanish, except near the surface, where some heating occurs. The amount of heating is proportional to the difference between the potential temperature at the surface and that at 900 mb. The surface is considered to be an infinite source/sink of heat, maintained at a constant temperature by solar radiation. The thermodynamic equation (3) then becomes

$$\frac{\partial [T]^*}{\partial t} - J([T]^*, [\chi]) - \frac{\kappa}{p}[T]^*[\omega] + [\omega]\sigma + \frac{\partial}{\partial y}[T'v'] + \left(\frac{\partial}{\partial p} - \frac{\kappa}{p}\right)[T'\omega'] = [Q]^* \quad (16)$$

with

$$[Q]^* = \begin{cases} K_H \left(\frac{\partial [T]^*}{\partial p} - \frac{\kappa [T]^*}{p}\right) \text{ at 900 mb} \\ 0 \quad \text{elsewhere} \end{cases} \quad (17)$$

Equations (14), (15), (16), (4), and the definition (17) govern the zonally averaged motions of the atmosphere. These equations, and equations (9) - (13), are energetically consistent, if triple correlation terms are small enough to be disregarded.

A numerical solution to these equations is obtained by a method similar to that used in the linear model. Only the perturbation quantities have x dependence, and this is given by $\xi'(x,y,p,t) = \xi_1(y,p,t)\sin kx + \xi_2(y,p,t)\cos kx$. The coefficients ξ_1 and ξ_2, and the zonally averaged

quantities, $[\xi](y,p,t)$, are defined on a grid in the y-p plane. The grid system is shown in Figure 6.2. The principal difference between this grid and the one on which the linear equations are solved is the vertical resolution. The terms involving vertical derivatives of perturbation quantities require that Δp be reduced from 200 mb to 100 mb. Otherwise, the grid configuration is very similar to that for the linear model. $[\omega]$, $[T]^*$, ω' and T' are defined at 1000, 900, 800, ...100 mb, and $[u]$, $[v]$, $[\phi]^*$, u', v', ϕ' are defined at 950, 850, 750...50 mb. Derivatives with respect to y and p are approximated by centered differences, except near the boundaries, where one sided approximations to $\frac{\partial}{\partial y}$ and $\frac{\partial}{\partial p}$ are required for some terms. The jacobian is computed using the scheme developed by Arakawa (1966). This scheme ensures that the kinetic energy, $\frac{\partial[\chi]}{\partial p}^2 + \frac{\partial[\chi]}{\partial y}^2$, the x component of vorticity, $\frac{\partial^2[\chi]}{\partial y^2} + \frac{\partial^2[\chi]}{\partial p^2}$, and the mean square vorticity are all conserved up to terms which are second order in Δy and Δp.

The boundary conditions are similar to those applied in the linear model. $[\omega]$ and ω' vanish at the lower boundary. T' also vanishes at 1000 mb, and $[T]^*$ is held constant there. Values of $[\phi]^*$ and ϕ' at 950 mb are obtained from the conditions

$$\frac{\partial}{\partial t} \int_{p_{oo}}^{o} dp \, \frac{\partial[\omega]}{p} = 0$$

and

$$\frac{\partial}{\partial t} \int_{p_{oo}}^{o} dp \, \frac{\partial \omega'}{\partial p} = 0$$

Figure 6.2. Grid system for the nonlinear model.

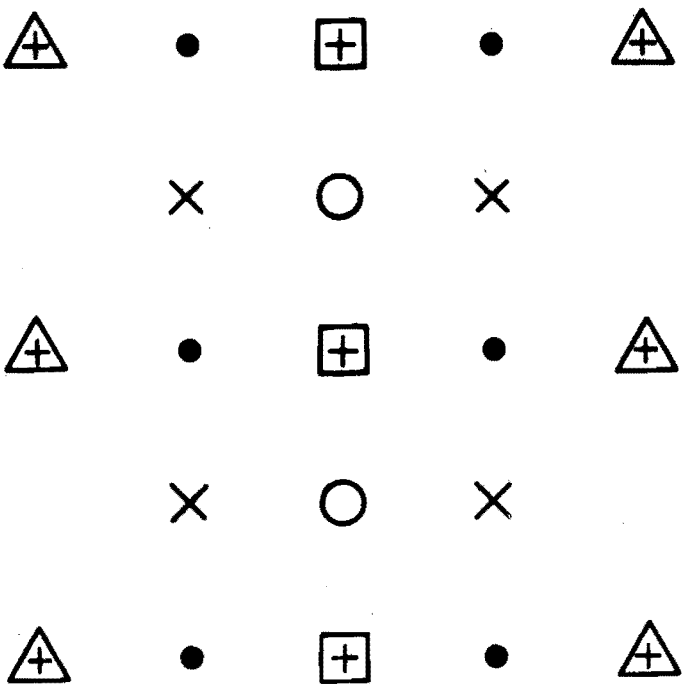

+ [u] , [v]

× $[T]^*$, $[\omega]$

• $[\phi]^*$

□ u', ϕ'

△ v'

○ T', ω'

respectively, to ensure $[\omega] = \omega' = 0$ at the top of the atmosphere. In order to simulate a radiation condition near the top of the atmosphere, a Rayleigh friction term is included in the perturbation momentum equations at the 50, 150 and 250 mb levels. The Rayliegh friction acts in the same manner as in the linear model, to absorb the energy which is reflected from the rigid lid imposed at the top of the atmosphere. As in the linear model, the lateral boundary conditions prohibit any flow of air into or out of the region. Thus, both [v] and v' are required to vanish at the equator and at 30°N.

The initial conditions for the nonlinear model are the same as those for the linear model. The zonally averaged flow is given by the [u] field shown in Figure 4.2. In order to evaluate [u] at the levels which are required for the model, the values of [u] defined on the grid system used for the linear model are interpolated linearly. [v] and $[\omega]$ both vanish. $[T]^*$ and $[\phi]^*$ are computed geostrophically from [u]. These fields are shown in Figure 4.3.

Comparison of Figures 4.3 and 2.2 shows that the field of $[T]^*$ used to initialize the model does not represent the observed temperature field too closely. Since Figure 4.3 assumes a jet intensity of 22.6 m sec^{-1}, the values of $[T]^*$ must be halved before they are compared to the observed values of $[T]^*$ in Figure 2.1. Clearly, the geostrophically determined temperature field does not closely approximate the observed field. The sign of $[T]^*$ agrees between the two fields, but the magnitude of the temperature deviations are quite different, particularly at low levels. According to observations, the largest values of $[T]^*$ occur at 850 mb, near 25°N. $[T]^*$ falls off rapidly at higher levels, but is nearly constant

between 850 mb and the surface. This results in almost no change in $[\theta]^*$ from 900 mb to 1000 mb, so that the heating/cooling rate is approximately zero. This is to be expected for a time averaged state. Near the equator, at low levels, the temperature deviations are negative, and their magnitudes are about two-thirds as large as those near 25°N. The geostrophic temperature deviations, on the other hand, are largest at 800 mb, and have very nearly equal magnitudes near the equator and over the Sahara Desert. The geostrophic surface temperatures at the surface are only about half as large as those at 800 mb. Because of this, the model produces considerable cooling over the desert. The magnitudes of the geostrophic temperatures are smaller than the observed temperatures by a factor of two or three. Because of these differences between the observed $[T]^*$ field and that used to initialize the model, the model cannot be expected to accurately simulate the thermal forcing over the desert. However, it is not practical to use an initial field of $[T]^*$ based more closely on the available temperature data. To do so would require the specification of a zonally averaged meridional flow. There is no data available to guide this specification. $[v]$ and $[\omega]$ would have to be determined solely by the requirement of balance between $[T]^*$ and $[u]$. Furthermore, the results of such a model could no longer be meaningfully compared to those of the linear model.

The initial perturbation fields are identical to those used in the linear model. T' is initialized to zero, and v' is given by a gaussian centered at 15°N and is vertically uniform. u' is computed from v' such that the perturbation is horizontally nondivergent. The solution is found by first advancing the perturbation variables one time step, and then advancing the zonally averaged variables.

2. Results of the Nonlinear Model

The nonlinear model becomes a linear model if the zonally averaged quantities are held constant, equal to their initial values, and α is set to zero. The perturbation variables after 4.6 days of integration of this model are shown in Figures 6.3 and 6.4. Ideally, these would be identical to Figures 5.22 and 5.23, obtained from the linear model. It is obvious from brief inspection of the two sets of figures that this is not the case. The principal differences between the results of the two models arise from two differences between the models. The large values of the perturbation wind fields at 350 mb in Figure 6.3 are due to a difference in the implementation of the radiation condition in the two models. In the five level model, the Rayleigh friction used to simulate the radiation condition extends down to the 300 mb level, effectively preventing reflections from the rigid upper boundary. In the ten level model, however, the dissipative term is included in the momentum equations only down to 250 mb. The model results indicate that this is insufficient to prevent reflections from the top of the atmosphere. That this is not a serious problem in the interpretation of the results can be seen from the fact that the reflections do not contaminate the flow field at low levels. Indeed, experiments with the five level model show that the results below 500 mb remain virtually unchanged as the coefficient of dissipation is varied from 0 to .4 day^{-1} at upper levels.

A potentially more serious discrepancy between the results of the two models is the overall growth rate of the disturbance. In the five level model, the growth rate of EKE is greater than .4 day^{-1}. However,

Figure 6.3. Results of the ten level linear model after 4.6 days.

u' contour interval = .3 m sec^{-1}

v' contour interval = .1 m sec^{-1}

ω' contour interval = .3 x 10^{-4} mb sec^{-1}

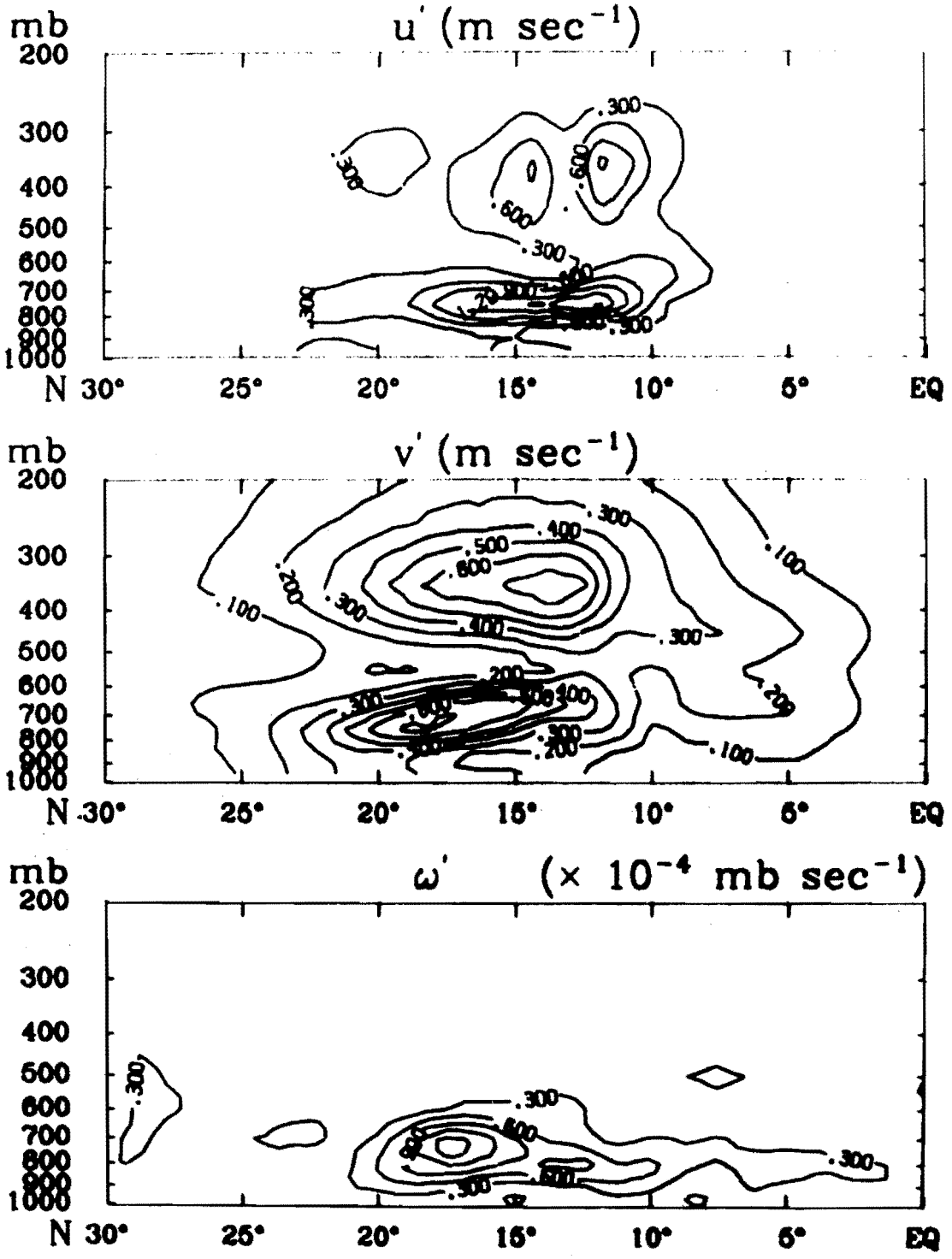
mb
u' (m sec⁻¹)
200
300
400
500
600
700
800
900
1000
N 30° 25° 20° 15° 10° 5° EQ
mb
v' (m sec⁻¹)
200
300
400
500
600
700
800
900
1000
N 30° 25° 20° 15° 10° 5° EQ
mb
ω' (× 10⁻⁴ mb sec⁻¹)
200
300
400
500
600
700
800
900
1000
N 30° 25° 20° 15° 10° 5° EQ

Figure 6.4. Results of ten level linear model after 4.6 days.

T' contour interval = .05 C

ϕ' contour interval = 2.0 $m^2 sec^{-2}$

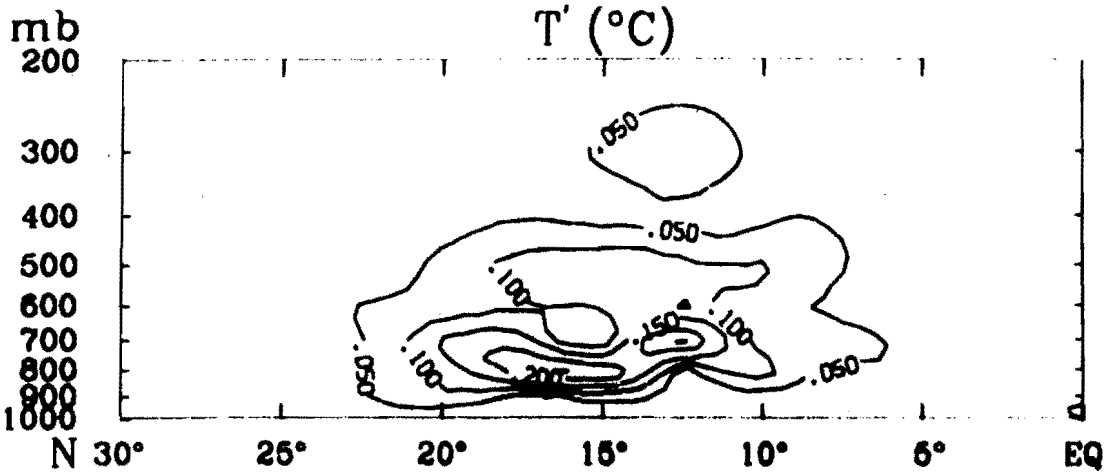
mb
T' (°C)
200
300
400
500
600
700
800
900
1000
.050
.050
.100
.150
.100
.100
.050
.200
.050
N 30°
25°
20°
15°
10°
5°
EQ

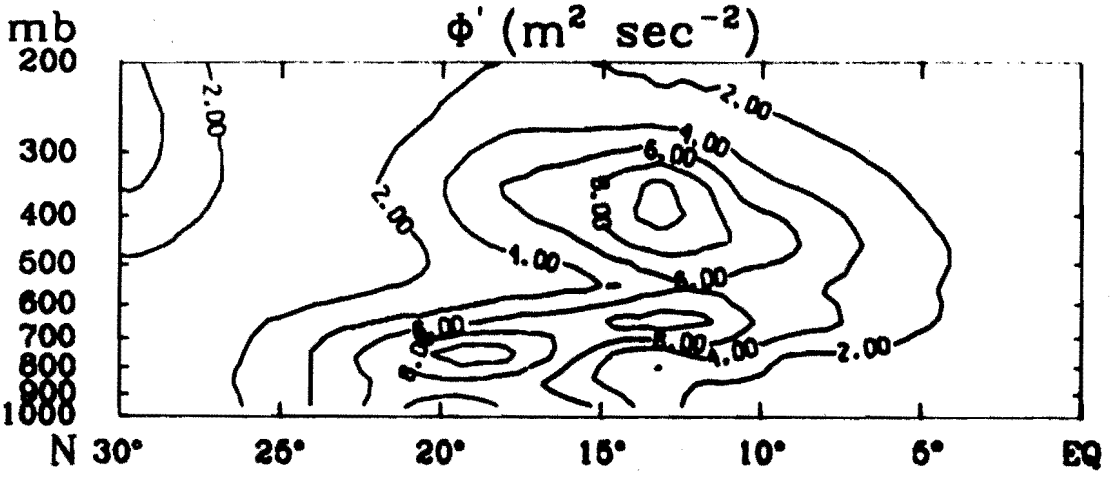
mb
Φ' (m² sec⁻²)
200
300
400
500
600
700
800
900
1000
2.00
2.00
4.00
6.00
8.00
2.00
1.00
4.00
2.00
2.00
N 30°
25°
20°
15°
10°
5°
EQ

in the ten level model, the maximum growth rate achieved by EKE is only .28 day^{-1}. This discrepancy is due to the difference in the vertical resolution of [u] in the two models. The results of the five level model show that the vertical transport of zonal momentum is an important instability mechanism. Consideration of the way in which $\frac{\partial[u]}{\partial p}$ is represented in the two models shows that the five level model is able to represent $\frac{\partial[u]}{\partial p}$ more accurately than can the ten level model. This is due to the fact that the five level model is a strictly linear model; $\frac{\partial[u]}{\partial p}$ is a constant parameter which is specified initially and remains unchanged. It need not be recomputed at each time step. Since [u] is known at 100 mb intervals, $\frac{\partial[u]}{\partial p}$ is computed over a 200 mb interval. For example, $\frac{\partial[u]}{\partial p}$ (700 mb) = $\frac{[u](800\text{ mb}) - [u](600\text{ mb})}{200\text{ mb}}$. This formulation implies that [u] varies linearly with pressure over the 200 mb interval from 800 mb to 600 mb. The ten level model still requires a 200 mb pressure interval over which to define $\frac{\partial[u]}{\partial p}$, since the quantity must be defined in terms of levels at which [u] is computed at each time step. Then, $\frac{\partial[u]}{\partial p}$ (650 mb) = $\frac{[u](750\text{ mb}) - [u](550\text{ mb})}{200\text{ mb}}$. But, since the initial values of [u](750 mb) and [u](650 mb) are themselves obtained by interpolating between levels of [u], this quantity may be expressed (initially) as

$$\frac{\partial[u]}{\partial p}(650\text{ mb}) = \frac{[u](800\text{ mb}) + [u](700\text{ mb}) - [u](600\text{ mb}) - [u](500\text{ mb})}{400\text{ mb}}$$

This procedure introduces considerable smoothing into $\frac{\partial[u]}{\partial p}$, so that values of $\frac{\partial[u]}{\partial p}$ in the center of the jet used by the ten level model are reduced by a factor of two from their values in the five level model. Because

data is not available at intermediate pressure levels, there is no simple way to avoid this difficulty. Therefore, the ten level model must tend to underestimate the growth of the waves. Results of the nonlinear model must be compared to Figures 6.3 and 6.4 rather than to the results of the five level linear model.

The influence of the waves on the zonally averaged flow in the absence of surface heating was investigated by setting K_H, the eddy coefficient for vertical heat transport in the lowest layer of the atmosphere, to zero, and allowing the waves to feed back onto the mean state. The coefficient parameterizing wave-wave interaction, α, was also set to zero so that no energy could be dissipated to higher wavenumbers. In this way, the effect of the waves on the mean state is maximized.

The results of this model are shown in Figures 6.5 - 6.9. Comparison of Figures 4.2 and 6.5 show that after 4.6 days, the waves have made no significant modifications of the zonal wind field. The position of the jet maximum is unchanged and its magnitude has been reduced by only 4 cm sec^{-1}. Even the second derivative of the zonal wind field, $\frac{\partial^2[u]}{\partial y^2}$, which is very sensitive to small changes in [u], is virtually unchanged by the nonlinear interaction. The meridional circulation is shown in Figure 6.5. The circulation generated by the waves is much too small to be significant. The maximum value of [v] is less than 1.6 cm sec^{-1}, whereas the meridional perturbation has a magnitude of over .5 m sec^{-1}. Likewise, the zonally averaged vertical velocity is an order of magnitude smaller than the perturbation vertical velocity. The maximum value of $[\omega]$ is less than 1×10^{-5} mb sec^{-1}, while ω' exceeds 1×10^{-4} mb sec^{-1}.

Figure 6.5. Results of nonlinear model after 4.6 days with $\alpha = 0$, $K_H = 0.$

[u] contour interval = 6.0 m sec^{-1}

$\frac{\partial^2[u]}{\partial y^2}$ contour interval = .8 x 10^{-10} $m^{-1}sec^{-1}$

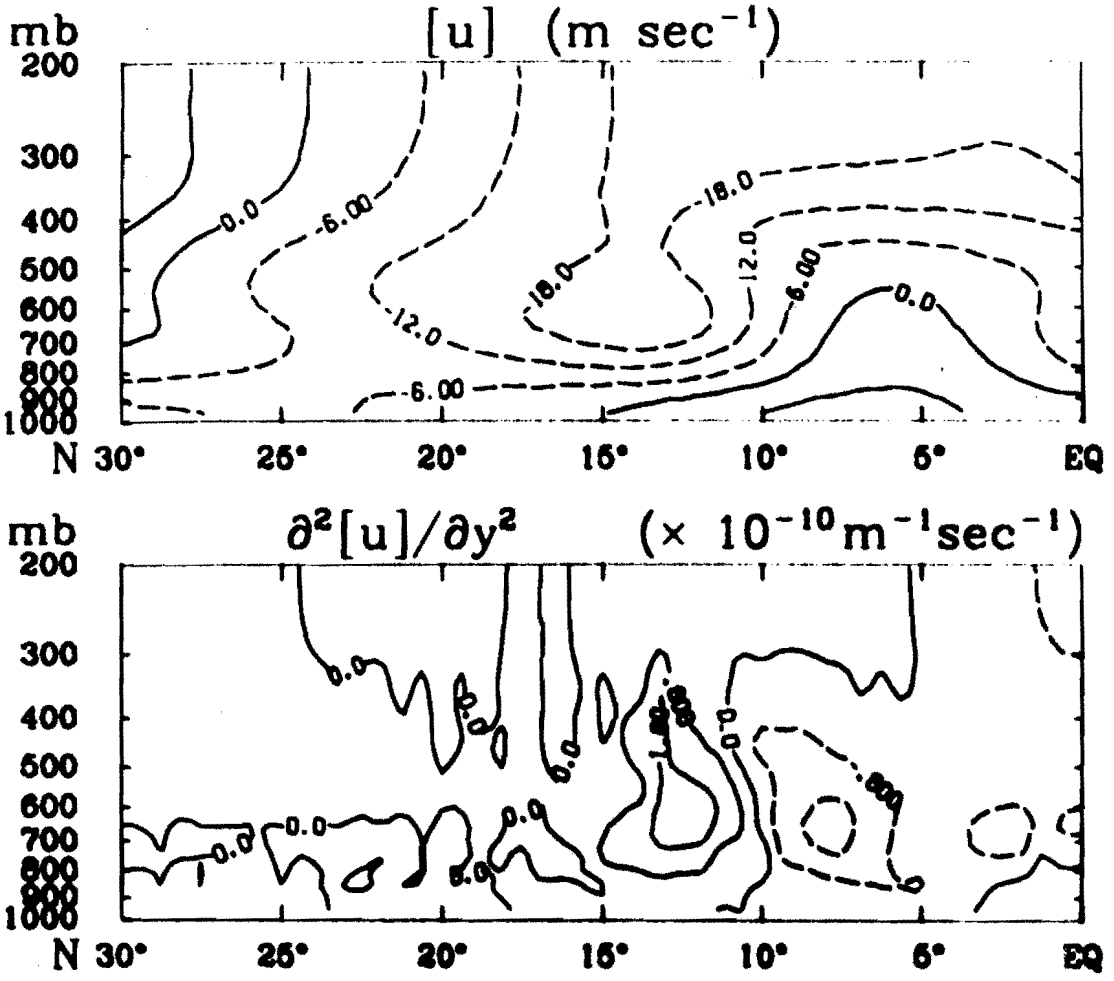
mb
[u] (m sec⁻¹)
200
300
400
500
600
700
800
900
1000
0.0
-6.00
-12.0
-18.0
N 30°
25°
20°
15°
10°
5°
EQ
mb
∂²[u]/∂y² (× 10⁻¹⁰m⁻¹sec⁻¹)
200
300
400
500
600
700
800
900
1000
0.0
N 30°
25°
20°
15°
10°
5°
EQ

Figure 6.6. Results of nonlinear model after 4.6 days with $\alpha = 0$, $K_H = 0$.

[v] contour interval = .6 cm sec^{-1}

[ω] contour interval = .3 x 10^{-6} mb sec^{-1}

[χ] contour interval = 50 mb m sec^{-1}

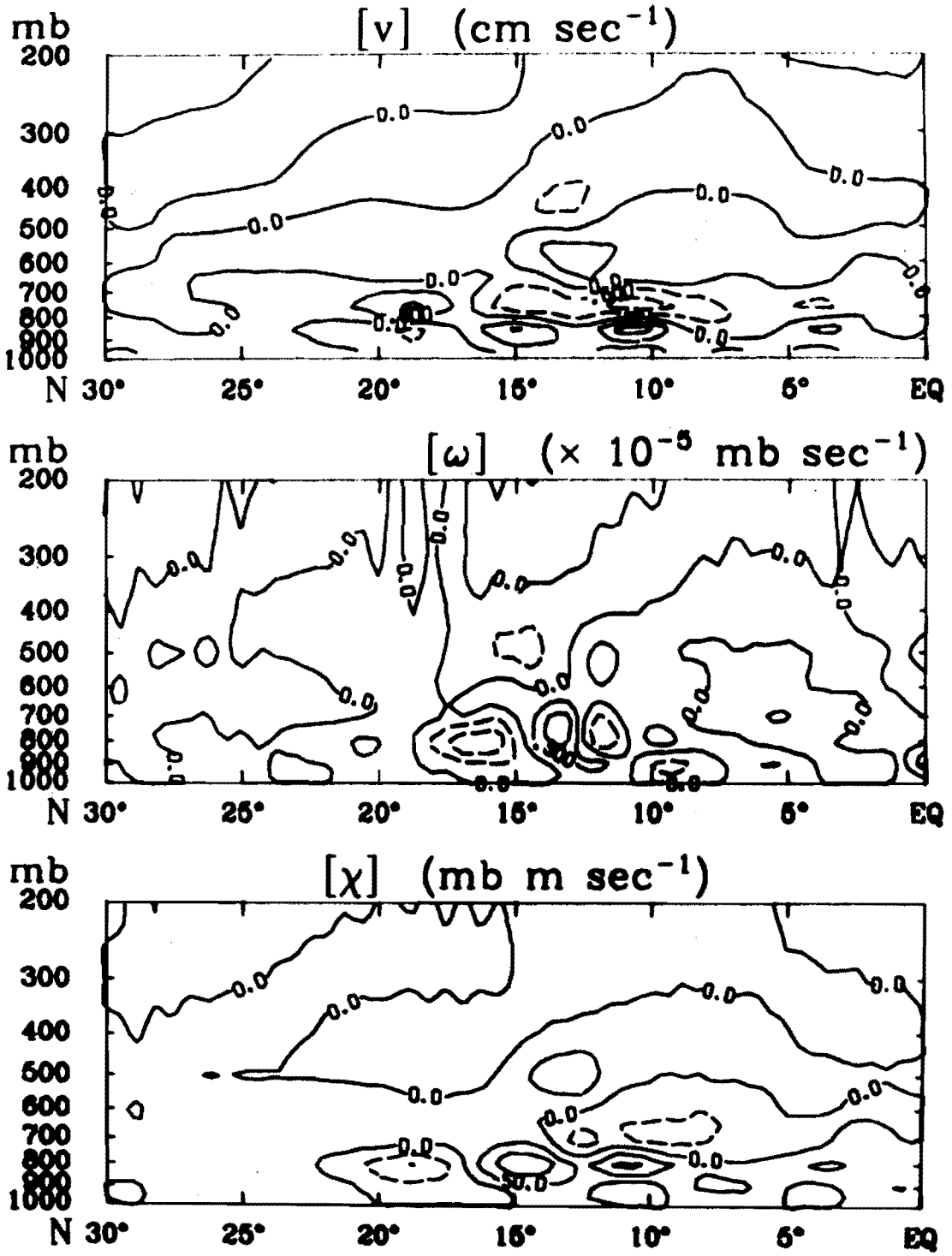
[v] (cm sec⁻¹)
mb
200
300
400
500
600
700
800
900
1000
N 30° 25° 20° 15° 10° 5° EQ
[ω] (× 10⁻⁵ mb sec⁻¹)
mb
200
300
400
500
600
700
800
900
1000
N 30° 25° 20° 15° 10° 5° EQ
[χ] (mb m sec⁻¹)
mb
200
300
400
500
600
700
800
900
1000
N 30° 25° 20° 15° 10° 5° EQ

Furthermore, the zonally averaged meridional circulation exhibits virtually no organization, indicating that it represents little more than computational noise. Figure 6.7 shows that the zonally averaged temperature and geopotential fields, like the zonal wind field, are unaffected by the inclusion of nonlinearities in the model. The perturbation fields after 4.6 days are shown in Figures 6.8 and 6.9. These fields are nearly identical to those shown in Figures 6.3 and 6.4 for the ten level linear model. This is to be expected, since there is no additional sink of energy when α is set to zero, and the source of wave energy, the shear of the zonal flow, is unchanged by the nonlinear effects.

When dissipation of energy due to wave-wave interaction is included in the model, there is no significant effect on the zonally averaged quantities. The only consequence of setting $\alpha = .1$ day^{-1} is a reduction in the magnitude of the perturbation variables.

The effect of surface heating on the zonally averaged flow was investigated in the absence of waves by initializing all the perturbations to zero, and setting $K_H = 1.027 \times 10^{-3}$ mb sec^{-1}. This corresponds to a time scale of about one day, so it represents a fairly large effect. But the effects of heating on the flow field are negligible. Figure 6.10 shows the response of $[u]$ and $\frac{\partial^2[u]}{\partial y^2}$ to the heating after 4.6 days. The fields are virtually identical to the initial fields. The meridional circulation induced by the heating is negligible, as seen in Figure 6.11. Maximum values of $[v]$ are about 15 cm sec^{-1}, and $[\omega]$ attains magnitudes

Figure 6.7. Results of nonlinear model after 4.6 days with $\alpha = 0$, $K_H = 0$.
$[T]^*$ contour interval = 2 C
$[\phi]^*$ contour interval = 200 m^2 sec^{-2}

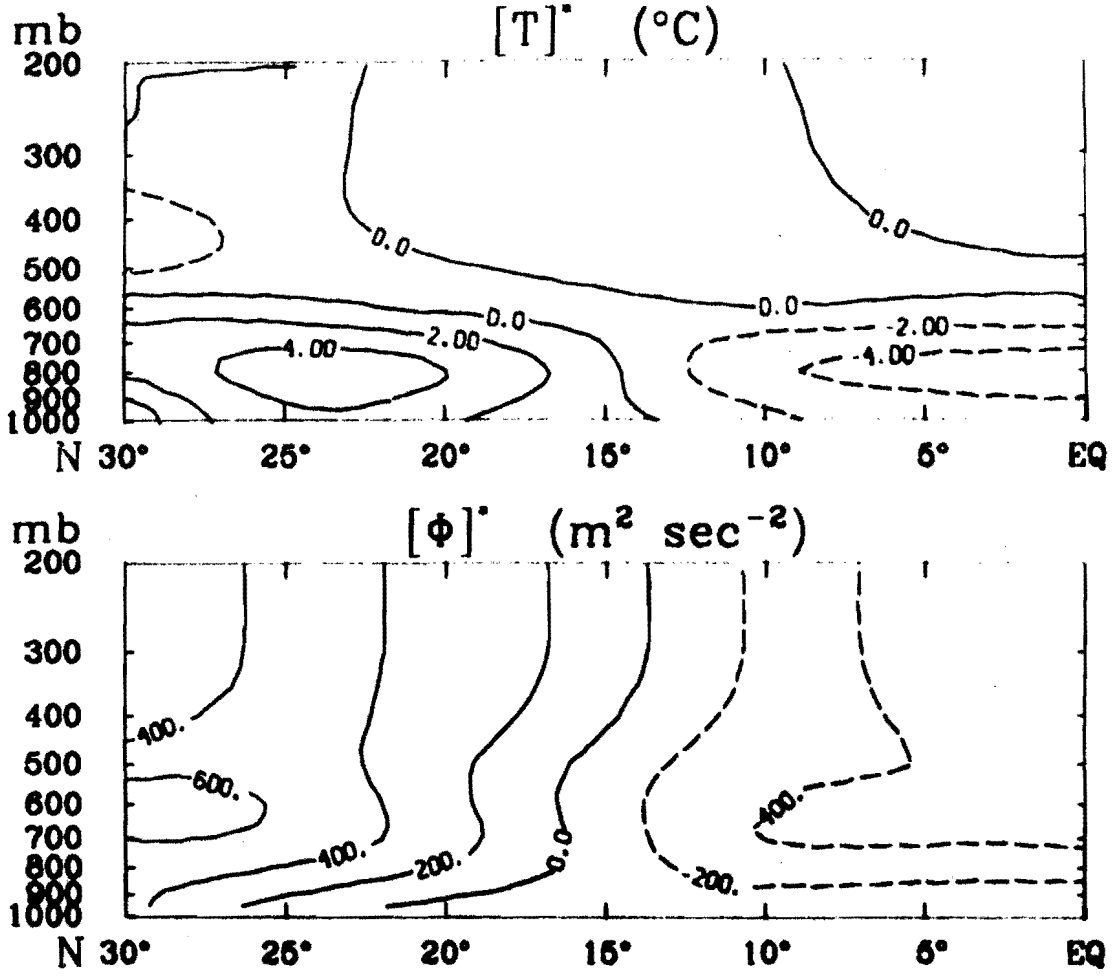
[T]* (°C)
mb
200
300
400
500
600
700
800
900
1000
0.0
0.0
0.0
-2.00
-4.00
4.00
2.00
N 30° 25° 20° 15° 10° 5° EQ
[Φ]* (m² sec⁻²)
mb
200
300
400
500
600
700
800
900
1000
400.
600.
400.
200.
0.0
400.
-200.
N 30° 25° 20° 15° 10° 5° EQ

Figure 6.8. Results of nonlinear model after 4.6 days with $\alpha = 0$, $K_H = 0$.

u' contour interval = .3 m sec^{-1}

v' contour interval = .1 m sec^{-1}

ω' contour interval = .3 x 10^{-4} mb sec^{-1}

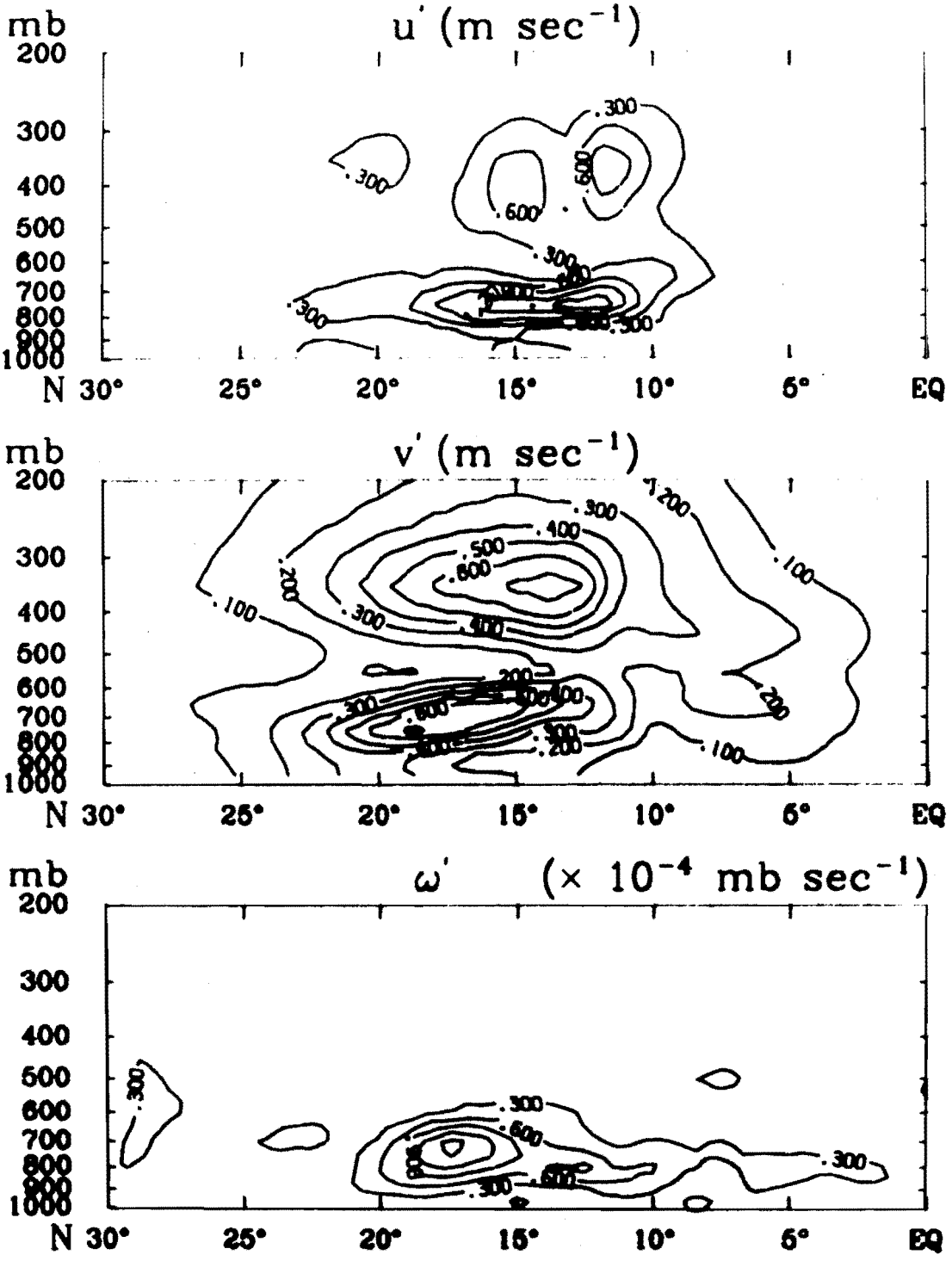
mb
u' (m sec⁻¹)
200
300
400
500
600
700
800
900
1000
N 30° 25° 20° 15° 10° 5° EQ
mb
v' (m sec⁻¹)
200
300
400
500
600
700
800
900
1000
N 30° 25° 20° 15° 10° 5° EQ
mb
ω' (× 10⁻⁴ mb sec⁻¹)
200
300
400
500
600
700
800
900
1000
N 30° 25° 20° 15° 10° 5° EQ

Figure 6.9. Results of nonlinear model after 4.6 days with $\alpha = 0$, $K_H = 0.$

T' contour interval = .056

ϕ' contour interval = 2.0 m^2 sec^{-2}

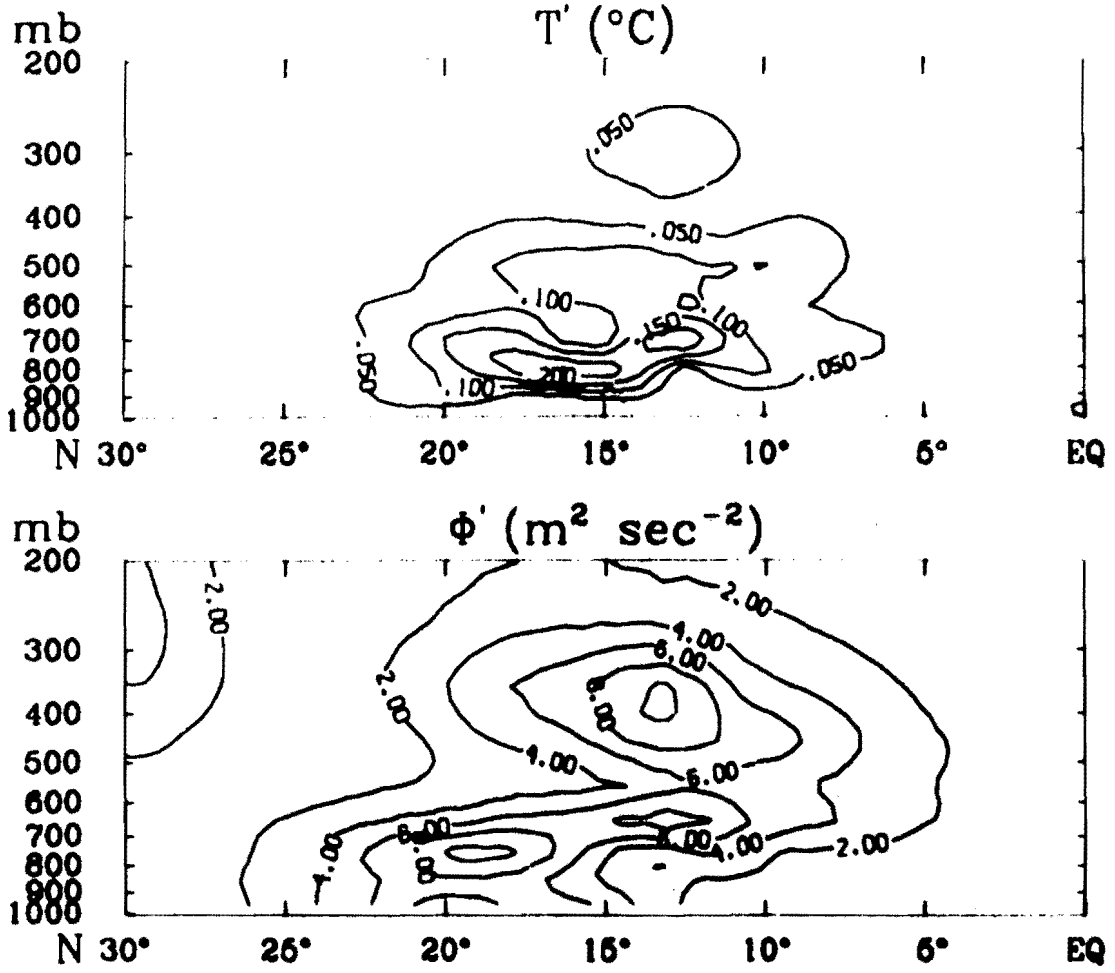
mb
T' (°C)
200
300
400
500
600
700
800
900
1000
.050
.050
.100
.150
.100
.050
.100
.050
N 30°
25°
20°
15°
10°
6°
EQ
mb
Φ' (m² sec⁻²)
200
300
400
500
600
700
800
900
1000
-2.00
2.00
4.00
6.00
8.00
-2.00
-4.00
-6.00
-8.00
N 30°
25°
20°
15°
10°
6°
EQ

Figure 6.10. Results of nonlinear model after 4.6 days with no waves, and $K_H = 1.027 \times 10^{-3}$ mb sec^{-1}.

[u] contour interval = 6.0 m sec^{-1}

$\frac{\partial^2[u]}{dy^2}$ contour interval = $.9 \times 10^{-10}$ m^{-1} sec^{-1}

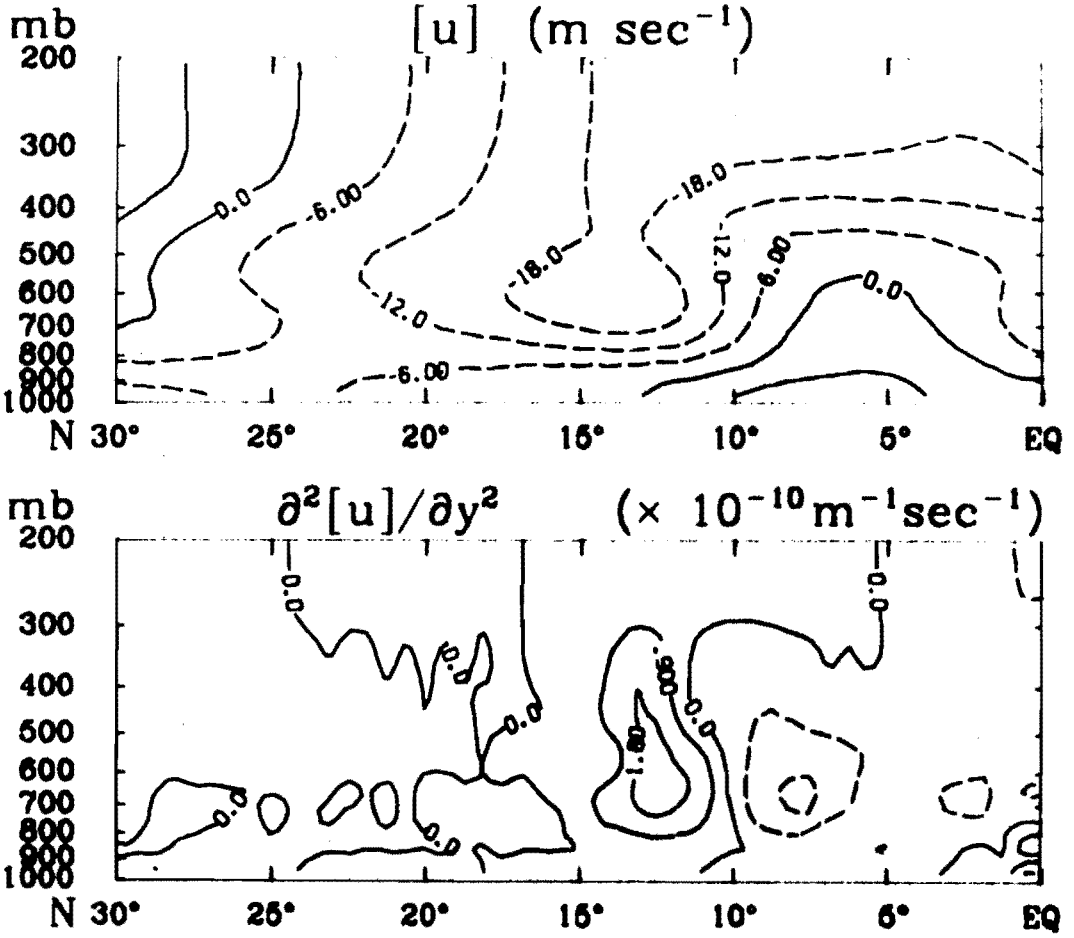
mb
[u] (m sec⁻¹)
200
300
400
500
600
700
800
900
1000
0.0
-6.00
-12.0
-18.0
-18.0
-12.0
-6.00
0.0
-6.00
N 30° 25° 20° 15° 10° 5° EQ
mb
∂²[u]/∂y² (× 10⁻¹⁰m⁻¹sec⁻¹)
200
300
400
500
600
700
800
900
1000
0.0
0.0
0.0
0.0
0.0
0.0
0.0
0.0
N 30° 25° 20° 15° 10° 5° EQ

Figure 6.11. Results of nonlinear model after 4.6 days with no waves, $K_H = 1.027 \times 10^{-3}$ mb sec^{-1}.

[v] contour interval = 6.0 cm sec^{-1}

[ω] contour interval = 5×10^{-5} mb sec^{-1}

[χ] contour interval = 300 mb m sec^{-1}

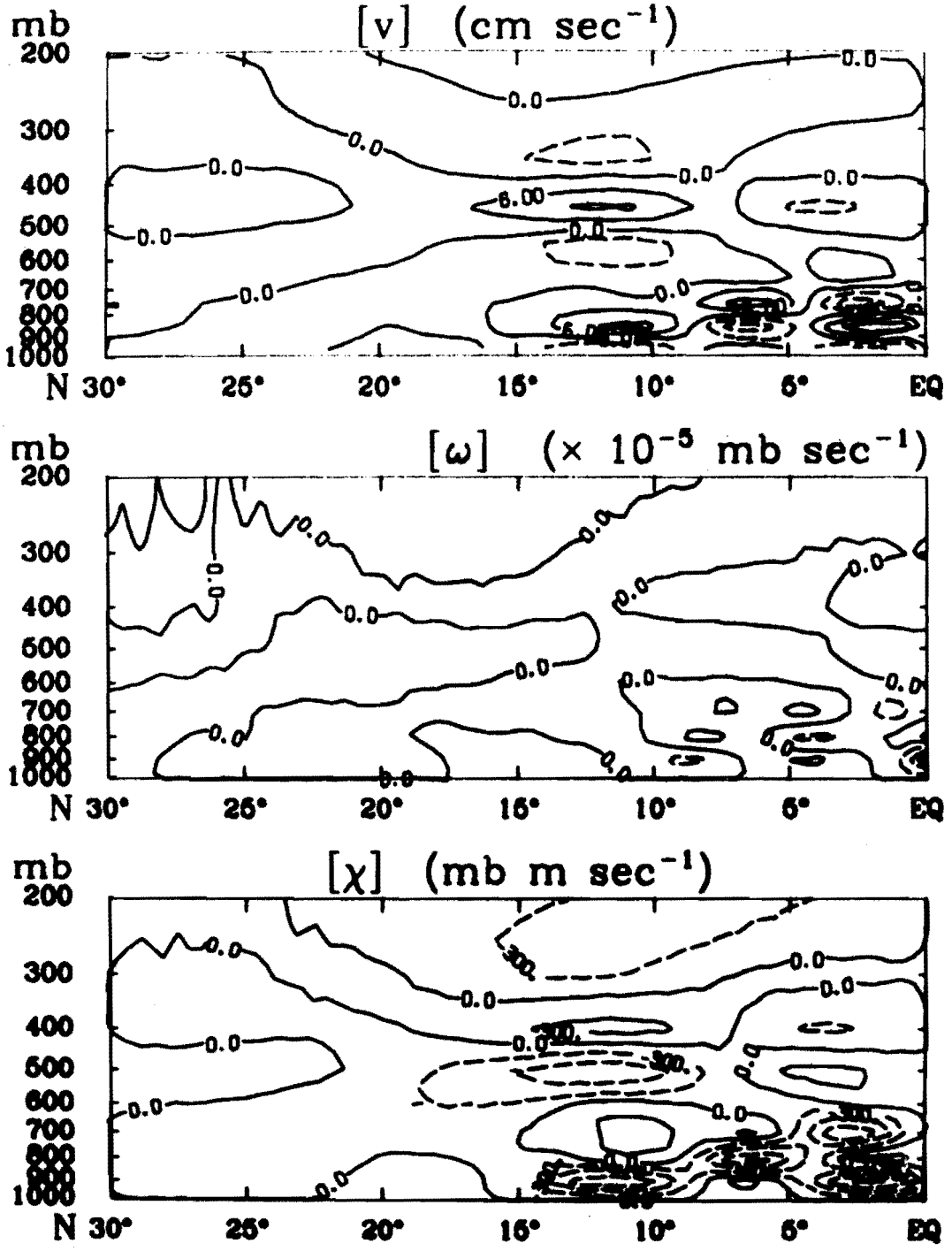
[v] (cm sec⁻¹)
mb
200
300
400
500
600
700
800
900
1000
N 30° 25° 20° 15° 10° 5° EQ
[ω] (× 10⁻⁵ mb sec⁻¹)
mb
200
300
400
500
600
700
800
900
1000
N 30° 25° 20° 15° 10° 5° EQ
[χ] (mb m sec⁻¹)
mb
200
300
400
500
600
700
800
900
1000
N 30° 25° 20° 15° 10° 5° EQ

Figure 6.12. Results of nonlinear model after 4.6 days with no waves, and $K_H = 1.027 \times 10^{-3}$ mc sec^{-1}.
$[T]^*$ contour interval = 2.0 C
$[\phi]^*$ contour interval = 200 m^2 sec^{-2}

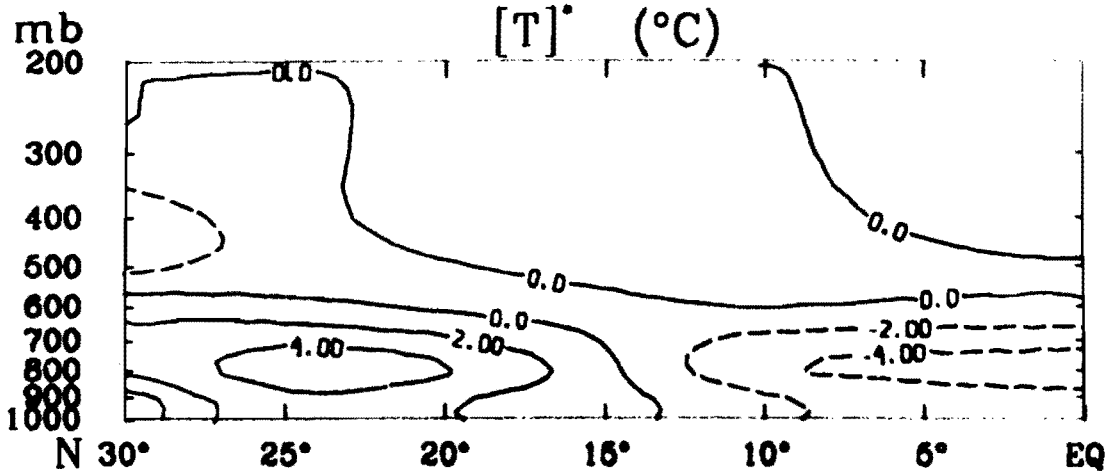
mb
[T]* (°C)
200
300
400
500
600
700
800
900
1000
0.0
0.0
0.0
0.0
0.0
-2.00
-4.00
4.00
2.00
N 30°
25°
20°
15°
10°
5°
EQ

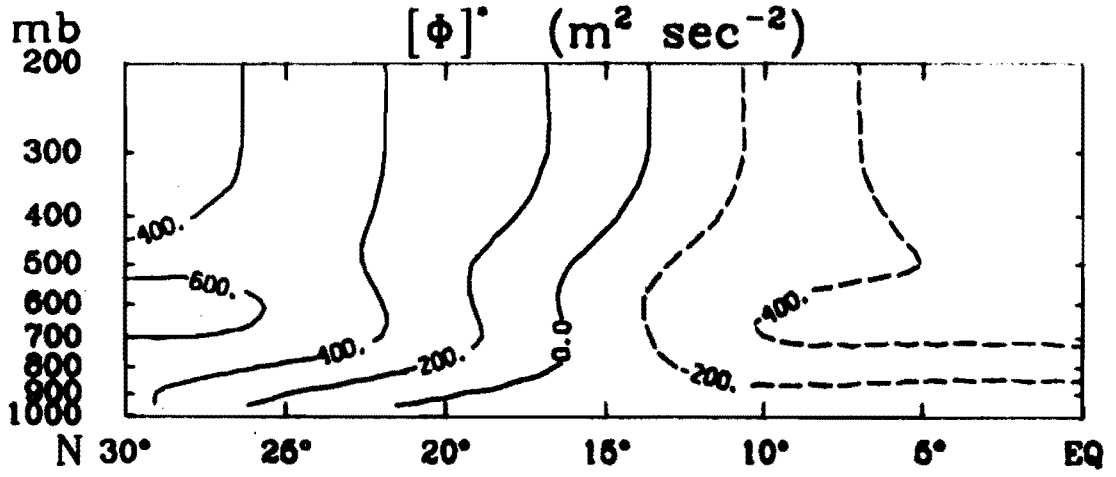
mb
[Φ]* (m² sec⁻²)
200
300
400
500
600
700
800
900
1000
400.
600.
400.
200.
0.0
400.
200.
N 30°
25°
20°
15°
10°
5°
EQ

somewhat greater than 5×10^{-5} mb sec^{-1}. Although these values are somewhat larger than those associated with the case of wave interaction with the basic flow in the absence of heating, they are still small, and quite disorganized. A slight adjustment in the temperature field at 900 mb may be seen in Figure 6.12. There is heating between the equator and 10°N, and cooling between 20°N and 30°N in response to the imposed surface temperature. This is not the heating field which would be expected over the desert, but it is consistent with the geostrophic distribution of temperature. The maximum temperature change is about .8C. The effect of the surface heating does not penetrate to higher levels. At 800 mb, the maximum temperature change is only .04C. The geopotential field is unaffected by the small change in 900 mb temperatures.

The results of the nonlinear model indicate that the waves do not deplete the energy of the jet on a 5 day time scale. Not only is the basic zonal flow, [u], unaffected by the nonlinear interactions with the waves, but the important stability characteristic, $\frac{\partial^2[u]}{\partial y^2}$ is also unchanged. Because of the problems involved with the vertical resolution of the basic state, the waves produced by the nonlinear model have smaller amplitudes than would be expected based on the linear model results. This tends to weaken the nonlinear interaction, so that the model probably underestimates their effect. However, even if the magnitude of the waves were doubled, it is not likely that the zonally averaged flow field would be appreciably stabilized by the waves over a 5 day time period.

The model results show that the geostrophically determined temperature field does not generate an organized meridional circulation in response to surface heating. Indeed, it does not lead to the type of heating field which would be expected over the desert region. This is due to discrepancies between the geostrophic temperature field and the actual temperature field. These differences between the observed values of $[T]^*$ and those determined geostrophically from the zonal wind field, coupled with the failure of the geostrophic temperature field to generate an organized meridional circulation in the nonlinear model, imply that the dynamics of the maintenance of the jet cannot be studied in the context of deviations about a geostrophic steady state.

Since the model has no knowledge of the value of $\frac{\partial [u]}{\partial p}$ at 1000 mb, there is no reason why the temperature field there must be determined by geostrophy. Presumably, the surface temperatures could be specified by the data field, even though the upper level temperatures were not. This could then yield a more realistic heating field. However, this is not the case. The observed temperatures over the desert are so much warmer than the geostrophic temperatures there, that $[\theta]^*$ increases sharply from 900 mb to 1000 mb when observed values of $[T]^*$ are used at the surface, and geostrophic values are used at 900 mb. The increase is so great that $\frac{\partial [T]^*}{\partial p} - \frac{\kappa [T]^*}{p}$ has a larger magnitude than does σ, and the overall lapse rate of temperature at 900 mb is super adiabatic. This results in strong convection, and invalidates the assumption of hydrostasis. Attempts to use such a temperature field in the model were thwarted by the onset of computational instability after about two days of integration.

In order to use a simple numerical model to study the way in which the zonally averaged flow responds to surface heating, it is necessary to allow the basic state to include an ageostrophic component. This requires non-vanishing initial fields of $[v]$ and $[\omega]$, so that $[T]^*$ may depart from geostrophic balance with $[u]$. Since $[v]$ and $[\omega]$ are small, of the same order of magnitude as v' and ω', such a system is not amenable to treatment by linear analysis.

VII. CONCLUSION

The characteristics of African waves have been fairly well documented over the past several years. However, the mechanism by which the waves are generated is not clear. The main purpose of this work was to determine whether or not the shear of the mean zonal flow is such that the waves may be initiated as instabilities on that flow. The nature of the instability was also of interest. The study was to determine which features of the flow are responsible for the generation of the waves, and through what physical mechanisms they act.

The fluid dynamical equations which govern the physical system do not lend themselves to analytic solution, even in their simplified, linear form. Therefore, the system was modeled numerically.

The results of the model show that the observed mean zonal flow over Africa can indeed support instabilities on the scale of African waves. The source of the wave energy is the kinetic energy of the zonal flow. Energy is transferred from the zonal flow to the waves as easterly momentum is transferred away from the easterly jet by the horizontal and vertical Reynolds stresses. When the vertical transport is constrained to be zero, energy is still transferred from the zonal flow to the waves by horizontal momentum transport. Although this significantly changes the distribution of energy transport in the atmosphere, the waves so generated display many of the same characteristics as to those generated in the more general case. If,however, the horizontal momentum transport is constrained to be zero, the vertical transport of momentum does not act to support an instability

of any kind. Neither quasi-geostrophic baroclinic energy conversion, nor the release of latent heat is important in the generation of the waves.

The interaction between the waves and the mean flow is sufficiently small so that the instability characteristics of the zonal flow remain virtually unchanged after interacting with the wave for about 5 days. In order to investigate the interaction in more detail, a model would need to allow the existence of an ageostropic zonally averaged flow, even in the initial state. The boundary conditions would also have to be changed. The assumption of periodic boundary conditions in the direction of propagation would have to be dropped, in order that the model could be allowed to simulate the interaction between the waves and the basic flow over a longer time span. The lateral boundary conditions could also be altered to allow the inflow of cool moist air at low levels due to the monsoon circulation.

REFERENCES

Arakawa, A. (1966) Computational design for long-term numerical integration of the equations of fluid motion: two-dimensional incompressible flow. Part 1. Jour. Comp. Phys. 1, pps. 119-143.

Arnold, J. E. (1966) Easterly wave activity over Africa and in the Atlantic with a note on the Intertropical Convergence Zone during July, 1961. Satellite and Mesometeorology Research Project, Report #65. Department of Geophysical Science, The University of Chicago.

Aspliden, C. I. (1974) The low level wind field and associated perturbations over tropical Africa during northern summer. Preprints--International Tropical Meteorology Meeting. American Meteorological Society, Boston.

Burpee, R. W. (1972) The origin and structure of easterly waves in the lower troposphere of North Africa. Jour. Atmos. Sci. 29, pp. 77-90.

Burpee, R. W. (1974) Characteristics of North African easterly waves during the summers of 1968 and 1969. Jour. Atmos. Sci. 31, pp. 1556-1570.

Burpee, R. W. (1975) A summary of weather systems affecting western Africa and the eastern Atlantic during GATE. Final Report, International Scientific and Management Group for GATE.

Carlson, T. N. (1969a) Synoptic histories of three African disturbances that developed into Atlantic hurricanes. Monthly Weather Rev. 97, pp. 256-277.

Carlson, T. N. (1969b) Some remarks on African disturbances and their progress over the tropical Atlantic. Monthly Weather Rev. 97, pp. 716-726.

Carlson, T. N. (1971) A detailed analysis of some African disturbances. NOAA Technical Memorandum ERL NHRL-90.

Charney, J. G. (1947) The dynamics of long waves in a baroclinic westerly current. Jour. Meteorology 4, pp. 135-162.

Charney, J. G. (1963) A note on large-scale motions in the tropics. Jour. Atmos. Sci. 20, pp. 607-609.

Charney, J. G. (1973) Planetary fluid dynamics, in P. Morel, ed., Dynamic Meteorology, D. Reidel Publ. Co. Boston, pp. 97-352.

Charney, J. G. and Stern, M. E. (1962) On the stability of internal baroclinic jets in a rotating atmosphere. Jour. Atmos. Sci. 19, pp. 159-172.

Courant, R., Friedrichs, K. O., Lewy, H. (1928) Über die partiellen Differenzengleichungen der mathematischen Physik. Math. Ann. 100, p. 32.

Dean, G. A. and La Seur, N. E. (1974) The mean structure and its synoptic-scale variation of the African troposphere. Preprints --International Tropical Meteorology Meeting. American Meteorological Society, Boston.

Drazin, P. G. and Howard, L. N. (1966) Hydrodynamic stability of parallel flow of inviscid fluid. Advances in Applied Mechanics 9, pp. 214-224.

Eady, E. T. (1949) Long waves and cyclone waves. Tellus 1, pp. 33-52.

Eldridge, R. H. (1957) A synoptic study of West African disturbance lines. Quart. Jour. Royal Met. Soc. 83, pp. 303-314.

Frank, N. L. (1969) The "inverted V" cloud pattern--an easterly wave? Monthly Weather Rev. 97, pp. 130-140.

Frank, N. L. (1970) Energetics of cold lows. Proc. Symposium on Tropical Meteorology, American Meteorological Society, p. E IV.

Holton, J. R. (1972) An Introduction to Dynamic Meteorology. Academic Press, New York.

Holton, J. R. and Colton, D. E. (1972) A diagnostic study of the vorticity balance at 200 mb in the tropics during the northern summer. Jour. Atmos. Sci. 29, pp. 1124-1128.

Kuo, H. L. (1949) Dynamic instability of two-dimensional nondivergent flow in a barotropic atmosphere. Jour. Meteorology 6, pp. 105-122.

Kuo, H. L. (1952) Three dimensional disturbances in a baroclinic zonal current. Jour. Meteorology 9, pp. 260-278.

Kuo, H. L. (1973) Dynamics of quasi-geostrophic flows and instability theory. Advances in Applied Mechanics 13, pp. 248-330.

Lilly, D. K. (1965) On the computational stability of numerical solutions of time-dependent non-linear geophysical fluid dynamics problems. Monthly Weather Rev. 93, pp. 11-26.

Lin, C. C. (1955) The Theory of Hydrodynamic Stability. Cambridge University Press, Cambridge.

Lorenz, E. N. (1955) Available potential energy and the maintenance of the general circulation. Tellus 7, pp. 157-167.

Lorenz, E. N. (1963) Deterministic nonperiodic flow. Jour. Atmos. Sci. 20, pp. 130-141.

Newell, R. E., Kidson, J. W., Vincent, D. G., Boer, G. J. (1972) The General Circulation of the Tropical Atmosphere and Interactions with Extra-tropical Latitudes, Vol. 1. MIT Press, Boston.

Nitta, T. and Yanai, M. (1969) A note on the barotropic instability of the tropical easterly current. Jour. Met. Soc. Japan 47, pp. 127-130.

Okulaja, F. O. (1970) Synoptic flow perturbations over West Africa. Tellus 22, pp. 663-680.

Orlanski, I. (1968) Instability of frontal waves. Jour. Atmos. Sci. 25, pp. 178-200.

Pedlosky, J. (1964a) The stability of currents in the atmosphere and the oceans: Part I. Jour. Atmos. Sci. 21, pp. 201-219.

Pedlosky, J. (1964b) The stability of currents in the atmosphere and the oceans: Part II. Jour. Atmos. Sci. 21, pp. 342-353.

Pedlosky, J. (1965) On the stability of baroclinic flows as a function of the velocity profile. Jour. Atmos. Sci. 22, pp. 137-145.

Phillips, N. A. (1964) An overlooked aspect of the baroclinic stability problem. Tellus 16, pp. 268-270.

Rayleigh, Lord (1879) On the instability of jets. Scientific Papers Vol. 1, Art. 58, pp. 361-371.

Rayleigh, Lord (1880) On the stability, or instability, of certain fluid motions. Scientific Papers Vol. 1, Art. 66, pp. 474-487.

Reed, R. J. and Recker, E. E. (1971) Structure and properties of synoptic-scale wave disturbances in the equatorial western Pacific. Jour. Atmos. Sci. 28, pp. 1117-1131.

Reiter, E. R. (1963) Jet-stream Meteorology, University of Chicago Press, Chicago.

Squire, H. B. (1933) On the stability of three-dimensional disturbances of viscous flow between parallel walls. Proc. Royal Soc. A 142, pp. 621-628.

APPENDIX

THE QUASI-GEOSTROPHIC APPROXIMATION

Although the time dependent motions of the atmosphere are not strictly geostrophic, they may be treated as small departures from geostrophic motions for a broad class of conditions. A very useful theory has been developed which uses scaling arguments to simplify the equations of motion and describes the tendency of atmospheric motions to restore geostrophic balance.

This quasi-geostrophic theory makes several assumptions about the motions it describes. It assumes that the horizontal length scale of the motions is much greater than their vertical length scale. The advective acceleration is assumed to be small compared to the Coriolis acceleration, and the time scale for the motions is assumed to be given by the time scale for horizontal advection. These assumptions are valid for motions on the scale of several thousand kilometers at mid latitudes, but the theory has been used with some success in tropical regions, down to about 10°N.

An equation governing the vertical component of the vorticity, ζ, may be obtained from the primitive equations by forming $\frac{\partial}{\partial x}$ (3.2) - $\frac{\partial}{\partial y}$ (3.1).

$$\frac{\partial \zeta}{\partial t} + \vec{v} \cdot \vec{\nabla} (\zeta+f) + \omega \frac{\partial \zeta}{\partial p} + (\zeta+f) \vec{\nabla} \cdot \vec{v} + \frac{\partial \omega}{\partial x} \frac{\partial v}{\partial p} - \frac{\partial \omega}{\partial y} \frac{\partial u}{\partial p} = 0 \qquad (1)$$

The relative importance of the various terms of (1) may be estimated by considering typical magnitudes of mid latitude motions. Horizontal

velocities are scaled by $U \sim 10$ m sec^{-1}, and vertical velocity by $W \sim 10^{-3}$ mb sec^{-1}. The horizontal length scale is $L \sim 10^{6}$ m. Then $\zeta \sim \frac{U}{L} \sim 10^{-5}$ sec^{-1}. Motions are assumed to take place over the entire depth of the atmosphere, so that $P \sim 10^{3}$ mb. The time scale is given by the advective time scale, $\frac{L}{U} \sim 10^{5}$ sec. The Coriolis parameter is replaced by its value near 45°N, $f_o = 10^{-4}$ sec^{-1}. The variation of f with respect to y is likewise given by its 45°N value, $\beta = 10^{-11}$ m sec^{-1}.

With this scaling, the magnitudes of the terms in (1) may be estimated. Since the last two terms of (1) involve differences of nearly equal quantities, only upper bounds can be estimated for these terms. They may actually take on significantly smaller values than those derived from simple scaling.

$$\frac{\partial \zeta}{\partial t} \sim \frac{U^2}{L^2} \sim 10^{-10} \text{ sec}^{-2}$$

$$\vec{V} \cdot \vec{\nabla}\zeta \sim \frac{U^2}{L^2} \sim 10^{-10} \text{ sec}^{-2}$$

$$\vec{V} \cdot \vec{\nabla} f \sim U\beta \sim 10^{-10} \text{ sec}^{-2}$$

$$\omega \frac{\partial \zeta}{\partial p} \sim \frac{WU}{LP} \sim 10^{-11} \text{ sec}^{-2}$$

$$(\zeta + f)\ \vec{\nabla} \cdot \vec{V} \sim \frac{f_o U}{L} \sim 10^{-9} \text{ sec}^{-2}$$

$$\frac{\partial \omega}{\partial x}\frac{\partial v}{\partial p} - \frac{\partial \omega}{\partial y}\frac{\partial u}{\partial p} \sim \frac{WU}{LP} \sim 10^{-11} \text{ sec}^{-2}$$

This analysis shows that the horizontal divergence must indeed be less than $\frac{U}{L}$. Indeed, $\vec{\nabla}\cdot\vec{V}$ must be no greater than 10^{-6} sec^{-1}. Otherwise,

the divergence term, $(\zeta+f)\vec{\nabla}\cdot\vec{V}$ could not be balanced by the other terms in the vorticity equation. This means that the motions must be approximately horizontally nondivergent. The horizontal wind field may be expressed as the sum of a nondivergent part, $\vec{V}_\psi = \hat{k}\times\vec{\nabla}\psi$, and an irrotational part, $\vec{V}_\chi = \vec{\nabla}\chi$ where ψ and χ are a stream function and a vector potential, respectively. Then, since $\vec{V}$ is approximately nondivergent, it can be replaced by $\vec{V}_\psi$, except where it appears as $\vec{\nabla}\cdot\vec{V}$. In the divergence term, f may be replaced by the constant value, f_o.

Then, keeping only the largest terms, (1) becomes

$$\frac{\partial\zeta}{\partial t} + \vec{V}_\psi \cdot \vec{\nabla}(\zeta+f) + f_o \vec{\nabla}\cdot\vec{V} = 0 \qquad (2)$$

The nondivergent wind may be approximated by the geostrophic wind, $\vec{V}_g = \frac{1}{f_o} k \times \vec{\nabla}\phi$, and $\vec{\nabla}\cdot\vec{V}$ is given by $-\frac{\partial\omega}{\partial p}$. Then (2) becomes

$$\frac{\partial\zeta_g}{\partial t} + \vec{V}_g\cdot\vec{\nabla}(\zeta_g+f) - f_o\frac{\partial\omega}{\partial p} = 0 \qquad (3)$$

This is the quasi-geostrophic vorticity equation.

The equation governing the thermodynamics of a quasi-geostrophic system is obtained from the general thermodynamic equation (3.3) by assuming that the stability term, $\frac{\partial T}{\partial p} - \frac{\kappa T}{p}$ can be approximated by the stability, σ, which depends on p only. Then, replacing $\vec{V}$ by $\vec{V}_g$, and eliminating T by using the hydrostatic relation (3.4), the thermodynamic equation becomes

$$\frac{\partial}{\partial t}\left(-\frac{\partial\phi}{\partial p}\right) + \vec{V}_g\cdot\vec{\nabla}\left(-\frac{\partial\phi}{\partial p}\right) + \frac{R}{p}\sigma\omega = 0 \qquad (4)$$

Equations (3) and (4) describe a quasi-geostrophic system. In such a system, departures from geostrophy are allowed, and appear as a secondary circulation represented by a vertical velocity field, ω. This secondary circulation always acts to restore geostrophy, while maintaining hydrostatic balance.

VITA

Mary Alice Rennick was born on 16 September, 1948, in Oak Park, Illinois. She attended Knox College in Galesburg, Illinois, and received her B. A. with honors in physics in 1970. She received her M. S. in physics from the University of Illinois in 1972. She belongs to the American Meteorological Society.